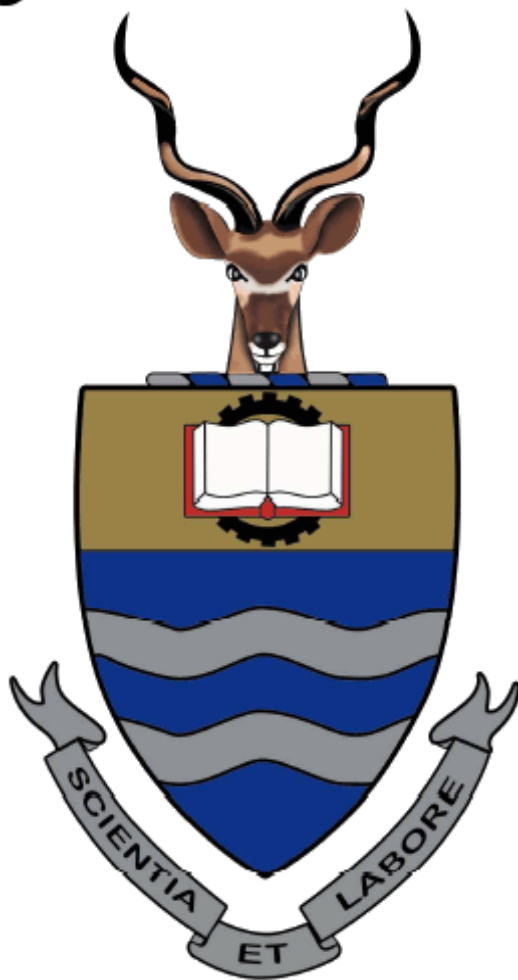


UNIVERSITY OF THE WITWATERSRAND



JOHANNESBURG

**THE SYNTHESIS, CHARACTERIZATION AND
PHOTOCATALYTIC ACTIVITY OF VARIOUS
MORPHOLOGIES AND SIZES OF ZnO PHOTOCATALYSTS**

BY

Siyabonga Siphonkabinde

(564058)

**A DISSERTATION SUBMITTED IN FULFILMENT OF THE
REQUIREMENTS FOR THE DEGREE OF**

MASTER OF SCIENCE IN THE SCHOOL OF CHEMISTRY

FACULTY OF SCIENCE

UNIVERSITY OF THE WITWATERSRAND

SUPERVISORS

Dr Zikhona N. Tetana

Prof. Nosipho Moloto

DECLARATION

I declare that the work reported in this dissertation is my own, unaided work. It is being submitted for the degree of Master of Science in the School of Chemistry, University of the Witwatersrand. It has not been submitted before for any degree or examination in any other University.

(Signature of candidate)

28th Day of March 2018

ABSTRACT

The increasing abundance of industries, together with the high human population density has prompted the pollution of the hydrosphere with organic and inorganic matter at a very high rate. To triumph over the problems caused by water pollution, and to comply with strict environmental regulations, researchers have been focusing on the development of new or improvement of existing water purification processes. One such process is known as Advanced Oxidation Processes (AOPs), and is based on using light quanta in conjunction with a photocatalyst (TiO_2 , ZnO , CdS , etc.) in order to degrade organic pollutants in an aqueous medium. An important factor in AOPs is the type of the photocatalyst being used as it controls the rate at which dyes are degraded when exposed to light quanta with energy higher or equals to its band gap energy. The photocatalytic activity of a photocatalyst is controlled by its properties such as surface area, crystallinity and morphology. These properties can be controlled by varying reaction parameters such as reaction time, type of precursor, and pH used when it is being synthesized. Furthermore, the photocatalytic activity also depends on operational parameters under which the photocatalyst is used. The operational parameters include factors such as the photocatalyst concentration, concentration of organic compounds in solution, pH at which the dye exists in nature, and light intensity. Zinc oxide nanoparticles were synthesized using microwave assisted heating method. Microwave assisted heating method was chosen over conventional colloidal method due to its ability to heat reaction mixtures homogeneously and very short reaction times. The synthesis of ZnO nanoparticles using a coprecipitation method between $\text{Zn}(\text{CH}_3\text{COO})\cdot 2\text{H}_2\text{O}$ and NH_3/NaOH via microwave assisted heating and their photocatalytic activity investigated. The crystalline structure, morphology and optical properties of as-synthesized ZnO were characterized by Powder X-ray diffraction (PXRD), Transmission Electron Microscopy (TEM) Scanning Electron Microscopy (SEM) and Ultra-violet Visible (UV-Vis) and Photoluminescence Spectrophotometer. ZnO was first synthesized using cetyltrimethylammonium bromide (CTAB) as capping agent and ammonia (NH_3) as precipitating agent in order to assess its photocatalytic activity in the degradation of Rhodamine B. Rhodamine B was used as a model dye as it is frequently used in industry. Rod like ZnO nanoparticles were produced with an average length of 608 nm and a width of 205 nm.

The operational parameters to be used during the course of the research were determined by performing photocatalyst concentration, dye concentration, light intensity, and pH studies. The extent of direct hydrolysis of the Rhodamine B dye under UV light without the photocatalyst was first measured to eliminate the possible contribution from the undesired variables to the overall efficiency. It was observed that using only light without a photocatalyst or vice versa could not degrade the dye, a combination of the two was needed for dye degradation. The ZnO photocatalyst was found to efficiently degrade the Rhodamine B dye at photocatalyst concentration of 160 ppm, light intensity of 210 W and at pH 8.

Morphological diversity was achieved by varying reaction parameters such as pH of the precursor solution and changing the type of zinc metal salts. Varying the pH changed the growth nature of ZnO forming pseudo-spherical nanoparticles at pH 7, bullet-like nanoparticles at pH 10 and rod-like nanoparticles at high pH of 14. The photocatalytic degradation experiments revealed that ZnO nanoparticles with different morphologies degraded Rhodamine B at different rates. The pseudo-spherical, bullet-, and rod-like nanoparticles degraded the dye at 150, 180, and 210 min, respectively. The difference in the rate of degradation was attributed to surface area differences and proportion of exposed polar facets (i.e. [0001], [000-1]) on the surface of the different morphologies.

Different sizes of the ZnO nanoparticles were prepared by varying the reaction time length, with short reaction time producing smaller particles than the longer reaction time. The photocatalytic activity of the nanoparticles was examined for the photocatalytic degradation of Rhodamine B as the test dye in aqueous solution under solar irradiation. The size of the nanoparticles was found to be highly dependent on the reaction time. Particle size influenced the photocatalytic activity with the smaller sized nanoparticles being more efficient in degrading Rhodamine B than the larger nanoparticles. The reason for the high catalytic activity was attributed to higher surface area. The as-synthesized ZnO photocatalyst showed good photocatalytic stability and can be reused four times with only gradual loss of activity. Thus, it is an efficient photocatalytic material for degrading contaminated coloured wastewater for reuse in textile industries under mild conditions.

The syntheses of ZnO nanoparticles using different precursors $\text{Zn}(\text{NO}_3)_2 \cdot 6\text{H}_2\text{O}$, $\text{Zn}(\text{CH}_3\text{COO})_2 \cdot 2\text{H}_2\text{O}$, ZnCl_2 , and $\text{ZnSO}_4 \cdot \text{H}_2\text{O}$, resulted in different structural, optical and photocatalytic activity. The difference in the properties of the nanoparticles synthesized in this study was attributed to the fact that the counter anions (i.e. NO_3^- , Cl^- , SO_4^{2-} , and CH_3COO^-) in the zinc metal salts are capable of coordinating to the crystal planes of ZnO differently. The different coordinating abilities of the counter anions resulted in dissimilar rates of growth and different morphologies. The BET surface area measurements were found to be 13.25, 12.34, 12.02, and 1.24 m^2g^{-1} for the NO_3^- , CH_3COO^- , Cl^- , and SO_4^{2-} counter anions, respectively. The difference in surface area indicated that the binding abilities of the counter anions to the decreased in the order $\text{NO}_3^- > \text{CH}_3\text{COO}^- > \text{SO}_4^{2-} > \text{Cl}^-$, with the NO_3^- anion binding more strongly to the crystal planes (i.e. [0001] and [000-1]) of ZnO and hence hindering rapid growth of the nanoparticles. Photocatalytic degradation studies indicated that the nanoparticles with the highest surface area were more active than those with lower surface area.

DEDICATIONS

To the women who gave birth to me, Duduzile Mgaga; my wonderful partner, Lebogang Sehoole, and my entire family, this is for you.

ACKNOWLEDGEMENTS

The completion of this dissertation is a combined effort from a variety of people, who all directly/indirectly made it to be a success.

- Lebogang Schoole, my pillar of strength, your belief in my abilities continue to motivate me on a daily basis.
- Dr Zikhona Tetana, I am thankful for the contribution to my knowledge in the field of photocatalysis. I appreciate you so much for your guidance and contribution throughout this project. Without you, this project would not have been a success.
- Prof Nosipho Moloto, your constructive criticism, intellectual capability and a good heart makes you the best advisor anyone can ever wish for. No words could ever express how much valuable you have been throughout my studies. May you continue to uplift black students in science.
- To my family, Duduzile, Zandile, Mzwakhe, Phindile Mgaga, your emotional and financial support throughout the course of my studies has kept me going even at times where I wanted to give up.
- To the CATOMMAT and the Quantum dots group, the group meetings have contributed so much to me as student. Sharing my work with you and getting constructive criticism back has made me a better researcher and presenter.

LIST OF PUBLICATIONS

Publication(s)

1. **S.S Nkabinde**, X. Mathebula, Z. Tetana and N. Moloto. The role of zinc metal salts on size, morphology and photocatalytic activity of ZnO, MRS Advances, First View, (2018) 1-13.

(Manuscripts to be submitted)

1. **S.S Nkabinde**, Z. Tetana, and N. Moloto. Morphology dependent photocatalytic activity of ZnO nanoparticles synthesized by microwave heating method.
2. **S.S Nkabinde**, Z. Tetana, and N. Moloto. The effect of reaction time on the size, morphology and photocatalytic activity of ZnO nanoparticles prepared via microwave heating method,

PRESENTATIONS

1. Oral presentation at the Catalysis Organometallics and Materials (CATOMAT) seminar held at the School of Chemistry, University of the Witwatersrand on the 15/06/2016
2. Oral presentation at the 64th South African Institute of Physics (SAIP) conference at the University of Cape Town, South Africa 04/07/2016
3. Oral presentation at the Catalysis Organometallics and Materials (CATOMAT) seminar held at the School of Chemistry, University of the Witwatersrand on the 15/06/2017.
4. Oral presentation at the Annual Gauteng's Nanoscience Young Researcher's Symposium (NYRS) held on the 18/11/2016, MINTEK in Randburg
5. Oral presentation at the Catalysis Organometallics and Materials (CATOMAT) seminar held at the School of Chemistry, University of the Witwatersrand on the 15/06/2017
6. Oral presentation at the Catalysis Organometallics and Materials (CATOMAT) seminar held at the School of Chemistry, University of the Witwatersrand on the 15/06/2017
7. Poster presentation at the South African Chemical Institute (SACI) conference held in the Western Cape on the 25/07/2017
8. Oral presentation at the Catalysis Organometallics and Materials (CATOMAT) seminar held at the School of Chemistry, University of the Witwatersrand on the 25/08/2017

TABLE OF CONTENTS

THE SYNTHESIS, CHARACTERIZATION AND PHOTOCATALYTIC ACTIVITY OF VARIOUS MORPHOLOGIES AND SIZES OF ZnO PHOTOCATALYST.....	i
BY	i
DECLARATION	ii
ABSTRACT	iii
DEDICATIONS.....	vi
ACKNOWLEDGEMENTS.....	vii
LIST OF PUBLICATIONS.....	viii
PRESENTATIONS	ix
LIST OF ABBREVIATIONS	xix
CHAPTER 1: Synopsis	1
1.1 Brief elucidation of the dissertation	1
1.2 Problem statement	2
1.3 Project motivation.....	3
1.4 Project aims and motivations.....	3
1.5 References	4
CHAPTER 2: Literature Review.....	5
2.1 General Introduction.....	5
2.2 Dyes and Pigments	7
2.4 Principles of ZnO in photocatalytic degradation.....	11

2.5 Quantitative analysis of dyes.....	15
2.5.1 UV-Vis absorption spectroscopy	15
2.5.2 Mass spectrometry	17
2.5.3 High Pressure Liquid Chromatography	20
2.6 The effect of operational parameters on the photocatalytic degradation efficiency.....	21
2.6.1 Catalyst loading	21
2.6.2 Dye concentration	22
2.6.3 Solution pH	22
2.6.4 Light intensity	23
2.7 Basic properties of ZnO.....	25
2.8 Synthesis of ZnO nanocrystals.....	27
2.8.1 Sol-gel Method.....	27
2.8.2 Hydrothermal Method.....	28
2.8.3 Microwave heating method.....	29
2.9 Synthesis parameter affecting the properties of ZnO nanocrystals.....	31
2.9.1 Reaction time	31
2.9.2 Type of precursor	33
2.9.3 pH of the solution.....	34
2.10.....Physical properties influencing the activity of a ZnO photocatalyst	35
2.10.1 Surface area.....	35
2.10.2 Non-metal anionic impurities	36
2.11..Atom-mediated nucleation and growth mechanism of metallic nanoparticles in solution.....	38
2.11.1 Nucleationand growth.....	39
2.11.2 Classical atom-mediated nucleation and growth	39
2.11.4 Non-classical nucleation and growth.....	42
2.12 References.....	46

CHAPTER 3: The Effects of operational parameters on the photocatalytic degradation of Rhodamine B60

3.1 Introduction60

3.2 Synthesis Procedure.....62

 3.2.1 Chemicals and materials 62

 3.2.2 Synthesis of ZnO nanoparticles 62

 3.2.3 Characterization 62

 3.2.4 Photocatalytic degradation of Rhodamine B 63

 3.2.5 Determination of the point of zero charge of ZnO nanoparticles 65

3.3 Results and Discussion66

 3.3.1 Structural properties of ZnO 66

 3.3.2 Optical properties of ZnO 69

3.4 Photocatalytic degradation study.....71

 3.4.1 Preliminary studies..... 71

 3.4.2 Effect of ZnO nanoparticles loading..... 74

 3.4.3 Effect of dye concentration..... 79

 3.4.4 Effect of pH..... 82

 3.4.5 Effect of light intensity 85

 3.4.6 Reusability of ZnO..... 86

3.5 Conclusions90

3.6 References91

Chapter 4: Microwave synthesis of various morphologies of ZnO and their photocatalytic activity.97

4.1 Introduction97

4.2 Synthesis Procedure.....100

 4.2.1 Chemicals and materials 100

 4.2.2 Synthesis of ZnO nanoparticles at different pH values 100

 4.2.3 Characterization 100

4.2.4	Photocatalytic degradation of Rhodamine B	101
4.3	Results and Discussion	103
4.3.1	Structural properties.....	103
4.3.2	Optical properties.....	108
4.4	Photocatalytic degradation of Rhodamine B.....	110
4.5	Conclusion	115
4.6	References	116
Chapter 5: Effect of reaction time on the size, morphology and photocatalytic activity of ZnO nanoparticles.		120
5.1	Introduction	120
5.2	Synthesis procedure.....	122
5.2.1	Chemicals and materials	122
5.2.2	Synthesis of ZnO nanoparticles	122
5.2.3	Photocatalytic degradation of Rhodamine B	123
5.2.4	Characterization	124
5.3	Results and Discussion	125
5.3.1	Structural properties.....	125
5.3.2	Optical properties.....	129
5.4	Photocatalytic degradation studies	132
5.5	Conclusion	135
5.6	References	136
CHAPTER 6: The role of zinc metal salts on size, morphology and photocatalytic activity of ZnO.....		139
6.1	Introduction	139
6.2	Synthesis procedure.....	141
6.2.1	Chemicals and materials	141
6.2.2	Synthesis of ZnO nanoparticles using different precursors	141
6.2.3	Characterization	142

6.2.4	Photocatalytic degradation of Rhodamine B	143
6.3	Results and Discussion	144
6.3.1	Structural properties.....	144
6.4	Photocatalytic degradation of Rhodamine B.....	156
6.5	Conclusion	160
6.6	References	161
Chapter 7: Conclusions and Recommendations		164
7.1	Conclusions	164
7.2	Recommendations	165

LIST OF FIGURES

Figure 2.1: Various types of dyes.	8
Figure 2.2: Crystal structure of Malachite green and Acid Yellow 36.	7
Figure 2.3: The crystal structure of Rhodamine B.	9
Figure 2.4: A schematic representation of the mechanism of photocatalysis [33].	13
Figure 2.5: Typical UV-Vis absorption spectra of Rhodamine B.	16
Figure 2.6: Time dependent changes of UV-Vis absorption spectrum of Rhodamine B during the degradation of the dye.	17
Figure 2.7: Photocatalytic degradation mechanism of Rhodamine B [48].	19
Figure 2.8: The wurtzite structure of zinc oxide [80].	26
Figure 2.9: Typical flow diagram for sol-gel synthesis method.	27
Figure 2.10: Schematic diagram of the hydrothermal synthesis method.	28
Figure 2.11 A diagram showing the different interaction of the heat source with the reaction medium during (a) conventional and (b) microwave heating.	30
Figure 2.12: Growth of nanoparticles in an aqueous solution with time.	32
Figure 2.13: Illustration of the different types of crystal facets exposed in ZnO nanoparticles with respect to its morphological form.	37
Figure 2.14: LaMer curve describing the metal nanocrystals formation stages in a reaction medium [137].	40
Figure 2.15: OA mechanism observed during growth of Pt nanocrystals [152].	43
Figure 3.1: Plot for determination of the point of zero charge of as-synthesized ZnO.	65
Figure 3.2: PXRD pattern of the ZnO nanoparticles prepared by microwave heating method.	66
Figure 3.3: TEM micrograph of the ZnO synthesized via microwave assisted heating method. .	67
Figure 3.4: The (a) UV-Vis absorption and (b) PL spectra of ZnO nanoparticles synthesized using microwave heating method.	69
Figure 3.5: UV-Vis spectra changes of (a) Rhodamine B as a function of light irradiation and (b) physical colour change monitored for 210 min.	71

Figure 3.6: The percentage of Rhodamine B dye degraded in 30 min intervals.	72
Figure 3.7: UV-Vis absorption spectra changes of Rhodamine B under UV irradiation in the absence of ZnO nanoparticles.	74
Figure 3.8: Percentage degradation of Rhodamine B as a function of ZnO concentration done over a period of 5 h.	75
Figure 3.9: Kinetic study of the degradation of Rhodamine B (20 ppm) at different ZnO photocatalyst loading (80 - 200 ppm).	77
Figure 3.10: Effect of initial concentration of Rhodamine B on degradation efficiency	79
Figure 3.11: Plot of $\ln(C_0/C_t)$ against irradiation time obtained during the photocatalytic degradation of Rhodamine B.	80
Figure 3.12: A graph showing the effect of pH on the photocatalytic degradation efficiency of ZnO nanoparticles.	82
Figure 3.13: A study showing the % degradation of Rhodamine B at different light intensities.	85
Figure 3.14: Reusability study of the ZnO nanoparticles for up to 4 cycles.	87
Figure 3.15: The morphological changes of ZnO nanoparticles after (a) 1 st , (b) 2 nd , (c) 3 rd , and (d) 4 th cycles of reusing the nanoparticles.	88
Figure 3.16: The (a) UV-Vis absorption and (b) PL spectra of the ZnO nanoparticles used for up to 4 cycles.	89
Figure 4.1: PXRD patterns of the ZnO nanoparticles synthesized at (a) pH 7, (b) pH 10, and (c) pH 14.	103
Figure 4.2: TEM micrographs of the different morphologies of ZnO nanoparticles synthesized at (a) pH 7, (b) pH 10, and (c) pH 14.	104
Figure 4.3: Possible growth mechanism of the aggregated rod like nanostructures.	105
Figure 4.4: SEM images of the different morphologies of ZnO nanoparticles synthesized at (a) pH 7, (b) pH 10, and (c) pH 14.	107
Figure 4.5: Room temperature absorption spectra of ZnO nanoparticles synthesized at different pH values.	108
Figure 4.6: Room temperature emission spectra and of the ZnO nanoparticles synthesized at different pH values.	109

Figure 4.7: Typical UV-Vis spectra changes of Rhodamine B (20 ppm, neutral water pH) upon irradiation in the presence of ZnO (160 ppm) nanoparticles synthesized at pH 14.....	111
Figure 4.8: The % degradation versus irradiation time plot for the pseudo-spherical, bullet- and rod-like nanoparticles.....	112
Figure 4.9: The dominant facets present on the surface of ZnO with different morphologies (modified from [53]).	113
Figure 5.1: PXRD diffractograms of ZnO nanoparticles prepared at different reaction times using microwave assisted heating.....	125
Figure 5.2: TEM micrographs of the ZnO nanoparticles synthesized for (a) 8, (b) 11, (c) 15, (d) 18, and (e) 30 min via microwave assisted heating.	127
Figure 5.3: The UV-Vis absorption spectra of the as synthesized ZnO nanoparticles.	129
Figure 5.4: PL spectra of ZnO synthesized over 8, 11, 15, 18 and 30 min reaction time via microwave assisted synthesis.....	131
Figure 5.5: (a) UV-Vis absorption spectra changes of Rhodamine B and (b)% degradation for the photocatalysts synthesized at different reaction times.....	133
Figure 6.1: PXRD of ZnO nanoparticles synthesized using different zinc metal salt precursors.....	145
Figure 6.2: TEM micrographs of ZnO synthesized using (a) $S_{NO_3^-}$, (b) $S_{CH_3COO^-}$, (c) S_{Cl^-} , and (d) $S_{SO_4^{2-}}$ zinc metal salts. (Red arrows – Oriented attachment).....	148
Figure 6.3: Proposed mechanism through which ZnO nanoparticles undergo oriented attachment.....	149
Figure 6.4: ZnO crystal showing the axial and equatorial face specific growth which formed (a) rod- and (b) hexagonal nanoparticles, respectively.....	151
Figure 6.5: Absorption spectra of ZnO nanoparticles synthesized under the same experimental conditions varying only the zinc metal salts.....	155
Figure 6.6: Room temperature emission spectra of ZnO synthesized using different zinc metal salts.....	156
Figure 6.7: UV-vis spectral changes of Rhodamine B during the course of degradation using (a) $S_{NO_3^-}$, (b) $S_{CH_3COO^-}$, (c) S_{Cl^-} , and (d) $S_{SO_4^{2-}}$ nanoparticles.....	158

LIST OF TABLES

Table 3. 1: Operational parameters varied together with the parameters that were kept constant during degradation of Rhodamine B.....	64
Table 3.2: Rate constant for photocatalytic degradation of Rhodamine B.....	78
Table 4.1: Rate constants for photocatalytic degradation of Rhodamine B using different ZnO morphologies.....	115
Table 5.1: Corresponding PXRD data of the different ZnO.....	126
Table 5.2: Rate constants for photocatalytic degradation of Rhodamine B using ZnO nanoparticles synthesized at different reaction times.....	137
Table 6. 1: Full-width half maximum and relative crystallite sizes of the ZnO nanoparticles...	145
Table 6.2: BET results of the synthesized ZnO nanoparticles.....	151
Table 6.3: Rate constants for photocatalytic degradation of Rhodamine B using ZnO nanoparticles synthesized from different zinc metal salts.....	163

LIST OF ABBREVIATIONS

AOPs - Advanced Oxidation Processes

AR14 - Acid red 14

CTAB - Cetyltrimethylammonium Bromide

CdS - Cadmium Sulphide

CB - Conduction Band

CO₂ - Carbon dioxide

C_{main}^{nu} - Minimum supersaturation level

C_s - Solubility concentration

DR - Digestive Ripening

e⁻ - electron

Eq - Equation

E_g - Band gap energy

E₀ - Oxidation potential

eV - Electron volts

FWHM - Full Width Half Maximum

HPLC - High Pressure Liquid Chromatography

HOO⁻ - Hydroperoxyl radicals

H₂O₂ - Hydrogen Peroxide

h⁺ - Hole

H⁺ - Hydrogen cation

hν - Energy of light

h - Hours

IR - Intraparticle Ripening

LC-MS - Liquid Chromatography-Mass spectrometry

MO - Methyl Orange

m/z - Mass to charge ratio

N - Number of nanoparticles

OH^\bullet - Hydroxyl radicals

$\text{O}_2^{\bullet -}$ - Superoxide radical anions

OA - Oriented Attachment

OR- Ostwald Ripening

OH^- - Hydroxyl anions

PPM - Parts Per Million

PL - Photoluminescence

P_{zc} - Point of zero charge

R6G - Rhodamine 6G

RB - Rhodamine B

R6G - Rhodamine 6G

SnO - Tin Oxide

TEM - Transmission Electron Microscopy

UV-Vis - Ultraviolet Visible Spectroscopy

UV -Ultra Violet

VB - Valence Band

V_{dye} - Volume of Rhodamine B dye

ZnO - Zinc Oxide

CHAPTER 1: Synopsis

1.1 Brief elucidation of the dissertation

Outlined in chapter 1 is a brief description of what each chapter in the dissertation entails. It is also composed of the problem statement, motivation, aims and objectives of the study. Chapter 2 draws attention to the general background on the nature of water pollution from the textile industry and the various ways that are used to remediate polluted natural water systems. Focus on Advanced Oxidation Processes (AOPs) as a promising method for water remediation is elucidated. The synthesis of ZnO nanoparticles as a potential photocatalyst in AOPs is demonstrated. The effects of various reaction parameters on the optical and structural properties of ZnO are also explained.

The focal point of the third chapter is the synthesis, characterization and photocatalytic activity of ZnO nanoparticles prepared using a simple microwave heating method. In this chapter, the ZnO nanoparticles are used to determine the operational parameters (e.g. pH, photocatalyst loading, light intensity) to be used in the photocatalytic degradation of Rhodamine B throughout the course of the study.

The fourth chapter outlines the synthesis and characterization of various morphologies of ZnO by varying the pH of the precursor solution. The optical and structural properties resulting as a result of varying pH are looked into. Furthermore, the effects that the different morphologies have on the rate of degradation of Rhodamine B are discussed.

The fifth chapter looks at how the most efficient ZnO morphology (i.e. pseudo-spherical nanoparticles) in degrading Rhodamine B as reported in chapter four, can be modified in order to produce a more efficient ZnO photocatalyst. This was done by varying the reaction time used in microwave assisted heating. The effect of reaction time on the size, morphology and photocatalytic activity of ZnO nanoparticles is discussed.

The sixth chapter focuses the synthesis of ZnO nanoparticles using various zinc metal salts using the method used in chapter five. The effects that varying the zinc metal salts has on the size,

morphology and photocatalytic activity of ZnO in the degradation of Rhodamine B are discussed.

The seventh chapter outlines the general conclusions on this dissertation and provides recommendations for future work.

1.2 Problem statement

The water levels in natural systems are currently at a record low due to the low frequency of heavy rainfall in the country. Furthermore, the majority of water that is available is heavily polluted to such an extent that it cannot be used for farming or drinking [1]. The release of coloured dyes by the textile industry is one of the main contributors to water pollution [1-2]. This nature of pollution is characterized by coloured water which harms aquatic life and humans that utilize it as a basic need [3]. The chemical break down of dyes in solution is the cause of the fatal effects associated with coloured waste water [4]. For example, nitro and azo dyes are known to be reduced in aquatic sediment bodies producing amines that are carcinogenic. Malachite green dye has also been reported to be carcinogenic and genotoxic agents that affect both the reproductive and immune system [4]. A wide variety of dyes have been identified as having fatal effect, as such, strict environmental protection laws have been set in place which forces industries to come up with remediation methods to deal with water pollution [4-5]. One method that has been developed is Advanced Oxidation Processes (AOPs) and is based on using sunlight in conjunction with a photocatalyst such as ZnO in order to degrade dyes in aqueous solution [6-8]. This method has shown positive results when used to remove coloured dyes in natural water and improving it through the synthesis of highly active photocatalysts is important.

1.3 Project motivation

Metal oxides such as ZnO and TiO₂ possess admirable electronic, optical and catalytic properties compared to their sulfide counter parts. Their photocatalytic activity can be varied by manipulating their size and shape. The ability to produce these types of materials using a simple and fast microwave assisted method provides an opportunity to upscale the synthesis for application in real life applications.

1.4 Project aims and motivations

The aim of the project was to synthesize and characterize ZnO nanoparticles and use them in the photocatalytic degradation of Rhodamine B dye. The above mentioned aims were fulfilled by identifying the following objectives.

- Synthesis and characterization of different sizes and morphologies of ZnO nanoparticles by varying reaction parameters using microwave assisted heating.
- Use the ZnO nanoparticles as photocatalysts in the photocatalytic degradation of the Rhodamine B dye.

1.5 References

- [1] N. Tripathy, R. Ahmad, J.E. Song, H.A. Ko, Y. Hahn, and G. Khang, *Materials Letters*, **136**, (2014) 171-174
- [2] M.H. Habibi, and M.H. Rahmati, *Spectrochimica Acta Part A: Molecular and Biomolecular Spectroscopy*, **137**, (2015) 160–164
- [3] D. Kim, and Y. Huh, *Materials Letters*, **65**, (2011) 2100-2103
- [4] D. Ratna, and B.S. Padhi, *International Journal of Environmental Sciences*, **3**, (2012) 940-955
- [5] H. Zolinger, *Colour chemistry- Synthesis, Properties of dyes and pigments*, VCH publishers, New York, (1987) pp 92
- [6] X. Li, J. Wang, J. Yang, J. Lang, S. Lü, M. Wei, X. Meng, C. Kou, and X. Li, *Journal of Alloys and Compounds*, **580**, (2013) 205-210
- [7] L. Fang, B. Zhang, W. Li, X. Li, T. Xin, and Q. Zhang, *Superlattices and Microstructures*, **75**, (2014) 324-333
- [6] M. Bitenc, B. Horvat, B. Likozar, G. Drazic, and Z.C. Orel, *Applied Catalysis B: Environmental*, **136–137**, (2013) 202-209
- [8] I.Y.Y. Bu, *Ceramics International*, **39**, (2013) 1189–1194

CHAPTER 2: Literature Review

2.1 General Introduction

The textile industry's primary concern is the manufacturing and design of cloth, yarn, clothing and their distribution [1]. Over the past decades, it has been established that there is an increased demand in the production of coloured clothing by the textile industry, mainly due to the forever increasing human population. As a result of this, large amount of coloured wastewater (dyes) are generated when each piece of clothing is given its desired colour [2]. The problem arises when the coloured wastewater is not managed properly and ends up in rivers, lakes or any other water sources around the area of discharge. The inability of mother nature to biodegrade such dyes means that they are able to persist in moving water, surviving long distances from the area in which they were originally introduced into the environment [3, 4]. Living organisms that are essential for a balanced ecosystem in rivers are affected by the coloured water through the destabilization of photosynthesis in water. In the presence of dyes in aqueous solution, the ability of sunlight to pass through the water is retarded, and this therefore forecloses the growth of aquatic life [5-7]. Such water can also be detrimental to human beings who are dependent on using the rivers where the dyes are discharged as they are known to be mutagenic and carcinogenic to humans [8-10]. This has therefore turned environmental pollution prevention into one of the main areas of research because of the fatal effects that coloured wastewater imparts on both wild and human life. The limited progress in dealing with this kind of water pollution has been due to the inability of the current methods to destroy the dyes entirely, without converting them into other forms that could potentially be more toxic [11, 12]. Some of the methods that have been previously used to remove dyes from water include air stripping, adsorption, Ozonation and precipitation [13]. Air stripping is used mainly in dealing with organic compounds that are volatile (Volatile Organic Compounds). The liquid organic compound of interest is allowed to come into contact with a gaseous phase such that it is transferred into gaseous phase and evaporates into the environment [14]. The removal of volatile organic compounds in this way results in deadly volatiles being released into the atmosphere [14].

Adsorption is based on using an adsorbent (e.g. activated carbon) which attracts the dye molecules to its surface thus removing the colour from an aqueous medium [15]. Adsorption is therefore advantageous in removal the colour but it does not destroy the dyes and hence further treatment is required [16]. The Ozonation method for water treatment uses an unstable gas known as ozone. Ozone is made up of three oxygen atoms that are highly unstable and capable of spontaneously decomposing. Upon decomposition, it dissociates into oxygen and a free radical oxygen form. The oxygen radical is very short lived and is highly reactive. It is these highly reactive radicals that are vital in the oxidation of dyes in aqueous medium [17]. Some of the advantage of using ozone is the fact that it has strong oxidizing power that results in short reaction time when it is being used. Treatment processes using ozone does not add chemicals to water, making it a moderately environmental friendly method to use. As most industrial methods, using ozone comes with the disadvantages of requiring high equipment and operation costs. There is also high toxicity issues associated with ozone generation. The biggest fall back of using ozone is that it is less soluble in water and hence requires special mixing techniques in order to be used efficiently [17, 18]. To summarize, the previously used methods in water purification have limitations in efficiently dealing with the coloured waste water from industry. This has therefore led to the realization of semiconductor photocatalysis as a promising means to reduce the extent of water pollution caused by dyes from the textile industry [19-21]. Photocatalysis has allowed for the dyes to be degraded completely without producing harmful by products which need to be treated further [21].

2.2 Dyes and Pigments

Colorants are defined as organic/inorganic compounds that when deposited onto the outermost surface of a particular material imparts colour through a process that changes, at least to a certain extent, the structure of the material/substrate requiring the colour [22]. The two types of colorants produced today are dyes and pigments. Pigments exist in both organic and inorganic form while dyes exist only as water-soluble or water insoluble organic compounds [22]. The major difference between the two is that colorants require a binder in order for them to form a coating on the surface of the substrate. The interaction between the pigments and substrate does not alter the crystal structure of the substrate [22]. Dyes on the other hand result to the destruction of the crystal structure of the substrate upon interaction. The molecules of the dye become irreversibly binded to the material in which they are used [22].

Dyes (Figure 2.1) have a very strong affinity to synthetic and natural materials due to their high colouring affinity and this makes them very important in the paper, food, photographic and most importantly in the textile industry [23]. The ability of a dye to impart colour is dependent on the affinity between the substrate and the dye and hence the development of a dye is often done with a specific substrate in mind. The main focus of the textile industry is primarily the production and colouring of raw fabrics. Depending on the type of interaction between the fabric and the dye, it can either be reversible or an irreversible kind of interaction. Hydrogen, covalent and ionic bonding is responsible for irreversible interaction while van der Waals forces dominate in reversible interactions [24]. The commonly used criterion to classify dyes is based mainly on the chemical structure, with characteristics such as trade name, intended use and colour being the rarely used criteria in the classification scheme [25].

The classification of dyes using chemical structure is done by looking at the functional groups which are responsible for the colour. These particular functional groups are known as chromophores and auxochromes [25]. The absorption of a certain wavelength of light by the chromophores results in the colour. The auxochromes on the other hand augment the chromophore's colour and enhance the dye molecule's ability to dissolve in water [25, 26]. The structural variety that exists between dyes allows them to also be classified according to composition. This is done by grouping them based on how soluble they are in various solvents.

Dyes can be basic, acidic, mordant, reactive, direct, and be metal based dyes [26, 27]. Currently, there are more than a hundred thousand dyes available commercially in the market [27].

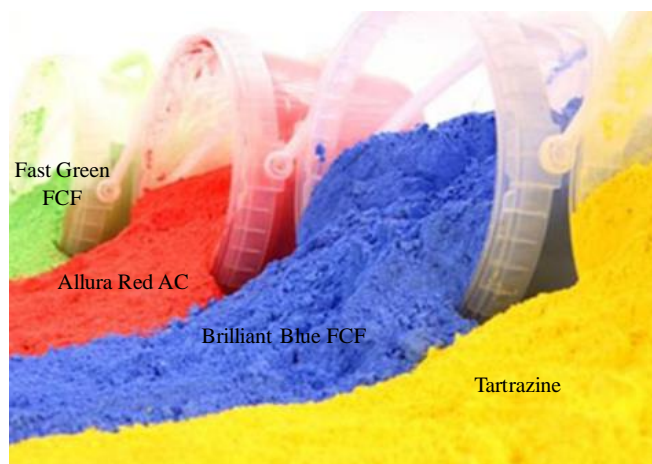


Figure 2.1: Various types of dyes [28].

Basic dyes (Figure 2.2(a)) such as malachite green are soluble in water and their coloured cations are responsible for the production of colour in an aqueous solution [29]. They mostly exist as amino and substituted amino compounds that are soluble in an acidic medium. They are made insoluble in the case where they are used under more basic conditions [29]. Their existence as cations allows them to attach to the substrate through ionic bonding with anionic groups [29]. Acidic dyes (Figure 2.2(b)) are soluble in water and their colour comes from their anions.

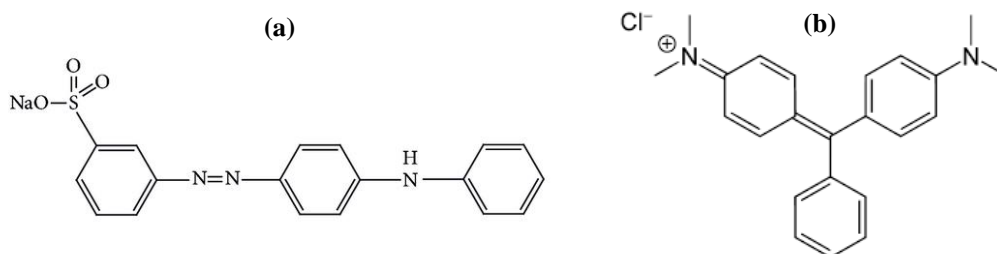


Figure 2.2: Crystal structure of Malachite green and Acid Yellow 36.

They contain one or more sulfonic acid substituents or other acidic group in their structure. The use of dyes has increased tremendously over the years and this has resulted to environmental issues [29]. When the dyes are being applied to fabrics, they are commonly dissolved in water. The water they are dissolved in has to be discarded when the fabric have been coloured. An issue arise when the dyes are not disposed of properly and are allowed to enter natural water sources

such as rivers and lakes [30]. The chemical composition of dyes is made up of a variety of organic substituents that can be toxic. In addition to being toxic, aqueous dye solutions contain chemicals that can be teratogenic, carcinogenic and mutagenic to various living organisms [30]. Dyes such as malachite green contain amines which can be reduced in sediments resulting to carcinogenic amines [30]. There is evidence that malachite green doesn't only affect the reproductive and immune system but it is also a genotoxic agent [31].

A wide range of dyes (Rhodamine B, Methyl Violet, Basic Green 4 etc.) are used for the sole purpose of giving each clothing material its desired colour but pose an issue due to their toxic nature in the environment [32]. Rhodamine B was chosen as a model dye not only because of its frequent use in industry but also because of its complex chemical structure (Figure 2.3) which makes it much harder to biodegrade in the environment [32].

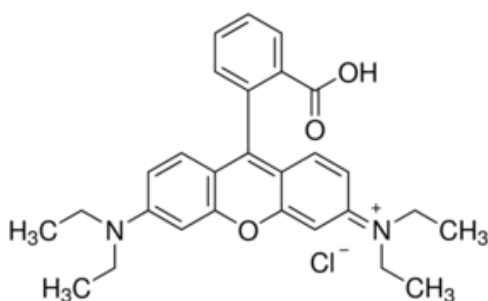


Figure 2.3: The crystal structure of Rhodamine B.

Rhodamine B is a cationic dye (basic dye) characterized by a positive ion on its molecule. It falls under a group of organic compounds known as xanthenes which are characterized by a poly aromatic structure and high molecular weight [33]. Human exposure to this dye causes irritation of the eyes and when it is inhaled or ingested it can cause damage to the thyroid and the liver. Rhodamine B is also known to be mutagenic, carcinogenic and neurotoxic [34]. In light of this, considering the negative health effect associated with this dye, it is worthwhile to perform an extensive study to remove the red to violet colour associated with the presence of Rhodamine B in natural water.

2.3 Photocatalysis

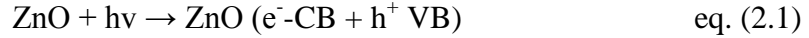
The oil and energy crisis in 1972 and 1979, respectively, resulted to the discovery of photocatalysis as the production of hydrogen by splitting water attracted attention. Fujishima and Honda [35] conducted a study on a TiO_2 electrode semiconductor which was able to produce hydrogen when irradiated with light. Due to this discovery, the application of photocatalysis received a lot of attention for applications such as photoinduced self-cleaning [36], photocatalytic removal of heavy metals [37], photooxidation/photodegradation [38] and photocatalytic gas phase oxidation [39]. Earlier studies on photocatalytic reactions were focused mostly on semiconductors such as ZnO (3.3 eV) and TiO_2 (3.2 eV) that have very wide band gap energies [40, 41]. Kinetic and thermodynamic limitations were believed to be the prominent drawbacks in photocatalysis. Properties of a semiconductor such as light absorption, migration and recombination, charge production determines the effectiveness of a semiconductor in photocatalysis. The first step, which is light absorption, determines whether a semiconductor is efficient to use for harvesting solar energy. The issue of light absorption is particularly severe with ZnO and TiO_2 because they are capable of only using 4% of the UV-light from the sun [42, 43]. With over 4 years of research and development, the degradation of gaseous pollutants or organic dyes or CO_2 conversion and water splitting for solar fuels have been the main areas of research. When the key word “photocata” is searched on the ISI database, approximately 5840 results come up. This is an indication that the gaps in industry associated with new material discovery and theoretical studies are receiving a great deal of attention. There exist a gap between practical application and research is still not resolved. The introduction of photocatalysis commercially has to be both economically and technically competitive to the currently available technologies for example chemical synthesis [44], hydrogen production from hydrocarbon reforming [45], CO_2 conversion by dry reforming and advanced oxidation processes [46]. The severe effects of water pollution have been recognised in the whole world for a long time. Heterogeneous semiconductor photocatalysis for partial oxidation of organic dyes has been systematically studied but literature lacks in reporting more effective ways of synthesizing photocatalysts. In this study we aim to bridge this gap by paving for efficient ways of synthesizing semiconductors.

2.4 Principles of ZnO in photocatalytic degradation

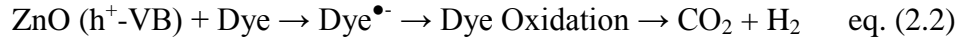
In response to the current global issues, heterogeneous semiconductor photocatalysis has been extensively studied for application in a wide range of environmental applications. The water purification industry is one area in which photocatalysis has become immensely important mainly because of the environmental pollution prevention laws put in place in many countries. The use of semiconductors in photocatalysis falls under a method known as Advanced Oxidation Processes (AOPs) [47]. In the past decades, coloured waste water has been treated with AOPs such as Ozonation and Fenton reagents. In a broad sense, AOPs are defined as a series of chemical procedures that are put in place in order to remove organic compounds in wastewater by using hydroxyl radicals that are very reactive [48]. AOPs employ a process that is known as photocatalysis. Photocatalysis is based on using light in conjunction with a photocatalyst (i.e., etc.) or an oxidant (i.e. H_2O_2) in order to increase the rate of chemical reactions by initiating chemical transformations with the surrounding matter [48]. A variety of different photocatalysts such as ZrO_2 , ZnO , SnO_2 , CdS , SrO_2 , ZnS , and TiO_2 have been employed in the photocatalytic degradation of dyes [49]. To date, ZnO and TiO_2 are reported to be the most efficient photocatalysts in dealing with coloured waste water. The cheapness, stability in aqueous medium, lack of toxicity and insolubility of TiO_2 has earned it its reputation for application in industrial applications [50]. The draw back with TiO_2 is that in the entire solar UV light, it can only utilise 3%. The challenge of using the entire solar energy from the sun by certain photocatalyst has forced researchers to focus on developing photocatalysts that can use all the UV light from the sun [50]. For example, CdS with band gap energy of 2.41 eV shows low photocatalytic activity when used alone due to rapid electron hole recombination [51]. Studies have revealed that using a CdS/ZnO composite is capable of efficiently degrading organic dyes [51]. ZnO has also been applied in photocatalysis but to a lesser extent than TiO_2 . The ability of ZnO to absorb a wide range of light from the solar spectrum has made it a more promising material for future applications.

Photocatalysts may therefore defined as a group of compounds which upon exposure to light quanta are capable of causing chemical changes in reaction substrates that they come into contact with [52-54]. Various researchers have proposed a plausible mechanism through which semiconductor photocatalysts are activated in the presence of sunlight. The proposed mechanism

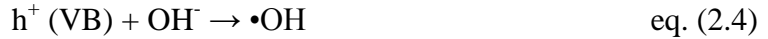
infers that upon illumination with light which has energy which is greater or equals to its band gap (i.e. $h\nu > E_g$), the photocatalyst undergoes photoexcitation which causes the ground state electrons which are located in the valence band (e^- -VB) to be excited and thus promoted to the conduction band (e^- -CB) as illustrated in Figure 2.4 [55, 56]. Through this process and in the case where electron-hole recombination does not occur, a hole is left behind at the catalyst surface (eq. (2.1)).



The property of this hole which makes it desirable is its high oxidation potential that allows it to be able to directly oxidize dyes converting them into much simpler counter parts through photo oxidation reactions (eq. (2.2)).



In the presence of photo activated ZnO photocatalyst, water can decompose into reactive hydroxyl radicals (eq. (2.3)). These hydroxyl radicals are not only formed this way, they are also produced when hydroxyl anions come into contact with the highly oxidative holes in zinc oxide (eq. (2.4)) [57, 58].



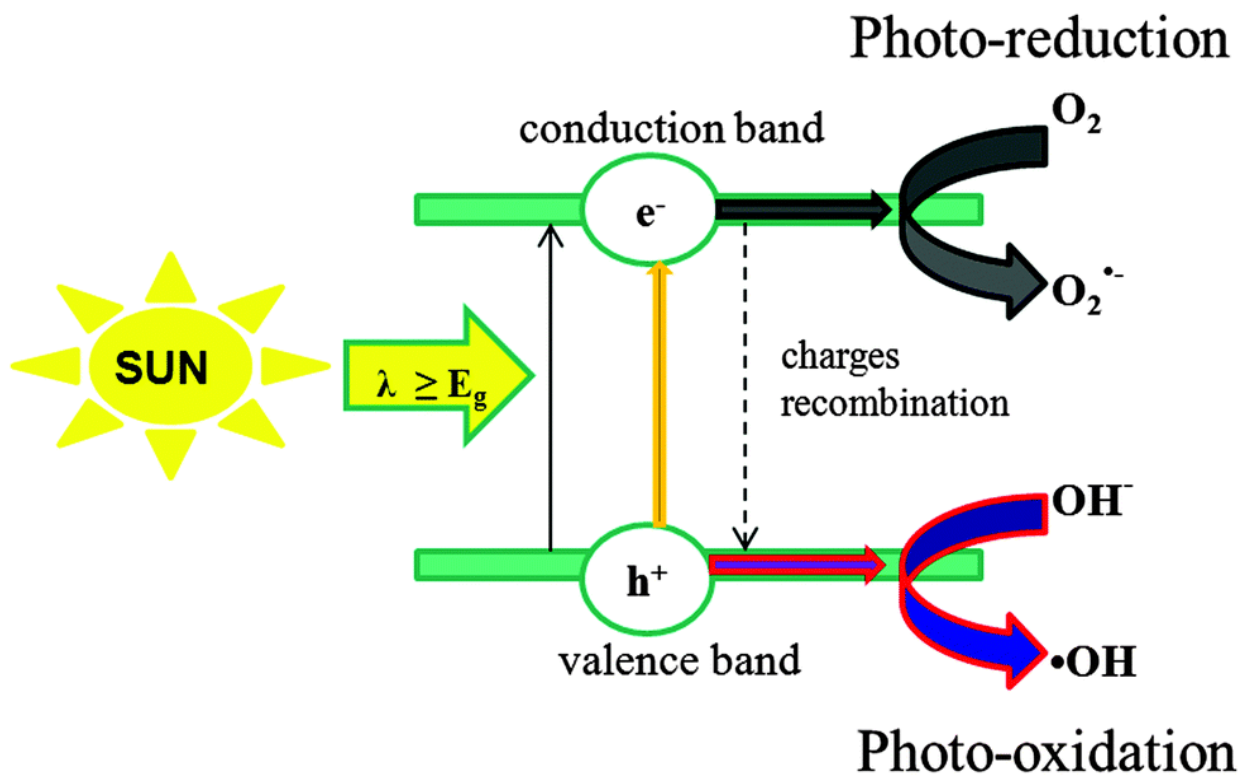


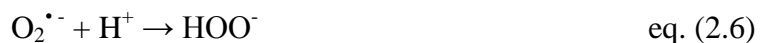
Figure 2.4: A schematic representation of the mechanism of photocatalysis [33].

The easily produced hydroxyl radicals generated are known to be non-selective oxidants which are very strong ($E_0 = +3.06$ V) and oxidize organic matter and break it into less toxic products (carbon dioxide, water and inorganic salts) effortlessly.

Photo oxidation reactions (eq. 2.5, 2.6, 2.7 and 2.8)) are also part of the well sort after degradation process. The photogenerated electrons may come into contact with oxygen at the surface of ZnO and react with it to form what is known as superoxide radical anions (eq. (2.5)).



The superoxide radical anions are very unstable and very reactive; hence they can be protonated to form hydroperoxyl radicals (HOO^\bullet) and subsequently hydrogen peroxide (H_2O_2) (eq. 2.6 and 2.7). The just generated hydrogen peroxide can further react with an electron to form hydroxyl anion and hydroxyl radicals (eq. (2.8)) [59-61].





The large quantities of hydroxyl radicals and hydroxyl anions are the major species which are necessary for the high efficiency of the photocatalytic degradation process. It can be noted that the availability of surface oxygen act to some extent as an electron capture, which prevents the high electron-hole recombination rates that reduces the efficiency of ZnO photocatalysts [62-64]. The production of carbon dioxide and water is an indication of the environmental friendliness of this process.

2.5 Quantitative analysis of dyes

In photocatalytic degradation experiments, Rhodamine B has been often used as a model dye when different synthetic photocatalysts are tested for their photocatalytic activity [65, 66]. During the test of photocatalytic activity, the progress of the degradation is commonly followed by techniques such as UV-Vis absorption spectroscopy, HPLC and mass-spectrophotometer. A summary of the type of information that these analytic techniques provide is given below.

2.5.1 UV-Vis absorption spectroscopy

UV-Vis absorption spectroscopy is routinely used in photocatalysis because dyes are composed of a high degree of conjugation (i.e. alternating double and single bonds). The presence of π and n- electrons in their structure means that they can absorb light in both the visible and UV region of the solar spectrum [65, 66]. Upon absorption of either visible or UV light, the π and n- electrons can be excited to higher anti-bonding molecular orbitals [67, 68]. The excitation of the electrons is subsequently followed by the loss of energy as the electrons move from higher energy levels to lower energy levels. The relaxation of the electrons is detected in the UV-Vis absorption spectrum and it appears as a peak in a plot of absorbance against wavelength [69, 70]. The absorption peak of Rhodamine B occurs in the visible region (553 nm) of the solar spectrum (Figure 2.5).

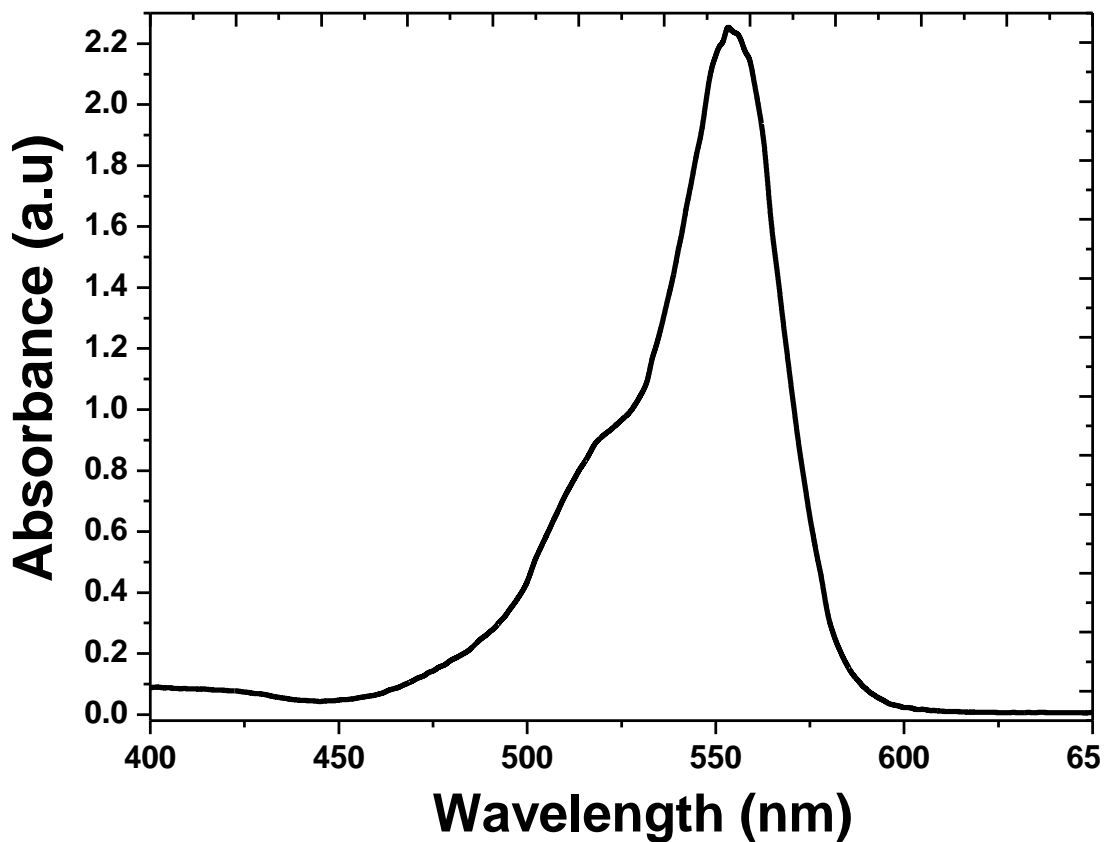


Figure 2.5: Typical UV-Vis absorption spectra of Rhodamine B.

It is this peak located at 553 nm that is used to monitor the progress of the degradation of the Rhodamine B dye using the Beer-Lambert's Law (eq. 2.9) [71].

$$A = \log_{10}\left(\frac{I_0}{I_f}\right) = \epsilon cL \quad \text{eq. (2.9)}$$

Where: A – Absorbance of dye solution, I_0 – Incident light intensity, I_f – Transmitted intensity, L – Cuvette path length and ϵ – Extinction coefficient. Beer-Lambert's Law therefore allows for the estimation of the concentration of the Rhodamine B dye solution that is measured at certain time intervals (Figure 2.6) using ZnO.

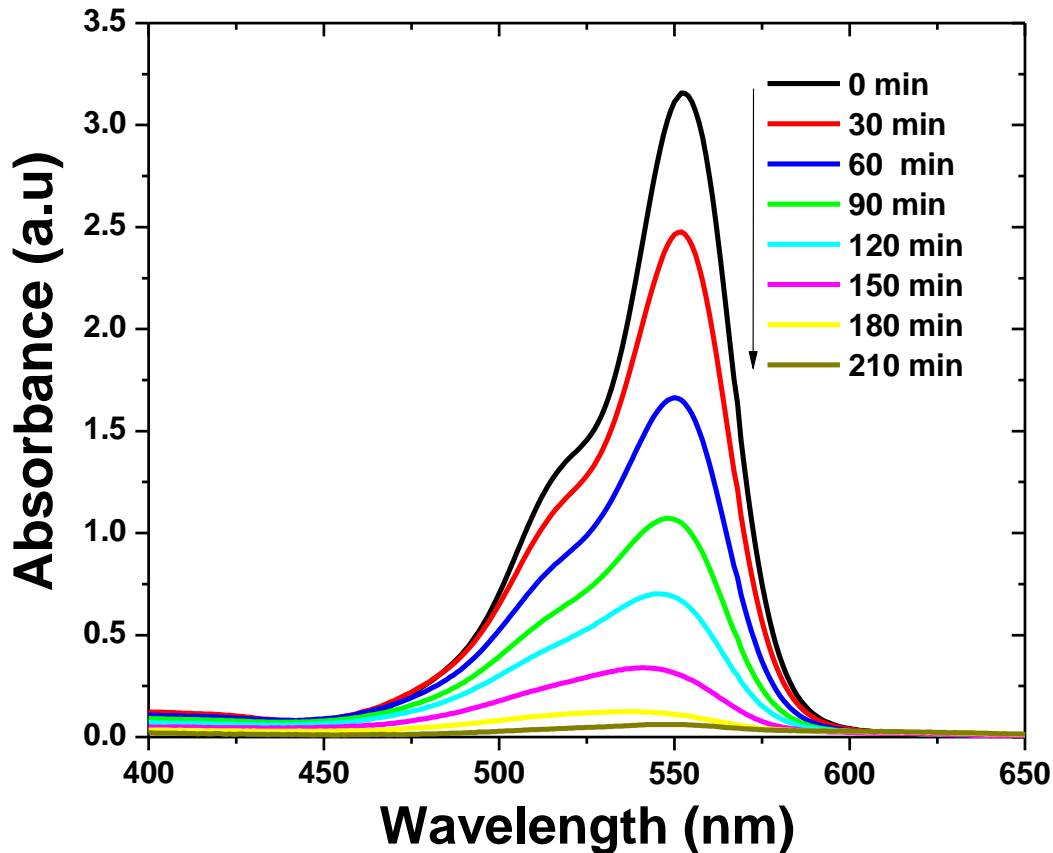


Figure 2.6: Time dependent changes of UV-Vis absorption spectrum of Rhodamine B during the degradation of the dye.

The decrease in the absorbance (i.e. concentration) of the absorption peak located at 553 nm for Rhodamine B is interpreted as indicating that the concentration of the dye is being reduced through time.

2.5.2 Mass spectrometry

The most common issue in the previously used method (e.g. Precipitation, Ozonation, etc.) for water purification was the inability to fully destruct dyes into less harmful counterparts [71]. Photocatalytic degradation is able to degrade the dyes into CO_2 , H_2O and inorganic salts [71]. This has opened a new area of research that focuses on quantifying the intermediates and final products produced during the degradation as a means of coming up with a degradation

mechanism. Using mass spectrometry has allowed for such studies to be a success. Mass spectrometry's application in photocatalysis is based on its ability to measure molecular masses of organic compounds present in a sample [72, 73]. It measures the molecular masses by ionizing the compounds upon exposure to electrons such that the ions are sorted out by their mass-to-charge ratio. When they have reached the detector, the results come out in a form of an ion signal to mass-to-charge ratio [74]. Tayade et al. [75] proposed a degradation mechanism based on results obtained from LC-MS analysis that was done on aliquots that were collected at different time intervals during the course of the photocatalytic degradation of Rhodamine B. The proposed mechanism of Rhodamine B is illustrated in Figure 2.7 [75].

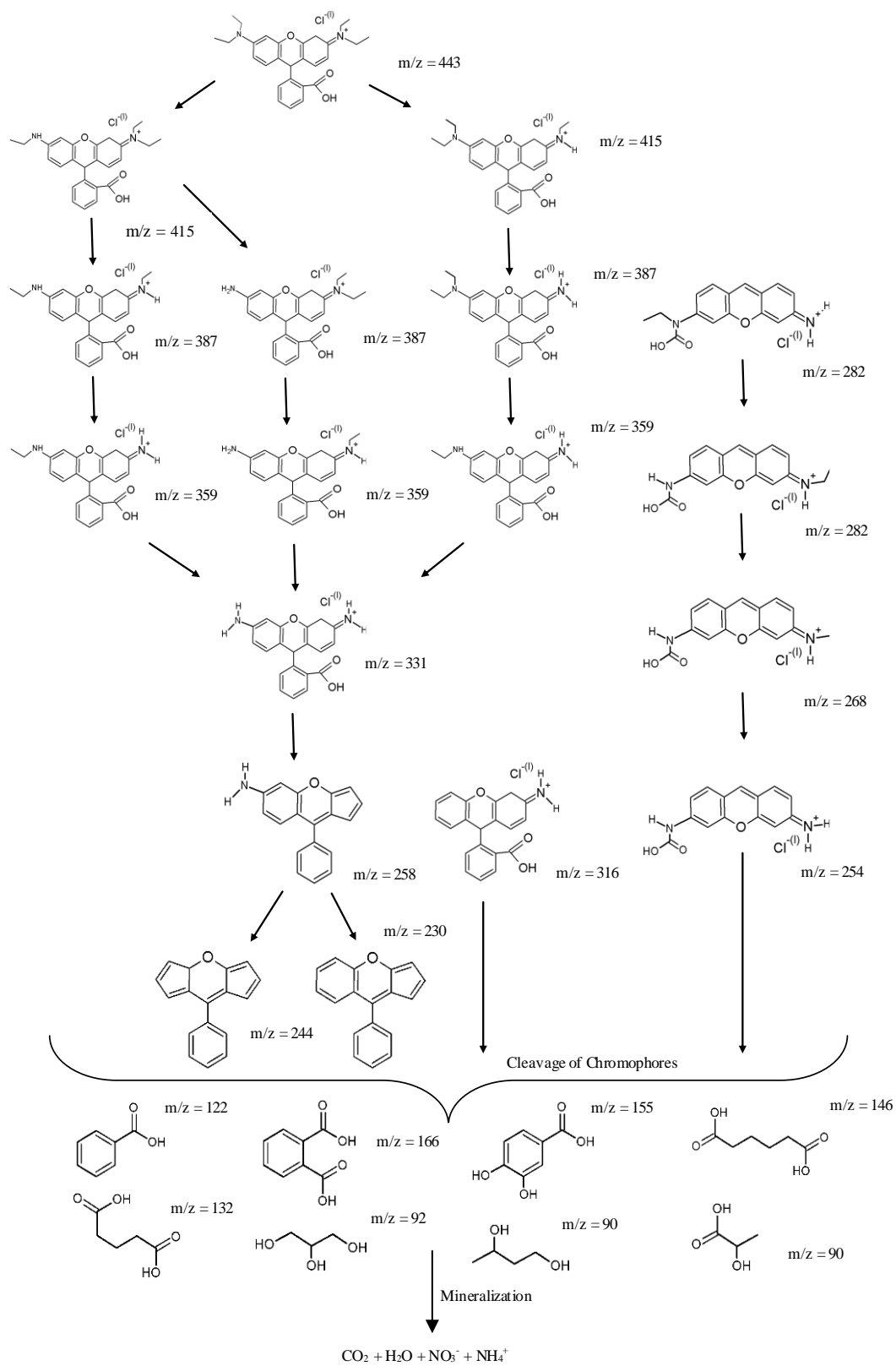


Figure 2.7: Photocatalytic degradation mechanism of Rhodamine B [48].

They reported that the degradation first occurs by the N-de-ethylation of Rhodamine B. The N-de-ethylation mechanism was proposed due to the presence of N-deethylated intermediates as detected by HPLC. The intermediates detected were N,N-diethyl-N'-ethylrhodamine (DER), N,N-diethylrhodamine (DR), N-ethylrhodamine (ER), and rhodamine (R) [76]. The products of the N-de-ethylation are oxidized to butane-1,3-diol, propane-1,2,3-triol, 2-hydroxypropanoic acid and adipic acid. The acids produced by the oxidation are then mineralized to H₂O, CO₂, NH₄⁺ and NO₃⁻ [76, 77].

2.5.3 High Pressure Liquid Chromatography

Liquid chromatography involves the injection of a certain amount of solution into a tube that is filled with a stationary phase made up of a very porous material. Once the solution is injected, the individual components in the solution travel inside the tube by the liquid which is moved by the force of gravity [78, 79]. The components in the solution interact differently with the stationary phase via chemical and physical interactions and hence will be separated inside the column. As a result of the different interactions with the stationary phase, the components will exit the column at different times and can be analysed by an external detector [78, 79]. The detector can be a spectrophotometer that measures the colour's intensity or by a device capable of determining the quantity of each component in the solution. The parameter used in HPLC to identify compounds in the solution is called retention time and is characteristic of each compound. Using this technique, the progress of degradation can be followed through time [78, 79]. An output from HPLC is called a liquid chromatogram, and it gives the time at which a component, shown as a peak, is eluted from the column [78, 79]. In a study done by AlHamedi et.al [80], on the degradation of Rhodamine B in the presence UV/H₂O₂. In their study, 50 mL of the dye solution being degraded was withdrawn at 30 min intervals. The organic component was extracted using dichloromethane. Upon analysis using HPLC, it was observed that the actual breakdown of the Rhodamine B resulted in low molecular weight aliphatic alcohols and acids [80].

2.6 The effect of operational parameters on the photocatalytic degradation efficiency

To get a better understanding of the behaviour of a photocatalyst used in photocatalytic degradation of dyes, it is important to know how it behaves under different environmental conditions. This understanding allows for optimum conditions to be implemented during its application allowing for maximum efficiency from the photocatalyst. In dye degradation studies, the important parameters that affect the efficiency of a photocatalyst include catalyst loading, dye concentration, solution pH and light intensity [81]. The effect that these operational parameters are outlined in the following subsections.

2.6.1 Catalyst loading

The determination of the optimum amount of catalyst that must be used during a reaction is important because it prevents catalyst wastage when it is used with the notion that more catalyst results to high reaction rate. A variety of research groups have proven that the highest amount of catalyst used cannot always be correlated with high photocatalytic degradation rates [82, 83]. Daneshvar et al. [84] studied the effect of catalyst loading on the rate of degradation of acid red 14 (AR14). They reported a steady increase in the rate of degradation for up to 160 ppm ZnO concentration, after which the rate decreased for concentrations above 160 ppm [84]. Kansal et al. [85] reported a study where the catalyst concentration was varied from 0.25 to 2.0 g/L for dye solutions of 25 mg/L at a natural pH (6.4 for Methyl Orange (MO) and 5.97 for Rhodamine 6G (R6G)). The optimum dose for R6G was found to be 0.5 g/L, while that of MO was 1 g/L. The authors reported that the degradation rate did not increase linearly with increasing catalyst dose [85]. Daneshvar et al. [84] and Kansal et al. [85] attributed the mild decrease in degradation efficiency at very high catalyst concentration to be due to increased turbidity of the dye-catalyst suspension which hinders the amount of photo excitation needed in dye degradation. It has also been suggested that at high catalyst concentration there might be an increase in the amount particle-particle interaction causing agglomeration and hence a reduced portion of active sites will be exposed [86].

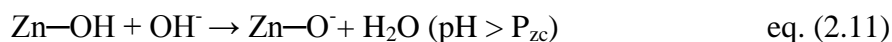
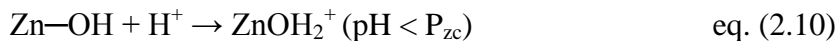
2.6.2 Dye concentration

A strong dependence between the dye concentration and the rate of degradation has been previously established [87, 88]. Studying this relationship is important because it allows the determination of the rate of the reaction (i.e. rate constant) using kinetics models [89]. In the majority of the studies reported in literature, an inversely proportional relationship exists between the concentration of the dye and the rate of dye degradation [89]. It is reported that the decrease in the rate of the reaction as the concentration of the dye is increased is due to the insufficient amount of hydroxyl radicals generated to degrade the large number of dye molecules available at high concentration of the dye. The decrease in the degradation rate is also said to be due to increased opacity in the dye solution which prevented light from reaching the surface of the photocatalyst [90]. Kansal et. al. [91] reported on the effect of dye concentration on the degradation of Reactive Black 5 (RB5) and Reactive Orange 4 (RO4). The concentration was varied from 10 to 100 mg/L and it was noted that in the case of RB5, for dye solutions of 10 and 25 mg/L, 100% decolourization occurred within 5 and 7 min, respectively, and in the case of 50 mg/L, almost complete degradation was observed in 30 min, and it gets further decreased on increasing the concentration of dye. Similar trend was observed in the case of RO4, where complete decolourization of 25 mg/L dye under optimized conditions [91]. The possible explanation for this behaviour was that as the initial concentration of the dye increased, the path length of the photons entering the solution decreased and in low concentration the reverse effect was observed, thereby increasing the number of photon absorption by the catalyst in lower concentrations [91]. The same effect was observed by Neppolian et al. [92] during the photocatalytic degradation of three commercial textile dyes: Reactive Yellow, Reactive Red, and Reactive Blue [92].

2.6.3 Solution pH

Coloured wastewater that is released into the environment exists at different pH conditions. The pH of the solution is important because it affects the surface charge of the photocatalyst which in turn affect the rate of degradation of the dye [93]. This effect of pH on degradation efficiency has

been explained by various researchers. They have based their explanation on the point of zero charge (P_{zc}) together with the high rate of dissolution of ZnO at certain pH of the dye solution. The point of zero charge of ZnO is ± 8.6 and hence its surface is positively charged below pH 8.6, and negatively charged above pH 8.6 (eq. 10 and 12).



The changes in the pH of the dye solution not only change the surface charge of the ZnO photocatalyst, it also changes the charge of the dye molecules. Since the degradation process requires that there be interaction between the dye molecules and photocatalyst, electrostatic interactions are bound to play a role in determining the efficiency at which a dye is degraded [94-96]. In the case of Rhodamine B, a cationic (basic) dye, its molecules at high pH are susceptible to adsorption to the negatively charged photocatalyst surface which results to an increased rate of dye degradation. Reduced degradation efficiency is expected at low pH due to the force of repulsion that exists between the positive photocatalyst surface and the cationic dye molecules. At high pH values, there is also an increased amount of OH^- ions in solution. The OH^- ions can be easily converted into the hydroxyl radicals responsible for the degradation of the dye molecules which results to high degradation rates [97-99]. Due to the diverse roles of pH, Kazeminezhad and Sadollahkhani [100] studied the effect of pH on the degradation rate of Rhodamine B and Methyl Blue at three pH values (4, 8, and 11). The authors reported that the optimum pH for Rhodamine B and Methyl Blue was 4 and 11, respectively. The difference in the adsorption ability of the different dyes at different pH values indicate the influence that the pH have on the properties of both the ZnO photocatalyst and the dye molecules [100].

2.6.4 Light intensity

The effect of light intensity on the photocatalytic degradation of dyes is important in the utilization of ideal experimental conditions. The intensity of light that is used influence the rate at which photo excitation occurs on the photocatalyst surface [101]. It is important to consider the fact that the sunlight intensity varies depending on weather conditions. Hence, if this process

was applied in the environment using direct sunlight, it would be important to know the UV dose that is required for effective photo activation of the photocatalyst. Salin et al. [102] used light intensities of 6 W and 12 W using a UV lamp with 254 nm wavelength. The results obtained clearly indicated that increasing the intensity of the lamp resulted in improved rates of degradation. The authors attributed the increased degradation rate to the fact that high light intensity allowed for generation of many electrons and holes to the covalent band of ZnO. Chakrabarti and Dutta [103] performed the light intensity study using Methylene Blue and Eosin Y and reported the same trend observed by Salin et al. [102].

2.7 Basic properties of ZnO

The interest on studies based on ZnO arises from the well sort after properties it displays in a wide range of applications such as in transistors, photo-detectors and light emitting diodes [104]. Apart from the basic vital properties such as a wide band gap (3.37 eV) corresponding to UV light of 387 nm, high exciton binding energy (60 meV) and its high sensitivity to light, ZnO comes with added advantages of being readily available, non-toxic in nature, stable in a wide range of environmental conditions and being very cheap to produce [105, 106]. As a wide band gap semiconductor, it is capable of absorbing UV light of the solar spectrum [107]. The ability to absorb light from the solar spectrum becomes important when it is used in photovoltaics by using the freely, environmentally friendly energy from the sun. Room temperature exciton emission that is observed in ZnO is made possible by its high exciton binding energy which is an important property when considering using a semiconductor material as a photocatalyst [108]. ZnO occurs in three different crystal structures namely; rocksalt, wurtzite and zinc blende. Rock salt (NaCl) is a metastable form which is stable only at very high pressure (~ 10 GPa). The zinc blende crystal structure exists only when ZnO can be grown through epitaxial in a substrate that is composed of a lattice structure which is cubic. Wurtzite is the most common and stable phase of ZnO. As a direct band gap semiconductor with vast amount of ionic bonding, ZnO crystallizes in the hexagonal wurtzite structure under ambient conditions, with a lattice that belongs to the $P6_3mc$ space group [109]. The hexagonal lattice (Figure 2.8) is composed of a zinc atom which is located in between four oxygen atoms, and vice versa, with lattice constants of $a = 3.2495 \text{ \AA}$, $c = 5.2069 \text{ \AA}$ and a density of 5.605 g.cm^{-3} [110]. This results in interconnected sublattices of Zn^{2+} and O^{2-} forming tetrahedral coordinated planes arranged along hexagonal axis (c-axis) [110, 111]. As a result of the tetrahedral coordination, ZnO possesses polar symmetry along the hexagonal axis. Properties such as spontaneous polarizability and piezoelectricity are due to the polarity that exists in ZnO crystals. The wurzite ZnO structure has two common basal polar termination facets, polar O terminated $[000-1]$ and Zn terminated $[0001]$ facets which are oriented along the c-axis, together with two non-polar $[112\bar{0}]$ oriented along the a-axis and the $[10-10]$ facets which are made up of the same number of O and Zn atoms. The chemical and physical properties of the polar and non-polar facets in ZnO vary, with the polar facets being characterized by high surface energies as opposed to their non-polar counterpart [110, 111].

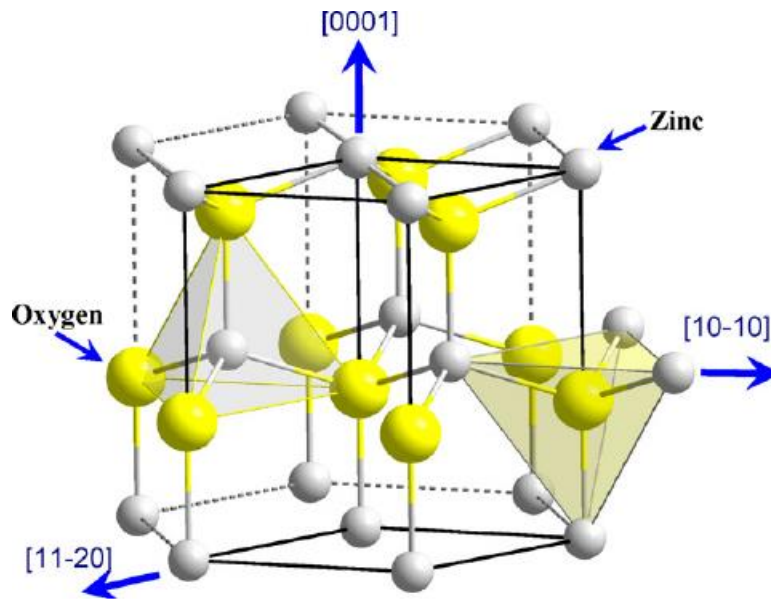


Figure 2.8: The wurtzite structure of zinc oxide [110].

The presence of polar surfaces is very important, particularly in photocatalysis. From surface energy measurements it has been determined that the polar surfaces of ZnO are positively charged [111, 112]. This is important from a photocatalysis viewpoint because it influences the interaction of the hydroxyl anions in solution during photocatalysis. It has been reported that when the proportion of the polar surface exposed in ZnO is maximized, the hydroxyl anions in aqueous solution during dye degradation experiments are easily attracted to the opposite charge that exists on the photocatalyst surface [113]. This strong interaction allows for the formation of more hydroxyl radicals which are the principal oxidizing species required for the speedy degradation of the dyes [113, 114]. A variety of researchers has since then conducted a series of experiments to synthesize morphologies that possess the [0001] and the [000-1] polar surfaces [115, 116].

2.8 Synthesis of ZnO nanocrystals

The drive for human kind to come up with new ways of solving problems, and design synthesis methods that have the potential to produce high yields at relatively low cost, under environmentally friendly conditions, has gave rise to a lot of advancement in the field of nanotechnology. Nano-sized materials have been synthesized by a variety of methods which produce products with different physical (i.e. shape and size) and optical (i.e. band gap energy) properties. This section introduces some of the methods that are commonly used to synthesize ZnO nanoparticles.

2.8.1 Sol-gel Method

Typically, synthesis using the sol-gel method (Figure 2.9) involves dissolving a zinc metal salt (e.g. $\text{Zn}(\text{CH}_3\text{COO})_2 \cdot 2\text{H}_2\text{O}$) precursor in an organic solvent (ethanol) or water. The mixture is subsequently titrated with a basic solution (e.g. NaOH/KOH) which acts as a precipitating agent allowing for the formation of a sol-gel.

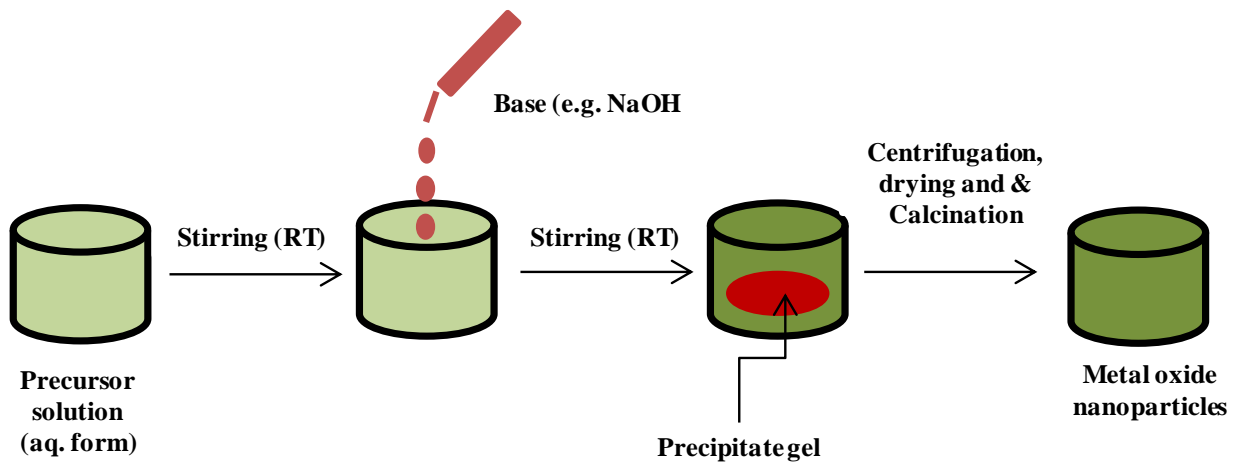


Figure 2.9: Typical flow diagram for sol-gel synthesis method.

The resulting solid-liquid diphasic system is then separated through centrifugation which allows for collection and drying (i.e. calcination) of the solid component of the mixture yielding the desired nanoparticles [117, 118]. Alwan et al. [119] dissolved 12.6 g of $\text{Zn}(\text{CH}_3\text{COO})_2 \cdot 2\text{H}_2\text{O}$ in

400 mL double distilled water with continuous stirring. The resulting solution was heated to 50 °C, 600 mL of ethanol and 6 mL of H₂O₂ (% 47) was subsequently added, resulting to a clear solution. The clear solution was incubated for 24 h and dried and 80 °C in an oven. After washing several times with distilled water, the complete conversion of ZnO was achieved through drying of the nanoparticles in a hot air oven.

2.8.2 Hydrothermal Method

The synthesis of ZnO using the hydrothermal method is based on heating a mixture of substrates gradually to a certain temperature (100–300 °C) in a steel pressure vessel (Figure 2.10) for several hours/days at high pressure [120].

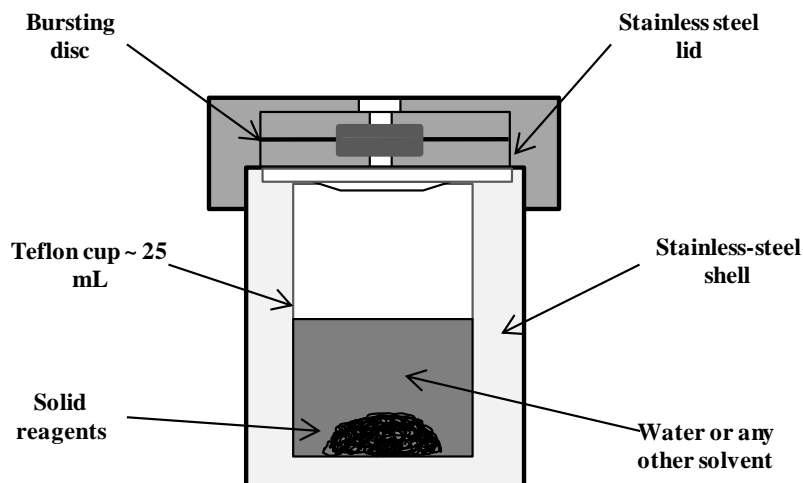


Figure 2.10: Schematic diagram of the hydrothermal synthesis method.

The heating under high pressure is followed by cooling which allows for crystal nucleation and subsequent crystal growth [120]. Such methods allows for growth of highly crystalline and pure single crystals that are not possible with other synthetic routes. Anesh et al. [121] prepared stock solutions (0.1 M) of Zn(CH₃COO)₂•2H₂O in 50 mL solution of methanol under stirring. To these stock solutions, varying concentrations of NaOH (0.2–0.5 M) prepared in methanol were added under continuous stirring to adjust the pH to between 8 and 11. The solutions were transferred into Teflon lined sealed stainless-steel autoclaves and heated under self-generated pressure at

temperatures in the range of 100–200 °C for 12 h. After the reaction was complete, they were allowed to cool naturally to room temperature, after which they were washed with methanol, filtered and dried at 60 °C in an oven. The results obtained indicated that there was a significant dependency between the nanoparticles morphologies and temperature. The size of the ZnO nanoparticles increased as the temperature for hydrothermal synthesis was increased. Baruwati et al. [122] used the hydrothermal method in which 2 g of $\text{Zn}(\text{NO}_3)_2 \cdot 4\text{H}_2\text{O}$ was dissolved in 200 mL of double distilled water. Ammonium hydroxide solution (25%) was used to adjust the pH to 7.5 under stirring and the mixture was continuously stirred for 1 h at room temperature. The mixture was then transferred into a Teflon lined stainless steel autoclave and heated for time periods in the range of 6–24 h at 120 °C. After the reaction, the autoclave was allowed to cool naturally to room temperature and the products washed multiple times using double distilled water. The resulting white powders were filtered and dried at 80 °C overnight.

2.8.3 Microwave heating method

Molecules having a permanent dipole moment or those possessing ionic conduction can be heated with energy in the form of electromagnetic waves [123]. When such molecules are exposed to an oscillating magnetic field, they will try and align with the field causing them to rotate. The constant agitation at molecular level as the polarity of the magnetic field is varied creates friction which heats up the molecules in a reaction mixture [123, 124]. This method has since received a lot of attention because it is capable of decomposing metal precursors rapidly resulting to shorter reaction times. Unlike conventional heating, in which a lot of energy is lost while heating the vessel containing the reaction medium, microwaves heat the precursor solutions directly (Figure 2.11) resulting to reduced energy consumption and very pure products [125].

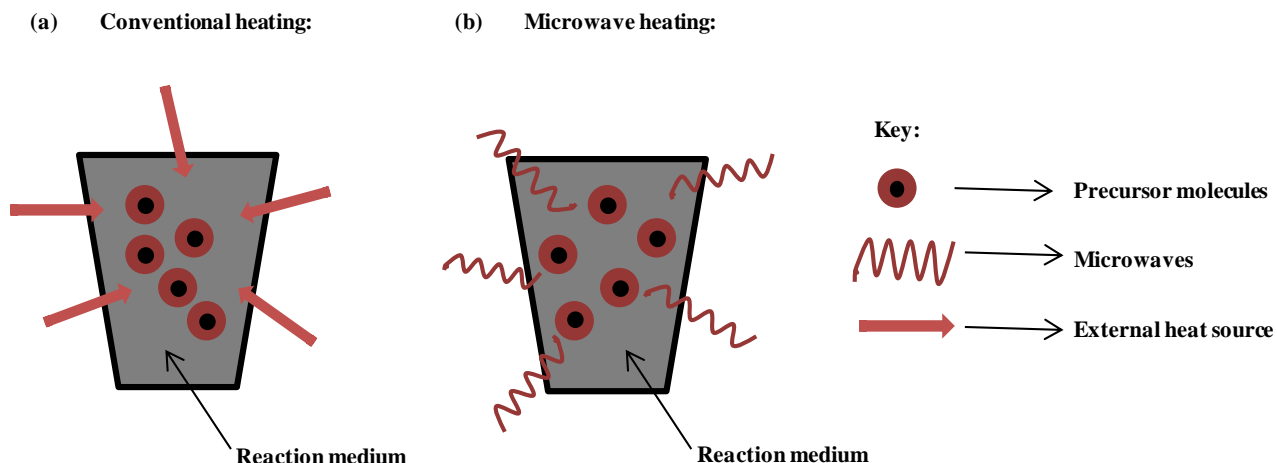


Figure 2.11: A diagram showing the different interaction of the heat source with the reaction medium during (a) conventional and (b) microwave heating.

Some of the known advantages of using microwave heating method over conventional synthesis are (1) high reaction rates, (2) ability to easily control reaction conditions, (3) different absorbing properties of reagents allow for good reaction selectivity, (4) high product yields, and (5) simple handling and easy optimization of reaction parameters [126]. Barreto et al. [126] employed microwave synthesis in which a zinc metal salt ($\text{Zn}(\text{CH}_3\text{COO})_2 \cdot 2\text{H}_2\text{O}$, $\text{Zn}(\text{NO}_3)_2 \cdot 4\text{H}_2\text{O}$ or ZnCl_2) was dissolved in 32 mL of deionized water or sodium di-2-ethylhexyl-sulfosuccinate. The resulting mixture was titrated with base (KOH, NaOH, or NH_4OH) for 2 min under continuous stirring (10 min) at room temperature. The colloidal solution was transferred into Teflon autoclaves and microwaved in a temperature controlled mode in a microwave accelerated system (Mars-X) operated at different powers (300, 600, and 1200 W) for a certain period of time (5, 10, or 20 min). The results indicated that changing the base used influenced the morphology of the nanoparticles and that longer reaction time was required in order to form well defined structures with homogeneous morphology and particle size [126].

2.9 Synthesis parameter affecting the properties of ZnO nanocrystals

The optical and structural properties of ZnO nanoparticles are highly controlled by the conditions under which they are synthesized. A lot of effort has been invested into understanding the way in which reaction parameters influence the resulting properties during synthesis [127, 128]. The commonly studied parameters during synthesis such as reaction time, type of precursor, pH of precursor are briefly described below. The ability to synthesize ZnO nanoparticles possessing excellent optical and structural properties is very important for industrial applications. Hence, getting a better understanding of how each parameter can be manipulated to get the desired result is imperative.

2.9.1 Reaction time

The period of time in which a reaction is run has been reported to be of great importance in determining the final size of the nanoparticles. Generally, synthesis of smaller sized particles is favoured by shorter reaction times. Longer reaction time provides enough life span for the formation of larger particles which tend to form much larger aggregates (Figure 2.12) [129].

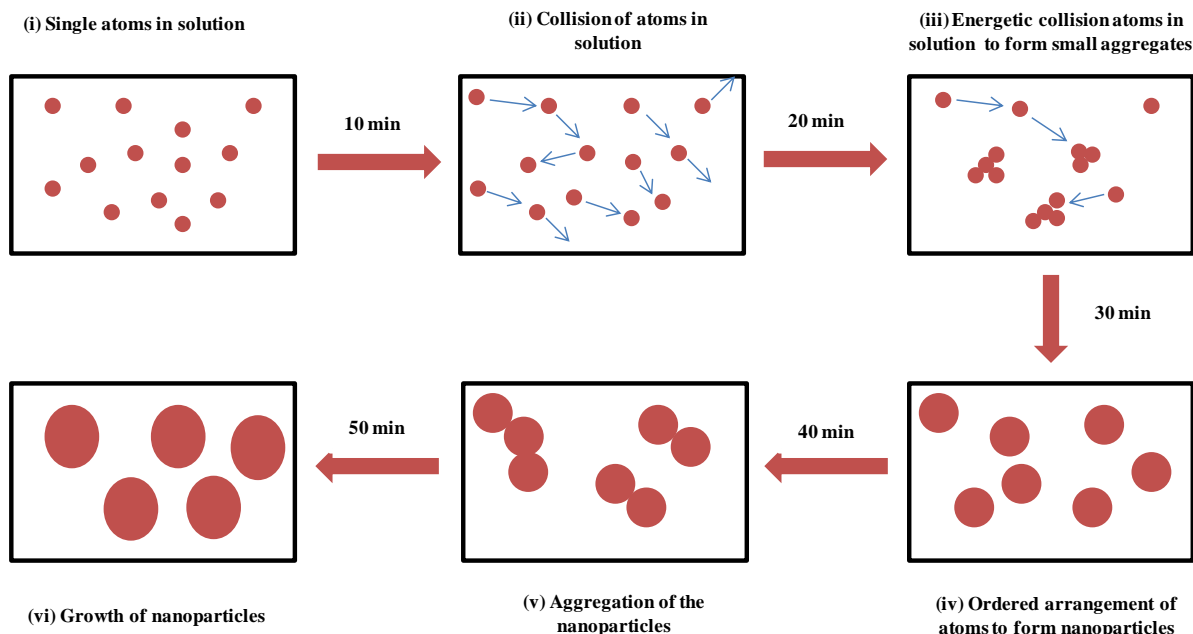


Figure 2.12: Growth of nanoparticles in an aqueous solution with time.

The relationship between particle size and time can be explained using the Ostwald ripening mechanism. According to the Ostwald ripening mechanism, during a reaction, different sized particles exist in the reaction medium. The smaller sized particles, being highly unstable, tend to aggregate to form bigger particles. As a result of this, running a reaction time provides enough time for larger particles to form [130, 131]. Dutta [132] reported the synthesis of ZnO using a sol-gel method at 8, 10 and 12 h which resulted in the nanoparticles of different sizes. The nanoparticles synthesized at 8, 10 and 12 h were found to be 15.2, 17.8 and 26.52 nm, respectively. Barreto et al. [126] varied the microwave power (300, 600 and 1200 W) during synthesis which resulted in different reaction times. The size of the nanoparticles was found to be smaller when 1200 W was used as a result of the reaction running for a short period of time as opposed to when lower microwave power was used.

2.9.2 Type of precursor

ZnO nanoparticles can be synthesized using a variety of zinc metal salts such as $\text{Zn}(\text{CH}_3\text{COO})_2 \cdot 2\text{H}_2\text{O}$, $\text{Zn}(\text{NO}_3)_2 \cdot 6\text{H}_2\text{O}$, ZnCl_2 and $\text{ZnSO}_4 \cdot \text{H}_2\text{O}$. The difference in these zinc metal salts is the type of counter anion (NO_3^- , CH_3COO^- , Cl^- , and SO_4^{2-}) in the precursor. The counter anion variation has allowed a variety of researchers to systematically study the effect it has on the optical and structural properties [132]. The growth of ZnO nanocrystals is sensitive to the type of precursor used because different counter anions have different abilities to coordinate with the different crystal planes of ZnO in a reaction medium [133, 134]. As a result of the different adsorption behaviours of the counter anions, different sizes and morphologies can be synthesized under the same experimental conditions, with only the precursor being varied. Ozel et al. [135] conducted a study on the effect of the type of precursor on ZnO formation and the development of the morphology during hydrothermal synthesis. They found that the morphology was strongly dependent on the type of precursor used during synthesis. Results indicated that when ZnCl_2 was used, ZnO took on an ellipsoidal rod like form with taped ends while when $\text{Zn}(\text{NO}_3)_2 \cdot 6\text{H}_2\text{O}$ was used, branched rod like particles were produced. In literature, the different morphologies observed are explained based on the nature of attachment of the $\text{Zn}(\text{OH})_4^{2-}$ monomers on the ZnO nuclei during growth. The different crystallographic planes in ZnO possess different growth kinetics, this means that the rate at which the $\text{Zn}(\text{OH})_4^{2-}$ monomer deposit to the different crystallographic planes is different [136, 137].

2.9.3 pH of the solution

Solution growth synthesis method of ZnO is based on using a zinc metal salt as a precursor and a precipitating agent (i.e. basic solution). A mixture of the zinc metal salt and a precipitating agent result in the formation of a precipitate that is further converted into ZnO through heat treatment at appropriate temperature [138]. The base in such reactions also acts as a reagent that is used to adjust the pH of the solution to the desired value. The amount of base added to the precursor solution has the potential of changing the resultant shape and size of the nanoparticles during synthesis. The effects of pH on the properties of ZnO emerge as a result of the fact that the amount of pH determines the concentration of the $\text{Zn}(\text{OH})_4^{2-}$ available for formation of ZnO nanocrystals [139]. At high pH conditions, large aggregates of the precipitate are generated (i.e. high $\text{Zn}(\text{OH})_4^{2-}$ concentration), and due to their proximity to one another, contact between them allows for faster growth. Lower pH allows for formation of much smaller nanoparticles due to the limited amount of the monomers in solution [139, 140]. Pung et al. [141] synthesized rod-like, rice-like and disk-like ZnO nanoparticles using sol-gel method. The different morphologies were achieved by varying the concentration of ammonia during synthesis which resulted in different morphologies with different photocatalytic activity.

2.10 Physical properties influencing the activity of a ZnO photocatalyst

A variety of photocatalysts, although active in degrading organic dyes, face a variety of drawbacks which causes them to become less active when used. Such drawbacks are associated with how the photocatalysts are prepared as it controls the resulting properties. These properties such as the surface area, exciton life span, and morphology play an important role on how a photocatalyst behaves upon application in a real life situation. Through varying certain reaction parameters such as reaction time, doping, and changing pH during synthesis, these properties can be tuned in order to get the best efficiency from a photocatalyst [142].

2.10.1 Surface area

Apart from the conditions of the reaction under which a photocatalyst is used, its photocatalytic activity is also controlled by properties such as its morphology, surface area and crystallinity [143]. The surface area of a photocatalyst is by far the most influential factor which has been extensively studied in the field of photocatalysis. It is used to quantify the amount of exposed/available active sites on the surface of photocatalysts which are available for catalytic reactions to take place in them [144]. This property of a photocatalyst has been important to study due to the fact that for dyes to be degraded, the molecules of the dye need to come into contact with the surface of the photocatalyst in order to be adsorbed. It is only when the dye molecules have come into contact with the photocatalyst that the oxidizing/reducing species ($\text{OH}\cdot$ and h^+) generated on the photocatalyst surface can react with them allowing for the degradation process to commence [145, 146]. As a result of this, surface area is a vital property which controls the efficiency of a photocatalyst. The higher the surface area, the higher is its efficiency in the degradation of dyes [146]. The surface area, being such an important factor in the efficiency of a photocatalyst, has had various methods being employed in order to improve it. Reducing the length in which a reaction is run has seen the size of nanoparticles being reduced into the nano-meter region. Flores et al. [147] conducted a study on the effect of pH on the optical, structural and photocatalytic properties of ZnO. The nanoparticles synthesized at various pH values were found to have surface areas of 3.83, 6.43, 9.31, and 18.88 $\text{m}^2\cdot\text{g}^{-1}$. Photocatalytic

degradation studies of Methylene Blue showed an improved rate of degradation when the ZnO nanoparticles with surface area of $18.88 \text{ m}^2.\text{g}^{-1}$ were used. Similar results of high degradation rates at high surface area have also been reported by Cheng et al. [148], Wang et al. [149].

2.10.2 Non-metal anionic impurities

Completely mindful of the various properties of ZnO that has made it to be known as one of the best photocatalysts; its activity is limited due to its short exciton life time and its wide band gap (3.2 eV) which both allows for vast amount of electron-hole recombination to take place during photocatalysis [150]. The high rate of electron-hole recombination can be reduced by introducing an impurity in a form of a non-metal such as sulphur, carbon and nitrogen in the substitutional sites in the crystal lattice of ZnO [151]. Due to the close proximity of these non-metals to oxygen in the periodic table, substitution occurs without the change in the crystal structure of ZnO. The introduction of these types of dopants results to narrowing of the band gap, allowing photoexcitation at lower energy radiation [152, 153]. This method of improving the photocatalytic activity of a photocatalyst has also been reported for another wide band gap photocatalyst such as TiO_2 [154]. An attempt has also been made to improve the photocatalytic activity by introducing transition metals such as manganese, vanadium and cobalt in the crystal structure of ZnO. Transition metal dopants results to increase of carrier recombination centres and thermal instability and hence more focus are now mainly based on non-metal dopants [155]. Qiu et al. [156] prepared pure and nitrogen doped ZnO tetrapods for application in the degradation of Bisphenol A. The nitrogen doped ZnO were found to be more effective in degrading Bisphenol A than the pure ZnO. The authors postulated that this is caused by the ability of the nitrogen to reduce the bang gap of ZnO and thus enhancing its light absorbing ability in the visible region of the solar spectrum.

2.9.3 Morphology

The proposed mechanism on how dyes are degraded is explained in section 2.3. In this mechanism it is clearly stated that in order for the dye molecules to be degraded, they need to first come into contact with the surface of the photocatalyst. This means that the nature of the surface, which is known as the morphology, will control how the dye molecules interact with it. ZnO morphology can be changed by varying reaction parameters such as the pH of the precursor, type of precursor, and the synthesis method. The important factor that separates different morphologies from one another is the proportion of polar (i.e. [0001] and [000-1]) and non-polar (i.e. [1000], [0010] facets exposed on the surface of the nanoparticles as shown in Figure 2.12 [157]. Figure 2.13 shows two different morphologies where by the rod-like morphology has a smaller proportion of the polar [0001] and [000-1] facets on its surface then the hexagonal morphology.

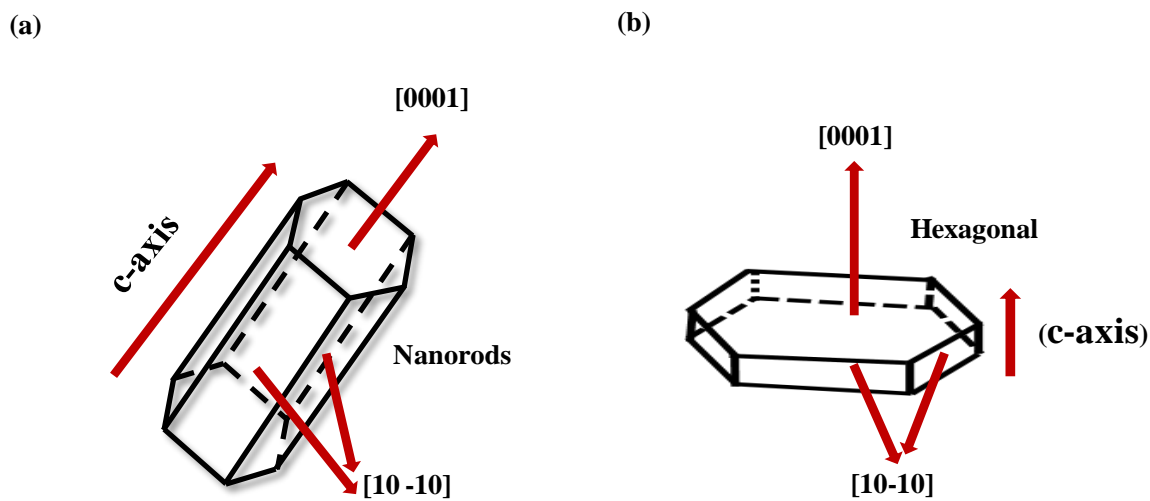


Figure 2.13: Illustration of the different types of crystal facets exposed in ZnO nanoparticles with respect to its morphological form.

The higher the amount of polar facets on the surface of certain morphologies (e.g. hexagonal and rodlike) has been reported to enhance the photocatalytic activity of ZnO. The enhanced photocatalytic activity result from the fact that polar facets have high surface energy, making

them positively charged. These facets are capable of attracting the hydroxyl anions in solution and transform them into hydroxyl radicals. As outline in section 2.3, it is the generated hydroxyl radicals that are responsible for degrading the dyes during photocatalysis [158]. Zhang et al. [159] compared hexagonal and spherical ZnO quantum dots in the degradation of Methylene Blue. The result indicated that in addition to high surface area, the special hexagonal morphology composed highly of Zn-terminated [0001] and O-terminated [000-1] polar facets was more efficient as a result of these facets ability to promote greater production of H_2O_2 and OH^\bullet .

2.11 Atom-mediated nucleation and growth mechanism of metallic nanoparticles in solution

The ability to control the method used to synthesize metallic nanoparticles is important because it allows for the optimization of the optical and structural properties of these crystalline materials for different applications in industry. Metallic nanoparticles are continually attracting a lot of attention from researchers in an attempt to improve their performance in a wide range of functional applications such as gas sensors, photovoltaics and photocatalysis [160, 161]. The current challenge that researchers are facing is that in order for new technological applications to be established, metallic nanoparticles need to be constructed in such a way that they are in the nanoscale region and have a controlled morphology and chemical composition. The chemical synthesis of metallic nanoparticles in solution is the most widely used method to synthesize materials whose properties can be controlled [162, 163]. Chemical synthesis has allowed a vast amount of studies to be conducted with the sole purpose of producing metallic nanoparticles of high quality at high yields which permits studies of the effect of morphology (i.e. shape and size) on the resulting properties to be a reality [164].

2.11.1 Nucleation and growth

Nucleation is defined as the first step that takes place in the formation of nanocrystals. It involves the coming together of precursor components (i.e. ions, atoms, and molecules) in such a way that they form a crystalline solid called a nucleus. The nuclei act as a site where more ions, atoms or molecules can deposit to aid the growth of the initial nuclei into a nanocrystal [165]. After nucleation takes place, there are two routes that can be followed for the growth of the metallic nanocrystal seeds. One pathway is the non-classical model that involves the formation of larger nanocrystal by the addition of small nanoparticles to one another. The other pathway is the classical model in which the atoms are added to the initially formed nanocrystal seeds [165].

2.11.2 Classical atom-mediated nucleation and growth

The classical atom-mediated nucleation and growth theory has been used for the past decades to understand how the morphology of metallic nanoparticles is controlled in chemical solution synthesis. The theory is based on the idea that for nucleation and growth to take place, the building blocks known as atoms must be present [166, 167]. The LaMer curve is used to describe the nucleation and growth processes which can be understood by looking at the evolution of the atomic concentration overtime. According to the LaMer curve, the nucleation and growth processes can be separated into three stages: atom production (stage I), nucleation from atoms aggregation (stage II), and nanocrystal growth from atoms addition (stage III), as shown in Figure 2.14 [168].

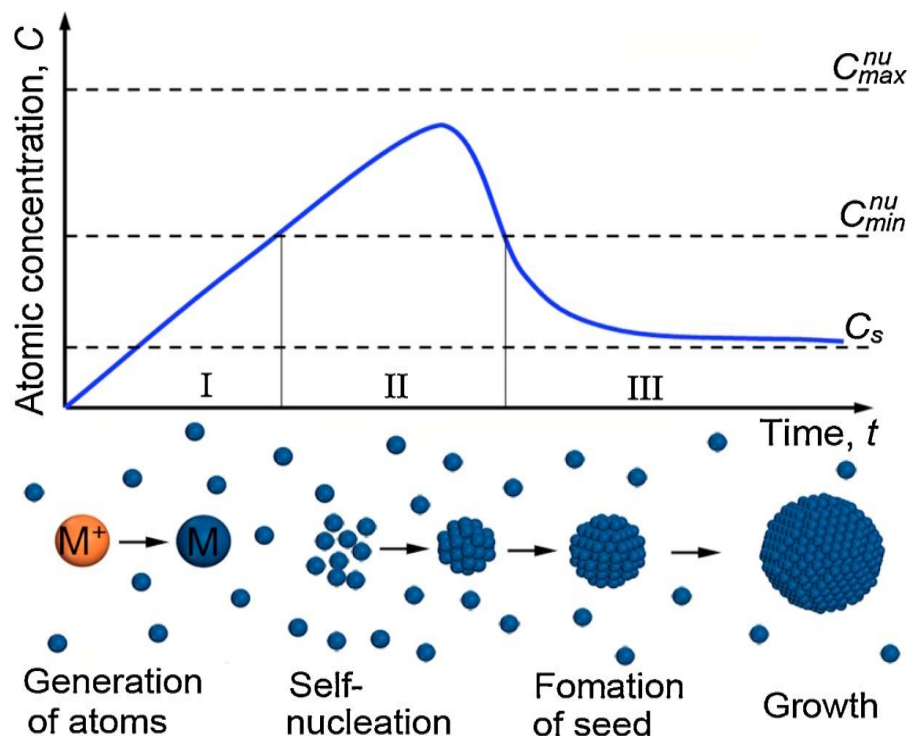


Figure 2.14: LaMer curve describing the metal nanocrystals formation stages in a reaction medium [168].

The initial stage involves the production of metallic ions through the thermal decomposition or reduction of organometallic compounds using reducing reagents. At the point where the concentration of the atoms surpass that at the point of supersaturation, the second stage initiates where the atoms begin to form small clusters of nuclei resulting in the formation of aggregates through homogeneous nucleation. As the atomic concentration slowly decreases, it goes below the minimum supersaturation level (C_{main}^{nu}) and nucleation stops to occur. In the third stage, the continuous addition of metallic atoms results to the increase in the size of the initially formed nuclei. The growth of the cluster above a certain critical size at this stage allows the clusters to be organized and locked into a well-defined structure due to the high activation energy available for structural fluctuation. The birth of the initial seed is achieved when the critical point is reached and the seed is allowed to grow further as the metal atoms are added to it until the nanocrystals solubility concentration (C_s) is decreased. The simplicity of the LaMer curve has motivated other various theories to be established and are discussed in the preceding sections.

These theories look at the nucleation and growth of nanocrystals in ways that are not fully described by the different stages explained by the LaMer curve [168-173].

2.11.3 Beyond the LaMer curve

The new theories for explaining nucleation and growth of nanocrystals has come about because of the discovery new plausible mechanisms on how metallic nanocrystals form. The newly proposed mechanisms for controlling the morphology of the nanocrystal are a small variation of the classical nucleation and growth theories [174]. The theories look at the behaviour of atoms as they change during nucleation and growth in response to different kinetic and thermodynamic parameters [175]. For example, the nuclei's intrinsic structure, which can be varied by changing the thermodynamic and kinetic parameters such as supersaturation concentration of the atoms, has very high control on the morphology of the nanocrystals. Other parameters such as the surface energy of the nanocrystals, the route of diffusion of atoms adjacent to the interface of the reaction, and the energy barrier encountered by atoms when they diffuse on the surface of the crystal, all play a significant role in the growth process of metallic nanocrystals [176-179]. Through in-Situ observations, it has been shown that single-, poly- and mesocrystalline nanoparticles can be formed by the aggregation of small nanoclusters that are capable of changing shape during growth. Thus new models that take into consideration of both cluster and nanoparticles as monomers for nanocrystals have been established [180].

To make a distinction, in this review nucleation and growth of metallic nanocrystals as described by the LaMer curve is defined as the “classical” model. The “non-classical” model defines the nucleation and growth that looks at nanoparticles and clusters as basic building blocks for metallic nanocrystals.

2.11.4 Non-classical nucleation and growth

2.11.4.1 Oriented Attachment (OA)

For the non-classical atom-mediated growth, the reduction of the overall energy to its lowest which takes place when two particles coalesce can be achieved by the alignment of the high energy facets of the two particles. Alternatively, the two particles can rotate such that they undergo alignment along the same crystallographic direction resulting to the minimization of the energy at the interface of the two particles. This mechanism is called Oriented Attachment and it describes how particles next to one another can self-organize spontaneously in such a way that allows them to share the same crystallographic direction, and subsequently followed by the particles joining at the point of contact [180-182]. The OA mechanism was first proposed by Penn and Banfield [183] in the study of the hydrothermal synthesis of anatase TiO₂ looking at its mechanism of formation. Using in Situ-TEM, the OA mechanism, based on Pt nanocrystals, has been proposed to occur as follows [184].

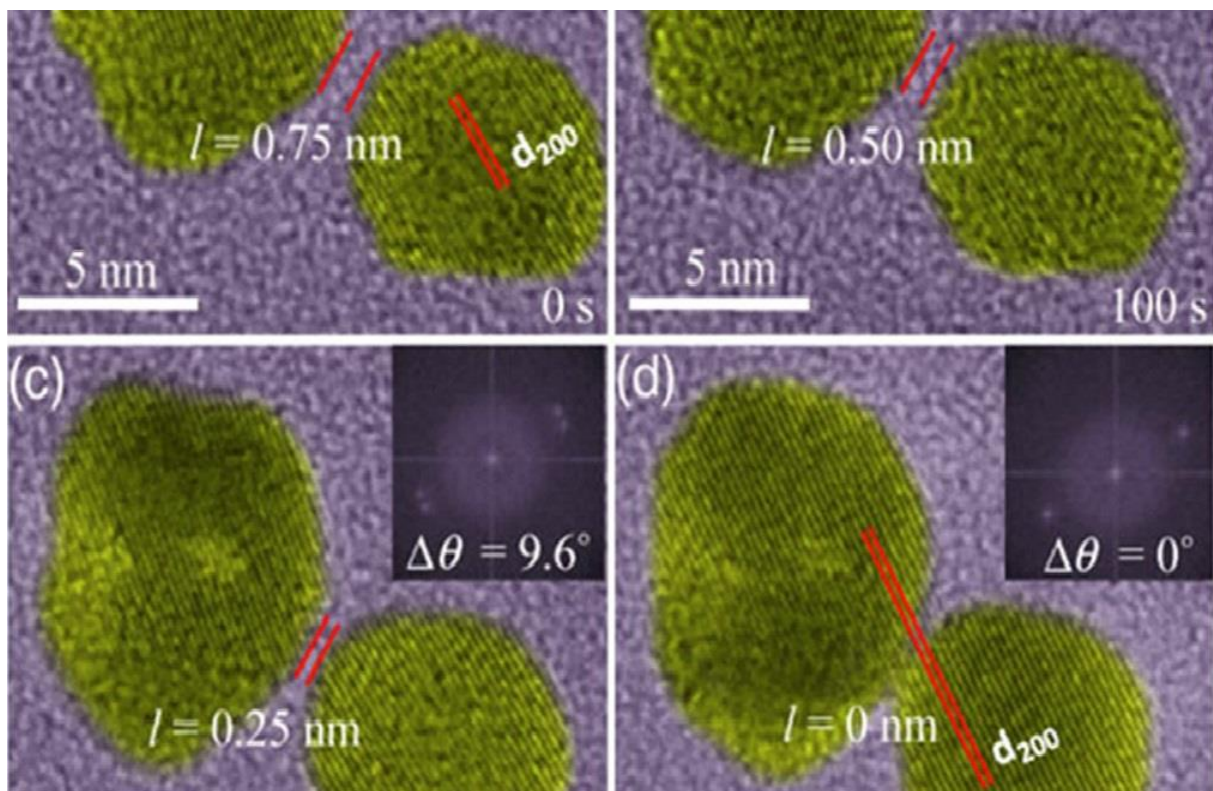


Figure 2.15: OA mechanism observed during growth of Pt nanocrystals [184].

The proposed mechanism stipulates that initially, the two adjacent nanocrystals move closer to one another. Through time, the distance between the Pt nanocrystals decreases from 0.75 to 0.25 nm. As they get closer, the nanocrystals start to rotate violently to a point where they form a well aligned dimer (Figure 15 (a-d)). The alignment is seen through the orientation of the d_{200} crystal planes. Unlike other semiconductor nanocrystals, such as CdSe/PbSe and GeTe, whose alignment occurs due to the presence of a permanent dipole moment, the nanocrystals from noble metals do not have permanent dipole moments to promote their alignment. Hence, the OA process is assumed to be as a result of a chemical bonding force [184].

2.11.4.2 Intraparticle Ripening (IR)

Attachment of two particles along a preferred crystallographic direction is not the only process known in particle-mediated growth, there is also transfer of atoms between particles that are attached. After particles undergo the OA process, the fusion of atoms located at the surface interface of the particles can result in the formation of a single crystal. The high energy atoms in certain locations of the particles rearrange in order to lower the systems total energy. This process is known as Intraparticle Ripening (IR) and was first introduced by Peng et al., [184] to describe the movement of atoms along the surface of the particles resulting to a change in morphology through time [184, 185]. Alivisatos et al., [186] has previously reported the attachment of Pt particles. When big and small particles come into contact, the atoms on the small particles move through the interface into the larger particles. Through time, the large particles get bigger and the small particle decrease in size and eventually disappear. In the case where the particles are of the same size, the diffusion of atoms from both particles towards each other result in the formation of a whole nanocrystal whose interface, where the particles are attached, is marked by a twin plane [186, 187].

Experimental and theoretical simulations of the formation of the twin plane revealed that the coalescence does not involve melting of the two particles, the dominant mass transport mechanism is considered to be surface diffusion. The IR mechanism was first observed by Uematsu et al. [188], where the morphology of the Au particles with a dumb-bell shape was transformed into spherical particles.

2.11.4.3 Overgrowth

In the atom-mediated growth mechanism, the attachment of the initially formed particles results to the formation of mesoparticles. The metallic ions and atoms that are left behind in the solution will aid overgrowth by attaching to the already formed mesoparticles. The LaMer curve (Figure 2.6) postulates that the nucleation and growth of the primary particles occurs in stage I and II when the concentration of the atoms is higher than $C_{\text{main}}^{\text{nu}}$. The concentration of the atoms decreases below $C_{\text{main}}^{\text{nu}}$, but not lower than the C_s , after which the primary particles aggregate to

form mesoparticles (stage III). Therefore, growth of the mesoparticles can continue through the atom-mediated route to the point where the concentration of the atoms goes below C_s (stage IV) [190].

2.11.4.4 Ostwald Ripening (OR) and Digestive Ripening (DR) mechanism

The description of the OR mechanism was first made public in 1900 by Ostwald, [191]. According to this mechanism, growth is initiated when the solubility of the nanoparticles undergo a drastic change. The change in solubility is highly dependent on the size of the nanoparticles. Larger particles are allowed to grow further as a result of the small particles solubility and surface energy being so high to such an extent that they re-dissolve and provide monomers for the larger particles. Researchers have come up with mathematical theories in describing the OR mechanism for reactions conducted in a closed system [192]. Contrary to the OR mechanism, DR mechanism describes nanoparticles growth to occur as a result of larger particles dissolving and depositing on the small particles allowing them to grow. High surface energy of the larger particles is believed to be the reason for the decrease in size of the larger particles [193].

2.12 References

- [1] S.S. Muthu, Textile Science and Clothing Technology, 1st Edition, pp 1-17, Springer Nature Singapore Pte LTD., Singapore (2017)
- [2] D. Jenkins, The Cambridge History of Western Textiles, 2003 Edition, pp 31-40, Cambridge University Press, United Kingdom (2003)
- [3] H. Lachheb, E. Puzenat, A. Houas, M. Ksibi, E. Elaloui, C. Guillard, and J. Herrmann, Applied Catalysis B: Environmental, **39**, (2002) 75–90
- [4] D. Gümüřand, and F.Akbal, Water Air and Soil Pollution, **216**, (2011) 117–124
- [5]A.R. Khataee, and M.B. Kasiri, Journal of Molecular Catalysis A: Chemical, **328**, (2010) 8-26
- [6] R. Pourata, A.R. Khataee, S. Aber, and N. Daneshvar, Desalination, **249**, (2009) 301–307
- [7] A. Aleboyeh, M.B. Kasiri, M.E. Olya, H. Aleboyeh, Dyes Pigments, **77**, (2008) 288–294
- [8] N. Daneshvar, D. Salari, and A.R. Khataee, Journal of Photochemistry and Photobiology A, **162**, (2004) 317–322
- [9] X. Jin, L. Ye, H. Xie, and G. Chen, Coordination Chemistry Reviews, **349**, (2017) 84–101
- [10] A.M. Ewlad-Ahmed, M.A Morris, S.V. Patwardhan, and L.T. Gibson, Environmental Science and Technology, **46**, (2012) 13354–13360
- [11] S. Radhika, and T. Jesty, Journal of Environmental Chemical Engineering, **5**, (2017) 4239–4250
- [12] X. Li, Y. Cheng, S. Kang, and J. Mu, Applied Surface Science, **256**, (2010) 6705–6709
- [13] S. Wang, and H. Li, Dyes and Pigments, **72**, (2007) 308-314
- [14] I. Watson, and A.D. Burnett, Hydrology: An Environmental Approach, Edition, pp 223-225, Lewis Publishers, Florida (1995)

- [15] I. Safarik, K. Nymburska, and M. Safarikova, *Journal of Chemical Technology and Biotechnology*, **69**, (1997) 1-4
- [16] M.V. Subbaiah and D. Kim, *Ecotoxicology and Environmental Safety*, **128**, (2016) 109–117
- [17] M. Mehrjouei, S. Müller and D. Möller, *Chemical Engineering Journal*, **263**, 2015, 209-219
- [18] M. Mehrjouei, S. Müller, K. Sekiguchi, D. Möller, *Ozone Science and Engineering*, **32**, (2010) 349–354.
- [19] K. Pirkanniemi, and M. Sillanpaa, *Chemosphere*, **48**,(2002) 1047-1060
- [20] M. Qamar, and M. Muneer, *Desalination*, **249**, (2009) 535-540
- [21] A.B. Patil, K.R. Patil, and S.K. Pardeshi, *Journal of Hazardous Materials*, **183**, (2010) 315-323
- [22] R.M. Christie, *Colour Chemistry*, 2nd Edition, pp 21-40, Royal Society of Chemistry, United Kingdom (2015)
- [23] H. Zollinger, *Color Chemistry: Syntheses, Properties, and Application of Dyes and Pigments*, 3rd Edition, pp 1-10, WILEY-VCH, Germany (2003)
- [24] A. Gurses, M. Acikyildiz, K. Gunes, and M.S. Gurses, *Dyes and Pigments*, 4th Edition, pp 51-55, Springer International Publishing, Switzerland (2016)
- [25] D.R. Waring, and G. Hallas, *The Chemistry and Application of Dyes*, 1st Edition, pp 17-33, Plenum Press, New York and London (1990)
- [26] M. Mark, *Handbook of textile and industrial dyeing*, 1st Edition, pp 8-17, Woodhead Publishing Limited, United Kingdom (2011)
- [27] N.N. Mahapatra, *Textile Dyes*, 1st Edition, pp 165-174, Woodhead Publishing Limited, India (2016)
- [28] J.A. Kiernan, *Biotechnology and Histochemistry*, **75**, (2001) 261 – 278

- [29] A.T. Peters, H.S. Freeman, *The Design and Synthesis of Organic Dyes and Pigments*, pp 1-55 Springer, Netherlands (1991)
- [30] H. Zangeneh, A.A.L. Zinatizadeh, M. Habibi, M.Akia, M. H. Isa, *Journal of Industrial and Engineering Chemistry*, **26**, (2015) 1-36
- [31] N.P. Raval, P.U. Shah, N.K. Shah, *Applied Water Science*, **7**, (2017) 3407–3445
- [32] S.D. Richardson, C.S. Willson, and K.A. Rusch, *Ground Water*, **42**, (2004) 678-688
- [33] R. Kubin, *Journal of Luminescence*, **27**, (1983) 455-462
- [34] C.G. Casey, *Journal of Physical Chemistry*, **92**, (1988) 6590-6594
- [35] A. Fujishima, K. Honda, *Nature*, **238**, (1972) 37-48
- [36] R. Wang, K. Hashimoto, A. Fujishima, M. Chikuni, E. Kojima, A. Kitamura, M. Shimohigoshi and T. Watanabe, *Nature*, **388**, (1997) 431-432
- [37] E.C. Butler and A.P. Davis, *Journal of Photochemistry and Photobiology A*, **70**, (1993) 273-283
- [38] R.I. Bickley, G. Munuera, and F.S. Stone, *Journal of catalysis*, **31**, (1973) 389-407
- [39] B.C. Faust, M.R. Hoffmann, and D.W. Bahnemann, *Journal of Physical Chemistry*, **93**, (1989) 6371-6381
- [40] K. Nakata, and A. Fujishima, *Journal of Photochemistry and Photobiology C: Photochemistry Reviews*, **13**, (2012) 169-189
- [41] C. BoonOng, L. YongNg, A.W. Mohammad, *Renewable and Sustainable Energy Reviews*, **81**, (2018) 536-551
- [42] H.Q. Sun, and S.B. Wang, *Energy Fuels*, **28**, (2014) 22-36
- [43] H.Q. Sun, S.B. Wang, H.M. Ang, M.O. Tade, and Q. Li, *Journal of Chemical Engineering*, **162**, (2010) 437-447
- [44] Y.H. Hu, and E. Ruckenstein, *Advanced Catalysis*, **48**, (2004) 297-345

- [45] J.D. Holladay, J. Hu, D.L. Kind, and Y. Wang, *Catalysis Today*, **139**, (2009) 244-260
- [46] E. Neyes, and J. Naeyens, *Journal of Hazardous Material*, **98**, (2003) 33-50
- [47] M. Muruganandham, R.P.S. Suri, M. Sillanpaa, J.J Wu, B. Ahmmad, S. Balachandran, and M. Swaminathan, *Journal of Nanoscience and Nanotechnology*, **4**,(2014) 1898-1910
- [48] I. Muthuvel, and M. Swaminathan, *Solar Energy Materials and Solar Cells*, **92**, (2008) 857-863
- [49] D. Sudha, and P.Sivakumar, *Chemical Engineering and Processing: Process Intensification*, **97**, (2015) 112-133
- [50] Y. Boyjoo, H. Sun, J. Liu, V.K. Pareek, and S. Wang, *Chemical Engineering Journal*, **310**, (2017) 537-559
- [51] E. Hong, D.K. Jung, and H. Kim, *Journal of Industrial and Engineering Chemistry*, **20**, (2014) 3869-3874
- [52] F. Zhang, J. Zhao, T. Shen, H. Hidaka, E. Pelizzetti, and N. Serpone, *Applied Catalysis B Environmental*, **15**, (1998) 147-156,
- [53] F. Vietmeyer, B. Seger, and P.V. Kamat, *Advanced Materials*, **19**, (2007) 2935–2940
- [54] B.Y. Wei, M.C. Hsu, P.G. Su, H.M. Lin, R.J. Wu, and H.J. Lai, *Sensors and Actuators B: Chemical*, **101**, (2004) 81–89
- [55] S.M. Alpert, D.R. Knappe, and J.J Ducoste, *Water Resour. Res.*, **44**, (2010) 1797-7808
- [56] S. Papić, N. Koprivanac, A.L. Božić, D. Vujević, S.K. Dragičević, and I. Peternel, *Water Environment Research*, **78**, (2006) 572-579
- [57] D. Ljubas, G. Smoljani, and H. Jureti, *Journal of Environmental Management*, **161**, (2015) 83-91
- [58] O.M. Alfano, D. Bahnemann, A.E. Cassano, R. Dillert, and R. Goslich, *Catalysis Today*, **58**, (2000)199-230

- [59] M.A. Fox, and M.T. Dulay, *Chemistry Reviews*, **93**, (1993) 341-357.
- [60] A.L Linsebigler, G. Lu, and J.T. Yates, *Chemical Reviews*, **95**, (1995) 735-758.
- [61] M. Yasmina¹, K. Mourad, S.H. Mohammed, and C. Khaoula, *Energy Procedia*, **50**, (2014) 559–566
- [62] R.I. Bickley, and F.S. Stone, *Journal of Catalysis*, **31**, (1973) 389–397.
- [63] P.V. Kamat, *Chemical Reviews*, **93**, (1993) 267–300.
- [64] M.A. Fox and M.T. Dulay, *Chemical Reviews*, **93**, (1993) 341–357
- [65] Q.I. Rahman, M. Ahmad, S.K. Misra, and M. Lohani, *Materials Letters*, **91**, (2013) 170-174
- [66] Z.L. Wang, and J.H. Song, *Science*, **312**, (2006) 242-246
- [67] W.U. Xiaohong, S.U. Peibo, L.I.U. Huiling and Q.I. Lili, *Journal of Rare Earths*, **27**, (2009) 739-743
- [68] S. Pung, X. Chan, S. Sreekantan and F. Yeoh, *Pigment and Resin Technology*, **45**, (2016) 408-418
- [69] R.J. Anderson, D.J. Bendell, and P.W. Groundwater, *Organic Spectroscopic Analysis*, 1st Edition, pp 1-10, The Royal society of Chemistry, United Kingdom (2004)
- [70] H.H. Perkampus, *UV-Vis Spectroscopy and Its Applications*, 1st Edition, pp 1-24, Springer-Verlag Berlin Heidelberg, Germany (1992)
- [71] H. Freiser, and M. Freiser, *Concepts and Calculations in Analytical Chemistry: A Spreadsheet Approach*, 3rd Edition, pp 212-215, CRC Press, United Kingdom (1992)
- [72] V. Meshko, L. Markovska, M. Mincheva, and A. E. Rodrigues, *Water Resolution*, **35**, (2001) 3357–3366
- [73] Z. Chen, D. Li, W. Zhang, Y. Shao, T. Chen, M. Sun, and X. Fu, *Journal of Physical Chemistry C*, **113**, (2009) 4433–4440

- [74] G. Lunn, and E.B. Sansone, Destruction of Hazardous Chemicals in the Laboratory, 3rd Edition, pp 1-34 John Wiley and Sons, United States of America (2012)
- [75] R.J. Tayade, T.S. Natarajan, and H.C. Bajaj, Industrial & Engineering Chemistry Research, **48**, (2009) 10262 – 10267
- [76] K. Yu, S. Yang, H. He, C. Sun, C. Gu, and Y. Ju, Journal of Physical Chemistry A, **113**, (2009) 10024-10032
- [77] W. Jo, and R.J. Tayade, Chinese Journal of Catalysis, **35**, (2014) 1781-1792
- [78] L.R. Snyder, J.J. Kirkland, and J.W. Dolan, 3rd Edition, Introduction To Modern Liquid Chromatography, pp 1-27, John Wiley and Sons, United States of America (2012)
- [79] W.J. Lough, and I.W. Wainer, High Performance Liquid Chromatography: Fundamental Principles and Practice, 1st Edition, pp 1-34, Chapman and Hall, United Kingdom (1995)
- [80] T. Rasheed, M. Bilal, H.M.N. Iqbal, H. Hu, and X. Zhang, **228**, Water Air and Soil Pollution, (2017) 291-101
- [81] M.H. Habibi, A. Hassanzadeh, and S. Mahdavi, Journal of Photochemistry and Photobiology A: Chemistry, **172**, (2005) 89-96
- [82] B. Neppolian, H.C. Choi, S. Sakthivel, B. Arabindoo, and V. Murugesan, Journal of Hazardous Material, **B89**, (2002) 303–317.
- [83] R.W. Matthews, Water Resolution, **24**, (1990) 653–660.
- [84] N. Daneshvar, D. Salari, D, and K. Alireza, Journal of Photochemistry and Photobiology A: Chemistry, **157**, (2003) 111-116.
- [85] S. Kansal, M. Singh, and S. Dhiraj, Journal of hazardous materials, **141**, (2007) 581-90
- [86] Y. Shavisi, S. Sharifnia, M. Zendezhaban, M. L. Mirghavami, and S. Kakehazar, Journal of Industrial and Engineering Chemistry, **20**, (2014) 2806–2813
- [87] L. Karimi, S. Zohoori, and M.E. Yazdanshenas, Journal of Saudi Chemical Society, **18**, (2014) 581-588

- [88] V. Subramanian, R.K. Roeder, E.E. Wolf, *Industrial and Engineering Chemistry Research*, **45**, (2006) 2187-2193
- [89] K. Aguilar, A. Garvín, and A. Ibarz, *Journal of Food Engineering*, **191**, (2016) 67-76
- [90] N. Yusoff, L. Ho, S. Ong, Y. Wong, and W. Khalik, *Desalination and Water Treatment*, **57**, (2016) 12496-12507
- [91] K.M. Parida, S.S. Dash, and D.P Das, *Journal of Colloid and Interface Science*, **298**, (2006) 787-793
- [92] B. Neppolian, H.C. Choi, S. Sakthivel, B. Arabindoo, and V. Murugesan, *Journal of Hazardous Materials B*, **89**, (2002) 303-312
- [93] P.R. Shukla, S. Wang, H.M. Ang, and M.O. Tade, *Separation and Purification Technology*, **70**, (2010) 338-344
- [94] J. Krishnan, A.A. Kishore, A. Suresh, B. Madhumeetha, and D.G. Prakash, *International Biodeterioration & Biodegradation*, **119**, (2017) 16-27
- [95] L.G. Devi, K.M. Reddy, *Applied Surface Science*, **256**, (2010) 3116-3121
- [96] S.B. Gajbhiye, *International Journal of Modern Engineering Research*, **2**, (2012) 1204-1208
- [97] R. Nagaraja, N. Kottam, C.R. Girija, and B.M. Nagabhushana, *Powder Technology*, **216**, (2012) 91-97
- [98] M. Sangareswari, and M.M. Sundaram, *Applied Physics A*, **123**, (2017) 364-372.
- [99] E. Engenidou, K. Fytianos, and I. Poulios, *Applied Catalysis B: Environmental*, **59**, (2005) 81- 89.
- [100] I. Kazeminezhad, and A. Sadollahkhani, *Journal of Materials Science*, **27**, (2016) 4206-4215
- [101] R. Kumawat, I. Bhati, and R. Ameta, *Indian Journal of Chemical Technology*, **19**, (2012) 191-194

- [102] H.M. Salin, Journal of Environmental Science and Engineering A, **4**, (2015) 395-400
- [103] S. Chakrabarti and B. Dutta, Journal of hazardous materials, **112**, (2004) 269-278
- [104] M. Willander, O. Nur, Q.X. Zhao, L.L. Yang, M. Lorenz, B.Q. Cao, M. Al-Suleiman, J. Perez, and C. Czekalla, **20**, (2009) 332001-332010
- [105] H. Kumar, and R. Rani, International Letters of Chemistry, Physics and Astronomy, **14**, (2013) 26-36
- [106] H. Lin, S. Liao, and C. Hu, Journal of Crystal Growth, **311**, (2009) 1378-1384
- [107] M.A. Behnajady, N. Modirshahla, M. Shokri, A. Zeininezhad, and H.A. Zamani, Journal of Environmental Science and Health Part A, **44**, (2009) 666–672
- [108] Z.M. Wang, Toward Functional Nanomaterials, 1st Edition, pp 1-77, Springer, United States of America (2009)
- [109] A.A.M. Elshaer, Molecular Beam Epitaxy Growth and Characterization of ZnO-based Layers and Heterostructures, 1st Edition, pp 8-13, Cuvillier Verlag, Germany(2008)
- [110] D. R. Lide, CRC Handbook of Chemistry and Physics, 73rd Edition, pp 1-34, CRC Press, New York (1992)
- [111] Y. Zhang, ZnO nanostructures: Fabrication and Applications, 1st Edition , pp 97-100, CPI GROUP (UK) Ltd, United Kingdom (2017)
- [112] S.S. Alias and A.A. Mohamad, Sythesis of Zinc Oxide by Sol-Gel Method for Photoelectro-chemical Cells, 1st Edition, pp 9-23, Springer, Singapore (2014)
- [113] Y. Chena, H. Zhao, B. Liu, and H. Yang, Applied Catalysis B: Environmental, **163**, (2015) 189-197
- [114] J. Yang, J. Wang, X. Li, J. Lang, F. Liu, L. Yang, H. Zhai, M. M. Ming, and X. Zhao, Journal of Alloys and Compounds, **528**, (2012) 28–33.
- [115] A. McLaren, T. Valdes-Solis, G. Li and S. C. Tsang, Journal of the American Chemical Society, **131**, (2009) 12540–12541

- [116] L. Xu, Y. L. Hu, C. Pelligra, C. H. Chen, L. Jin, H. Huang, S. Sithambaram, M. Aindow, R. Joesten, and S. L. Suib, *Chemistry of Materials*, **21**, (2009) 2875–2885
- [117] J.N. Hasnidawani, H.N. Azlina, H. Norita, N.N. Bonnia, S.Ratim, E.S. Ali, *Procedia Chemistry*, **19**, (2016) 211-216
- [118] A. Kargari, A. Tavakoli, and M. Sohrabi, *Chemical Papers*, **61**, (2007) 151-170
- [119] R.M. Alwan, Q.A. Kadhim, K.M. Sahan, R.A. Ali, R.J. Mahdi, N.A. Kassim, A.N. Jassim, *Nanoscience and Nanotechnology*, **5**, (2015) 1-6
- [120] H. Hayashi, and Y. Hakuta, *Materials*, **3**, (2010) 3794-3817
- [121] P.M. Aneesh, K.A Vanaja, and M.K. Jayaraj, *Proceedings of SPIE*, **6639**, (2007) 1352 - 1363
- [122] B. Baruwati, D.K. Kumar, and S.V. Manorama, *Sensors and Actuators B: Chemical*, **119**, (2006) 676-682
- [123] A.K. Singh, and U.T. Nakate, *Advances in Nanoparticles*, **2**, (2013) 66-70
- [124] L. Perreux, and A. Loupy, *Tetrahedron*, **57**, (2001) 9199-9223
- [125] N. Thanh, N.D. Giang, L.Q. Vinh, and H.T. Dat, *Communications in Physics*, **24**, (2014) 153-161
- [126] G.P Bareto, G. Morales, and M.L.L Quintanilla, *Journal of Materials*, **2013**, (2013) 478681
- [127] H.C. Lee, W. Liu, S. Chai, A.R. Mohamed, C.H. Voon, U. Hashim, M. K. Arshad, P.Y.P Adelyn, A.R.N. Huda, S.M. Kahar, N.M.S Hidayah, C.W. Lai, and C. Khe, *Procedia Engineering*, **184**, (2017) 460–468
- [128] S. Sathish, and S. Balakumar, *Journal of Luminescence*, **190**, (2017) 272–278
- [129] J. Polte, *Crystal Engineering Communications*, **17**, (2015) 6809-6830
- [130] J. Y. Rempel, M. G. Bawendi, and K. F. Jensen, *Journal of American Chemical Society*, **131**, (2009) 4479–4489

- [131] J. FlorS, A.M. de.LimaM, and R. Davolos, *Surface and Colloid Science*, **128**, (2004) 239-243
- [132] D. Dutta, *Journal Sol-Gel Science and Technology*, **77**, (2016) 48–56
- [133] A. M. Pourrahimi, D. Liu, L. K. H. Pallon, R. L. Andersson, A. Mart´inez Abad, J.M. Lagaron, M. S. Hedenqvist, V. Strom, U. W. Geddea, and R. T. Olsson, *Royal Society of Chemistry Advances*, **4**, (2014) 35568–35577
- [134] O. Singh, N. Kohli, and R.C. Singh, *Sensors and Actuators B*, **178**, (2013) 149-154
- [135] E. Ozel, I.G. Tuncolu, C. Aciksari, and E. Suvuci, *Hittite Journal of Science and Engineering*, **3**, (2016) 73-80
- [136] H. Zhang, D. Yang, Y.J. Yi, X.Y. Ma, J. Xu, and D.L. Que, *Journal of Physical Chemistry B*, **108**, (2004) 3955-3958
- [137] M. Rosina, P. Ferret, P.H. Jouneau, I.C. Robin , F. Levy , G. Feuillet , and M. Lafossas, *Microelectronics Journal*, **40**, (2009) 242–245
- [138] S. Bagheri, K.G. Chandrappa, and S.B.A. Hamid, *Der Pharma Chemica*, **5**, (2013) 265-270
- [139] P. Sagar, P.K. Shishodia, R.M. Mehra, *Applied Surface Science*, **253**, (2007) 5419-5424
- [140] S.S. Alias, A.B. Ismail, and A.A. Mohamad, *Journal of Alloys and Compounds*, **499**, (2010) 231-237
- [141] S. Pung, W. Lee, and A. Aziz, *International Journal of Inorganic Chemistry*, **2012**, (2012) Article ID 608183
- [142] D. Chen, Z. Wang, T. Ren, H. Ding, W. Yao, R. Zong, and Y. Zhu, *Journal of Physical Chemistry C*, **118**, (2014) 15300-15307
- [143] Z.R. Tian, J.A. Voigt, J. Liu, B. Mckenzie, M.J. Mcdermott, M.A. Rodriguez, H. Konishi, H.F. Xu, *Nature Materials*, **2**, (2003) 821-826
- [144] K.N. Abbas, N. Bidin, *Applied Surface Science*, **394**, (2017) 498-508

- [145] F. Liu, Y.H. Leung, A.B. Djuricic, A.M. Ching, and W.K. Chan, *Journal of Physical Chemistry C*, **117**, (2013) 12218–12228
- [146] M.A. Fox, and M.T. Dulay, *Chemistry Reviews*, **93**, (1993) 341-357
- [147] J. FlorS, A.M. de.LimaM, and R. Davolos, *Surface and Colloid Science*, **128**, (2004) 239-243
- [148] H. Cheng, J. Wang, Y. Zhao and X. Han, *RSC Advances*, **4**,(2014) 47031–47038
- [149] G. Wang, L. Xu, J. Zhang, T. Yin and D. Han, *International Journal of Photoenergy*, **2012**, (2012) 265760
- [150] W. Raza, S.M. Faisal, M. Owais, D. Bahnemannc, and M. Muneer, *Royal Society of Chemistry*, **6**, (2016) 78335-78350
- [151] B. Subash, B. Krishnakumar, M. Swaminathan, and M. Shanthi, *Langmuir*, **29**, (2013) 939–949
- [152] M. Samadia, M. Ziraka, A. Naserib, E. Khorashadizadea, and A.Z. Moshfegh, *Thin Solid Films*, **605**, (2016) 2–19
- [153] A. Furubayashi, T. Hitosugi, Y. Yamamoto, K. Inaba, G. Kinoda, Y. Hirose, S. Toshihiro, and H. Tetsuya, *Applied Physics Letters*, **86**, (2005) 252101–252103
- [154] J. Wang, Y. Liang, F. Cheng, C. Fang, H. Chen, C. Tsai, J. Jiang, and T. Nee, *Journal of Luminescence*, **136**, (2013) 11-16
- [155] Y. Qiu, M. Yang, H. Fan, Y. Xu, Y. Shao, X. Yang, and S. Yang, *Materials Letters*, **99**, (2013) 105–107
- [156] E. Debroye, J.V Loon, H. Yuan, K.P. F. Janssen, Z. Lou, S. Kim, T. Majima, and M.B. J. Roeffaers, *Journal of Physical Chemistry Letters*, **8**, (2017) 340–346
- [157]J. Gupta, P. Bhargava, and D. Bahadur, *Physics B*, **448**, (2014) 16–19
- [158] L. Zhang, L. Yin, C. Wang, N. Lun, and Y. Qi, *Applied Material Interfacets*, **2**, (2010) 1769–1773

- [159] G. Lee, S. Kim, S. Jung b, S. Jang, and J. Kim, *Sensors and Actuators B*, **250**, (2017) 569–573
- [160] A. Castellanos-Gomez, *Journal of Physical Chemistry Letters*, **6**, (2015) 4280–4291
- [161] E. Gharibshahia, E. Saion, A. Ashraf, and L. Gharibshahi, *Applied Radiation and Isotopes*, **130**, (2017) 211–217
- [162] M.B. Gawande, A. Goswami, F.X. Felpin, T. Asefa, X. Huang, R. Silva, X. Zou, R. Zboril, and R.S. Varma, *Chemical Reviews*, **116**,(2016) 3722-3811
- [163] C. Barreneche, R. Mondragon, D. Ventura-Espinosa, J. Mata, L.F. Cabeza, A.I. Fernández, and J.E. Julia, **128**, (2018) 121-126
- [164] E. Ruckenstein, G.O. Berim, and G. Narsimhan, *Advances in Colloid and Interface Science*, **215**, (2015) 13–27
- [165] M.C. Weinberg, W.H. Poisl, and L. Granasy, *ComptesRendusChimie*, **5**, (2002) 765-771
- [166] M. Volmer, W.A. Keimbildung, and U.Z. Gebilden, *Physical Chemistry*, **119**, (1926) 277–301
- [167] R. Becker, and W. Doering, *Annals of Physics*, **24**, (1935) 719–752.
- [168] V.K. Lamer, and R.H. Dinegar, *Journal of American Chemical Society*, **72**, (1950) 4847-4854
- [169] Y.N. Xia, Y.J. Xiong, B. Lim, S.E. Skrabalak, *Angewandte Chemie International Edition*, **48**, (2009) 60-103
- [170] J. Lothe, and G. M. Pound, *Journal of Chemical Physics*, **36**, (1962) 2080-2085
- [171] E.C. Vreeland, J. Watt, G.B. Schober, B.G. Hance, M.J. Austin, A.D. Price, B.D. Fellows, T.C. Monson, N.S. Hudak, L. Maldonado-Camargo, A.C. Bohorquez, C. Rinaldi, and D.L. Huber, *Chemistry of Materials*, **27**, (2015) 6059–6066
- [172] T. Sugimoto, *Advanced Colloid Interface Science*, **28**, (1987) 65–108.

- [173] I.M. Lifshitz, V.V. Slyozov, *Journal of Physical Chemistry Solids*, **19**, (1961) 35–50.
- [174] N.T.K. Thanh, N. Maclean, and S. Mahiddine, *Chemical Reviews*, **114**, (2014) 7610–7630
- [175] T. Nishinaga, *Progress in Crystal Growth and Characterization of Materials*, **62**, (2016) 43–57
- [176] Y.N. Xia, Y.J. Xiong, B. Lim, and S.E. Skrabalak, *Angewandte Chemie International Edition*, **48**, (2009) 60-103.
- [178] H.J. You, J.X. Fang, F. Chen, M. Shi, X.P. Song, and B.J. Ding, *Journal of Physical Chemistry C*, **112**, (2008) 16301—16305.
- [179] H.J. You, S.C. Yang, B.J. Ding, and H. Yang, *Chemical Society Reviews*, **42**, (2013) 2880—2904.
- [180] Y. Xia, X. Xia, and H.C. Peng, *Journal of American Chemical Society*, **137**, (2015) 7947—7966.
- [181] H. You, and J. Fang, *Nano Today*, **11**, (2016) 145—167
- [182] K.A. Fichthorn, *Chemical Engineering Science*, **121**, (2015) 10-15
- [183] R.L. Penn, and J.F. Banfield, *Geochim.Cosmochim Acta*, **63**, (1999) 1549—1557.
- [184] F.D. Wang, V.N. Richards, S.P. Shields, and W.E. Buhro, *Chemistry of Materials*, **26**, (2014) 5—21.
- [185] X.G. Peng, L. Manna, W.D. Yang, J. Wickham, E. Scher, A. Kadavanich, and A.P. Alivisatos, *Nature*, **404**, (2000) 59—61.
- [186] Z.A. Peng, and X.G. Peng, *Journal of American Chemical Society*, **123**, (2001) 1389—1395.
- [187] H.M. Zheng, R.K. Smith, Y.W. Jun, C. Kisielowski, U. Dahmen, and A.P. Alivisatos, *Science*, **324**, (2009) 1309—1312.

-
- [188] J.M. Yuk, J. Park, P. Ercius, K. Kim, D.J. Hellebusch, M.F. Crommie, J.Y. Lee, A. Zettl, and A.P. Alivisatos, *Science*, **336**, (2012) 61—64.
- [189] T. Uematsu, M. Baba, Y. Oshima, T. Tsuda, T. Torimoto, and S. Kuwabata, *Journal of American Chemical Society*, **136**, (2014) 13789—13797
- [190] V.K. Lamer and R.H. Dinegar, *Journal of American Chemical Society*, **72**, (1950) 4847—4854
- [191] N.T.K. Thanh, N. Maclean, S. Mahiddine, *Chemical Reviews*, **114**, (2014) 7610—7630
- [192] Y.W. Wang, J.T. He, C.C. Liu, W.H. Chong, and H.Y. Chen, *Angewandte Chemie International Edition*, **54**, (2015) 2022—2051
- [193] Y. Xia, X. Xia, and H.C. Peng, *Journal of American Chemical Society*, **137**, (2015) 7947—796.

CHAPTER 3: The Effects of operational parameters on the photocatalytic degradation of Rhodamine B

3.1 Introduction

Processes that are designed for application at a larger scale require that optimum conditions be evaluated in order to get the most efficient conditions for operation. For example, the optimization of the operating conditions in large scale application of ZnO-based photocatalytic processes is of vital importance. Intrinsic properties of ZnO such as surface area, band gap energy, crystallinity and morphology are controlled during synthesis and can be improved by varying certain reaction parameters (e.g. reaction time, synthesis method, capping agent, type of precursor etc.) [1-4]. These properties form a major part of the internal parameters that influence the photocatalytic activity of ZnO nanoparticles. The extrinsic properties of ZnO such as nanoparticles concentration/loading, dye solution pH, dye concentration and light intensity are also important in photocatalysis. These properties must be individually studied during the use of the nanoparticles at hand to get a better understanding of its photocatalytic degradation efficiency [5]. In the photocatalytic degradation of dyes in aqueous solution, the properties of the ZnO nanoparticles are affected by the conditions under which it is used [6]. It is therefore vital to review some of the effects of operational parameters on the photocatalytic degradation process [7-10].

Khezrianjoo et al., [11] reported on the effect of operational parameters on the degradation of Acid Yellow using ZnO nanoparticles. The study indicated that the rate of degradation was highly dependent on properties such as pH, dye concentration, ZnO nanoparticles loading and ethanol concentration. They reported that Acid Yellow was degraded quickly at pH 8, with the ZnO nanoparticles loading of 1 g/L for a 50 mg/L dye solution. Dyes exist in neutral, basic or acidic form based on the type of charge it possesses on its structure when it is in an aqueous solution [12]. The charge on the dye molecules is important because it determines how the dye molecules interact with the surface of the ZnO nanoparticles at different pH values. For example, the surface charge of ZnO changes depending on the pH conditions that it is exposed to in an

aqueous solution relative to its point of zero charge (pH 8.6) [13]. Below pH of 8.6, its surface is positively charged, and above pH 8.6 it is negatively charged. This therefore means that it will interact differently with the dyes of different charges, with efficient interaction occurring in the case where the dye and the surface of the ZnO are different [14, 15]. Easy interaction between the dye molecules and the surface of the ZnO nanoparticles results to high degradation rate.

ZnO nanoparticles loading used during photocatalytic degradation of methylene blue proved to be an important parameter in a study done by Balcha et al. [16]. They observed that increasing the concentration of the ZnO nanoparticles improved the degradation rate for up to 1 g/L, after which the degradation rate remained constant for up to 1.5 g/L. The observed trend was said to be due to the increased availability of active sites when the ZnO concentration was increased which improved the degradation rate. Above 1.5 g/L, the degradation rate remained constant because the excess amount of the ZnO nanoparticles caused high turbidity in the solution that prevented the light from travelling easily in the solution and hence retarded the rate of degradation.

The concentration at which dyes exists in the environment vary depending on the input from industry. Sakthivel et al. [17] conducted a study where they varied the concentration of Acid Brown 14 from 2×10^{-4} to 6×10^{-4} mol/L and the results revealed that the initial dye concentration influences the rate of degradation of the dye. The results were easy to understand since increasing the dye concentration result in more dye molecules being available and hence there aren't enough hydroxyl radicals to degrade the vast amount of the dye molecules, hence the rate tends to decrease at high concentrations of the dye. In this study, the synthesis of ZnO using microwave heating method is reported. The effect of operational parameters such as dye concentration, ZnO nanoparticles loading, pH of dye solution and the reusability study of the ZnO nanoparticles is studied.

3.2 Synthesis Procedure

3.2.1 Chemicals and materials

Zinc nitrate hexahydrate, $\text{Zn}(\text{NO}_3)_2 \cdot 6\text{H}_2\text{O}$, $\geq 98\%$, and Cetyltrimethylammonium bromide (CTAB) were obtained from Sigma Aldrich. Ammonia, 25 %, was obtained from Associated Chemical Enterprise (ACS). Rhodamine B was obtained from MAY and BAKER LTD. A Universal 320R sonicator (t/min = 10, RPM = 7000) was obtained from Hettich Lab Technology and a Microwave Reaction System, (Multiwave 3000 SOLV) was obtained from Anton Paar. All chemicals were used as received without any further purification.

3.2.2 Synthesis of ZnO nanoparticles

Typically, 1.5324 g of zinc nitrate hexahydrate was dissolved in 37.5 mL CTAB solution (0.1 M) in a 100 mL beaker and stirred for 5 min. Once the zinc nitrate hexahydrate was dissolved, the pH of the solution was adjusted to pH 7 using 25 % of ammonia (NH_3) as modified from [18]. The resulting white aqueous solution was then vigorously stirred with the help of a magnetic stirrer for 20 min. The white aqueous precipitate was transferred into 2 vessels and hydrothermally microwaved at 600 W for 15 min. After completion of the reaction, it was allowed to naturally cool to room temperature and the white powdered samples were collected by centrifugation. The powdered samples were washed thoroughly with deionized water and ethanol to remove impurities possibly remaining in the final products. Finally, the samples were dried at 80°C for 12 h in an oven under air.

3.2.3 Characterization

Prior to characterization, the ZnO nanoparticles were dissolved in ethanol and sonicated for ten min using a Digital ultrasonic cleaner (Model: PS – 20A). The optical properties were determined by Photoluminescence (PL) spectroscopy using a Varian Cary Eclipse EL04103870

fluorescence spectrophotometer and UV-Vis spectroscopy using a Varian Cary Eclipse (Cary 50) UV-Vis absorption spectrophotometer. For visualization of the sizes and morphology of the nanoparticles, Transmission Electron Microscopy (TEM) was used and recorded using a FEI Technai T12 TEM microscope operated at an acceleration voltage of 120 kV. TEM samples were prepared by drop-casting the ethanol diluted samples on a 300 mesh copper grids. Structural properties were analysed by Powder X-ray Diffraction using a Bruker MeasSrv (D2-205530)/D2-205530 diffractometer equipped with a secondary graphite monochromated CoK α radiation (λ 1.79026 nm) at 30 kV/30 mA. Measurements were taken using a glancing angle of incidence detector at an angle of 2°, for 2 θ values between 10-90° in steps of 0.026° with a step time of 37 s and at a temperature of 25 °C. The light source (solar simulator) used for photocatalysis was an ORIEL SOL 2A, Newport, model – 69907 with input power: 190-264 VAC, 50/60 Hz, 202 A (serial number – 1723). The pH was measured using a Starter 3100 pH Bench

3.2.4 Photocatalytic degradation of Rhodamine B

The dye degradation experiments were conducted by preparing 500 mL stock solution of Rhodamine B with the desired concentration (e.g. 20 ppm). 100 mL of the stock solution was poured into a 200 mL cut beaker and mixed with a known mass (i.e. 0.16 g) of the ZnO nanoparticles. The dye-nanoparticles mixture was sonicated for 30 min in the dark in order to ensure that the ZnO nanoparticles were well dispersed in the solution. At the end of sonication, the mixture was subsequently stirred for 60 min using a magnetic stirrer and a stirrer bar in order to allow for equilibration between the dye molecules and the nanoparticles. Before the mixture was exposed to solar radiation, an aliquot (~ 4 mL) was withdrawn and its absorbance measured, and that aliquot was labelled as ‘time zero’, which meant before exposure to light. The progress of degradation was monitored using the following equation (eq. 3.1):

$$\frac{C_t}{C_0} \times 100 \% \quad \text{eq. (3.1)}$$

Where C_t refers to the concentration of the dye after a certain time of irradiation and C_0 refers to the concentration of the dye before irradiation. The light was then switched on and constantly

irradiated on the mixture that was continuously stirred. Aliquots (~ 4 mL) were then subsequently withdrawn and filtered using a syringe filter (0.2 μ L) at 30 min intervals for a period of 5 h, and their absorbance determined. The progress of the degradation was monitored by the change in the absorbance of the excitation peak (553 nm) of Rhodamine B using UV-Vis absorption spectroscopy. The pH of the dye solution was measured using a Starter 3100 pH Bench. The distance between the dye solution and solar simulator was 12 cm. Table 3.1 shows how the operational parameters were varied during the study. The pH of the dye solution was kept at 6.97 and the volume was 100 mL.

Table 3.1: Range in which the operational parameters were during degradation of Rhodamine B.

Parameters varied			
[ZnO] (ppm)	[Rhodamine B] (ppm)	pH	Light Intensity (W)
20	5	2	54
40	10	4	105
60	15	6	210
80	20	7	
100	25	10	
120		12	
140			
160			
180			

3.2.5 Determination of the point of zero charge of ZnO nanoparticles

The point of zero charge (pzc) is defined as the point where the surface charge of the adsorbent material is zero in the aqueous media. This is an important parameter in photocatalytic degradation as it determines the degree of interaction between the dye molecules and the photocatalyst. To fully ascertain the behaviour of ZnO nanoparticles at various pH, its point of zero charge was determined using the pH drift method [19] as follows:

A 0.01 M aqueous solution of NaCl was prepared in a 200 mL volumetric flask. To 15 mL of the solution, nitrogen gas was allowed to bubble in it and pH measured when its value was stable. The pH was then adjusted to pH 2 using HCl/NaOH. The initial pH was noted after which 10 mg of ZnO nanoparticles were added to the 15 mL solution of NaCl. The mixture was kept under stirring for 48 hr at room temperature. The same process was repeated for pH 4, 6, 8, 10 and 12. After 24 hr of stirring, the solution was filtered and the final pH measured for each set [19].

A plot of the final pH(y axis) vs Initial pH (x axis) gave a straight line as shown in Figure 3.1

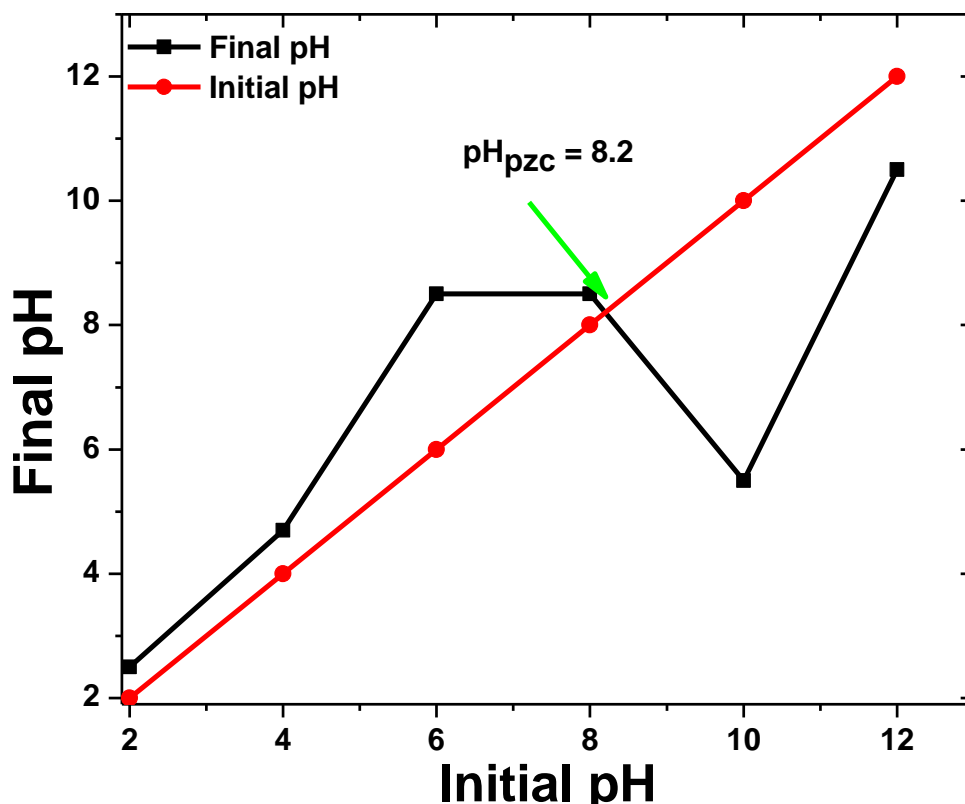


Figure 3.1: Plot for determination of the point of zero charge of as-synthesized ZnO.

3.3 Results and Discussion

3.3.1 Structural properties of ZnO

A typical PXRD diffractogram of ZnO nanoparticles is shown in Figure 3.2. The peaks in the diffraction pattern were indexed perfectly to the hexagonal wurzite ZnO phase reported in the JCPDS (Card No. 01-079-2205) with the lattice constants of $a = 3.2501 \text{ \AA}$ and $c = 5.2071 \text{ \AA}$ and space group $P6_3mc$. The high intensity and narrow width of the peaks in the diffractogram are an indication of the high crystallinity of the synthesized ZnO nanoparticles.

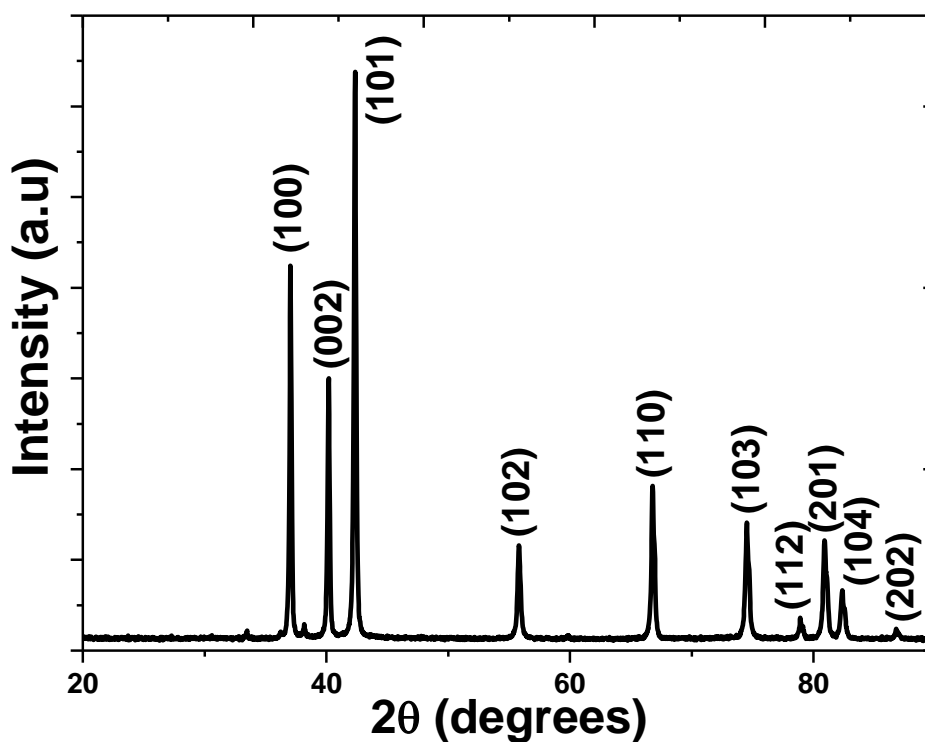


Figure 3.2: PXRD pattern of the ZnO nanoparticles prepared by microwave heating method.

All the peaks correlate perfectly to the reference and any peaks that could possibly be attributed to any impurities were not detected and this served as an indication of the high purity of the synthesized ZnO nanoparticles. The diffractogram displays a characteristic anisotropic growth, with the most intense (101) plane being the preferred growth direction.

Figure 3.3 shows the surface morphology of ZnO nanoparticles synthesized at 600 W microwave powers for a period of 15 min. It is observed that ZnO nanoparticles adopted a rod-like morphology which is characterized by irregular ends.

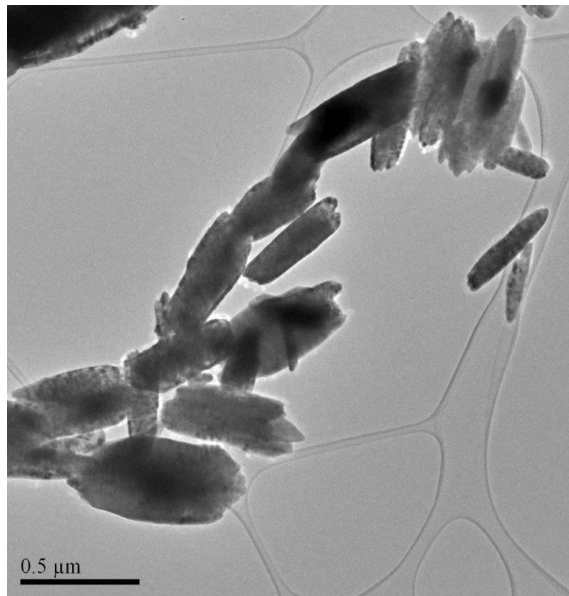
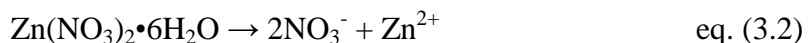


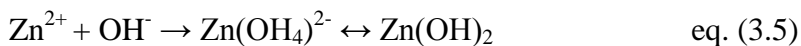
Figure 3.3: TEM micrograph of the ZnO synthesized via microwave assisted heating method.

The rods are composed of varying sizes in which the average length was found to be 608 nm with an average width of 205 nm. The anisotropic growth which was observed in the PXRD diffractogram by the high intensity of the (101) peak is supported by the length to width ratio of the rods which is greater than one ($608/205 = 2.97$). The growth mechanism of the ZnO rods was proposed as follows:

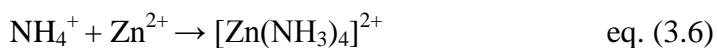
When $\text{Zn}(\text{NO}_3)_2 \cdot 6\text{H}_2\text{O}$ was dissolved in water, it dissociates into its constituent ions (eq. 3.2). The NO_3^- anions were hydrolysed producing OH^- ions (eq. 3.3). Upon addition of the ammonium solution, NH_3 was also hydrolysed to form OH^- and NH_4^+ ions (eq. 3.4).



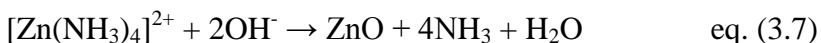
The OH^- and Zn^{2+} ions reacted to form either $\text{Zn}(\text{OH}_4)^{2-}$ or $\text{Zn}(\text{OH})_2$, which were the monomers for ZnO (eq. 3.5).



The NH_4^+ will also react with Zn^{2+} to form a tetraaminezinc ion complex $[\text{Zn}(\text{NH}_3)_4]^{2+}$ (eq. 3.6).



Upon exposure to microwave irradiation, the $\text{Zn}(\text{OH})_2$ and $\text{Zn}(\text{OH}_4)^{2-}$, being the monomers, undergo dehydration as the temperature of the reaction mixture increased resulting to the formation of ZnO nuclei [18]. Similarly, the $[\text{Zn}(\text{NH}_3)_4]^{2+}$ monomers reacted with the OH^- ions in solution (eq. 3.7), which subsequently became converted to ZnO [20, 21].



In hydrothermal synthesis, the specific surface energy of the different crystal facets determines the resulting crystal shape based on how the surfactant molecules interact with the initially formed crystallites. In this study, the formation of the 1D rod-like nanostructures is indicative of the growth that is favoured along the [101] direction of ZnO. Rod-like nanoparticles form due to the adsorption of the monomers to the high energy polar surfaces (i.e. $\pm [0001]$) characteristic of the wurtzite structure of ZnO. Under neutral conditions (pH = 7), ZnO also has non polar surfaces that are negatively charged. To control the growth of ZnO, the CTAB capping agent was used to modify the morphology and size of the nanoparticles [22]. It was proposed that when the CTAB was dissolved in an aqueous medium, it dissociated into CTA^+ and Br^- ions. The CTA^+ cations become attracted to the non polar surfaces of ZnO preventing the precursor monomers from binding in this growth direction and hence hindering lateral growth. The hindrance of growth along the non-polar facets allowed for growth to be fast along the polar facets. (i.e. c-axis) of ZnO forming rod-like nanoparticles. The preferred growth along one particular direction is known as anisotropic growth [23].

3.3.2 Optical properties of ZnO

The UV-Vis absorption spectrum of the as-synthesized ZnO nanoparticles is shown in Figure 3.4(a). The spectrum displays a strong absorption peak at ~ 372 nm (3.33 eV) which was characteristic of pure hexagonal ZnO phase [23-25]. The absorption peak at 372 nm was slightly blue shifted from that of the exciton state in the bulk which occurs at wavelength of ~ 387 nm (3.20 eV) [26-29].

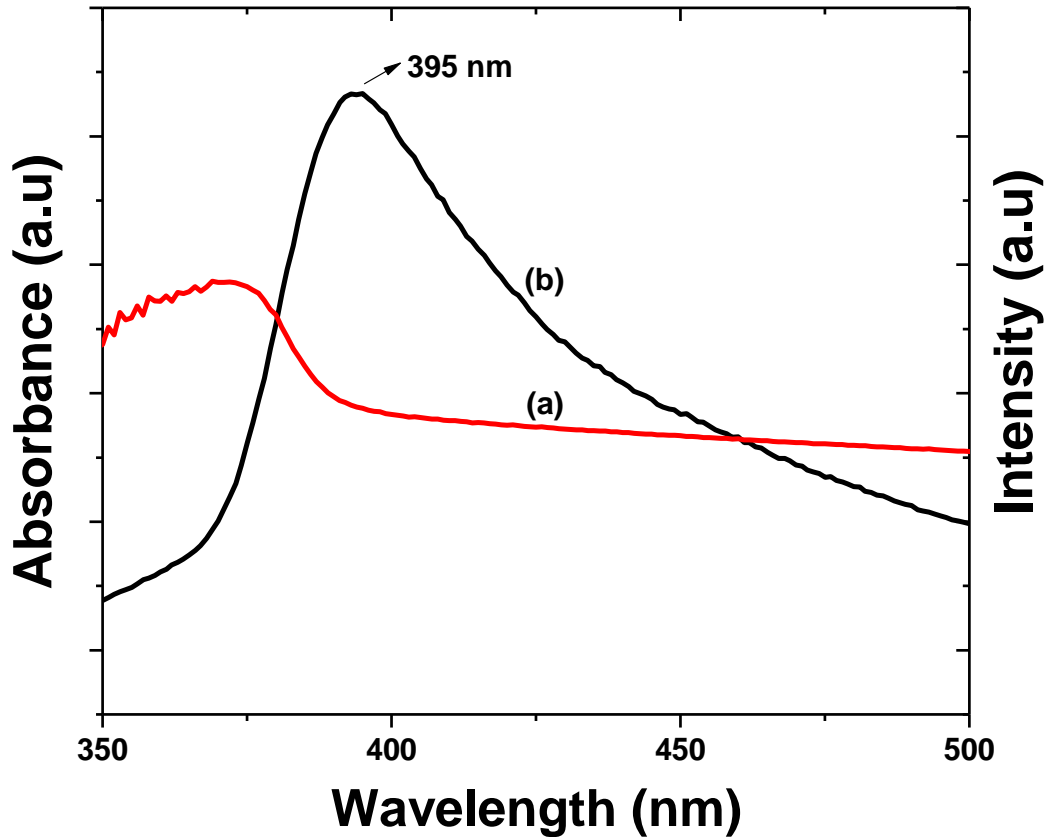


Figure 3.4: The (a) UV-Vis absorption and (b) PL spectra of ZnO nanoparticles synthesized using microwave heating method.

The presence of this absorption peak alone in the spectrum supports the high purity of the synthesized nanoparticles as observed in PXRD results. The absorption band edge of the ZnO was determined using the following equation (eq. 3.8):

$$E = \frac{hc}{\lambda} \quad \text{eq. (3.8)}$$

Where;

E = band gap energy (eV), h = Planck's constant ($m^2 \text{ kg/s}$), c = speed of light (m/s) and λ = wavelength (nm) corresponding to the absorption edge [30]. The calculated band gap energy based on eq. 3.8 was found to be 3.14eV. The tailing of the UV-Vis spectrum is indicative of the poly dispersed nature of the ZnO nanoparticles as observed in TEM (Figure 3.1(a)).

Figure 3.3(b) shows the corresponding room temperature PL spectrum of the ZnO nanoparticles synthesized via microwave heating method. The PL spectra of the nanoparticles display a strong UV emission peak centered at 395 nm. The UV emission peak has been attributed to the near band edge characteristic of ZnO. The occurrence of the broad PL peak that is not Gaussian (i.e. symmetrical) is attributed to the poly dispersity of the nanoparticles as seen in TEM [31].

3.4 Photocatalytic degradation study

3.4.1 Preliminary studies

To test for the photocatalytic activity of the ZnO nanoparticles, the dye degradation experiments were conducted in order to determine the operational parameters to be used during the course of the research. The ZnO photocatalyst loading used was 160 ppm, with the dye concentration of 20 ppm. Figure 3.5(a) and Figure 3.5(b) shows typical spectral changes in the UV-Vis absorption peak and the physical colour change, respectively, that was observed during the course of the degradation of Rhodamine B. It can be observed that as the dye solution was exposed to light, the concentration of the dye started to decrease which was indicated by the decrease in the absorbance of the dye absorption peak located at 553 nm (Figure 3.4(a)).

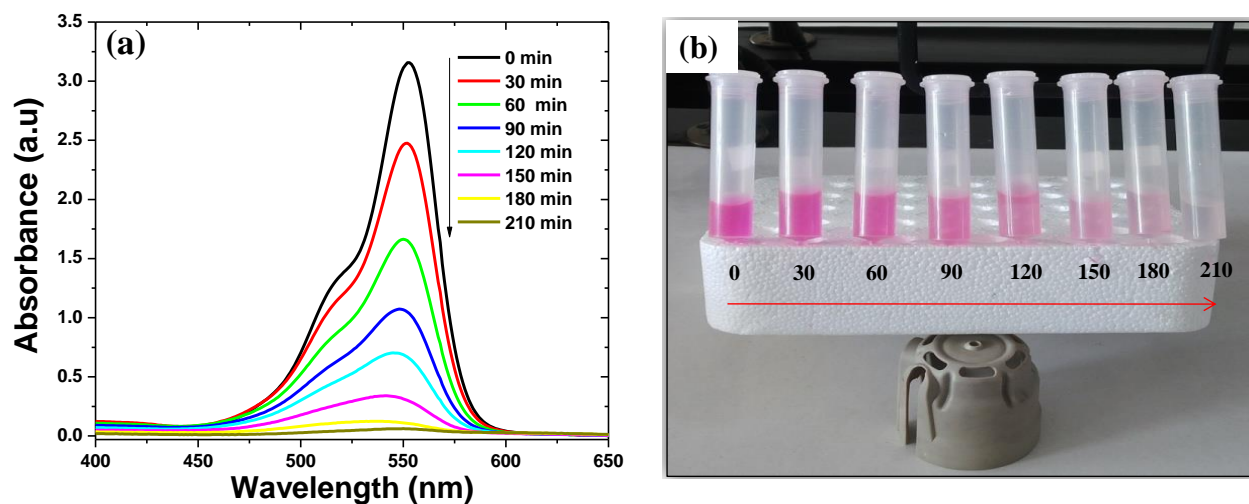


Figure 3.5: UV-Vis spectra changes of (a) Rhodamine B as a function of light irradiation and (b) physical colour change monitored for 210 min.

The decrease in absorbance together with the colour change indicated that the synthesized ZnO nanoparticles were photo active and could be used for photocatalytic degradation studies. The degradation process seemed to be free of any UV-Visible active intermediates. This conclusion is based on the idea that throughout the degradation process, the only absorption peak that was observed was the one that was attributed to Rhodamine B. One would expect that since this

degradation process is based on oxidation, the functional groups which are most susceptible to oxidation would be degraded first and the intermediates generated through time would be picked up in the absorption spectra. It was observed that the absorption peak of the dye when it became colourless (210 min) was in the same region as the blank which was run using deionized water. The zero absorption of what used to be the dye, together with the drastic change in colour from pink to completely colourless can be used as supportive evidence that the dye completely degraded [32]. Figure 3.6 depicts the percentage of the dye which was degraded at 30 min intervals. In the first 90 min of dye degradation, the dye was being degraded at a fast rate with approximately 67 % degradation achieved in the first 90 min. The degradation efficiency slowed down after 90 min, with the 33 % remaining requiring 120 min to completely degrade.

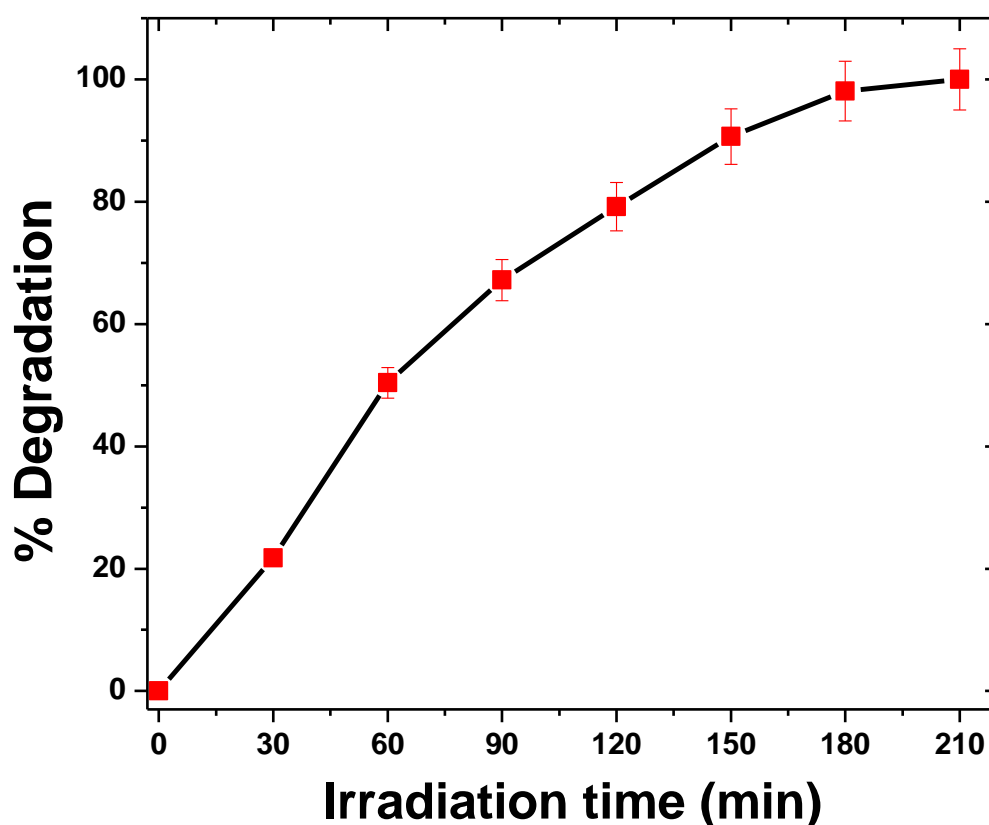


Figure 3.6: The percentage of Rhodamine B dye degraded in 30 min intervals.

It is well understood that the dye has to diffuse from the bulk solution into the surface of the ZnO nanoparticles in order to be degraded [33, 34]. Hence, we concluded that when the dye concentration was high, a large proportion of the dye molecules were in close proximity to the

active sites and thus were able to quickly reach the ZnO surface and be oxidized, hence a large proportion of the dye is degraded in the early stages of the degradation process [35]. As the dye concentration decreased through time of exposure to light, the dye molecules took a significant amount of time to reach the surface of the ZnO nanoparticles, even with less competition for active site, this result in decreased degradation efficiency with time. Another factor that can be considered in attempting to give a plausible explanation for the retardation of the degradation efficiency is the behaviour of ZnO when it is exposed to light in aqueous solution [36]. Photocorrosion of ZnO has been extensively studied and it is known to be one of the major drawbacks of ZnO in photocatalysis [37, 38]. This process involves the chemical reaction of the photogenerated electrons with certain atoms which make up the crystal lattice of ZnO (eq. 3.9 and 3.10) [39, 40]



The photodecomposition of ZnO into its constituent ions causes a decrease in the amount of the photo active material present in the solution with time and hence explains the decrease in the degradation efficiency after a certain amount of irradiation.

3.4.2 Effect of ZnO nanoparticles loading

To determine the effect of the concentration of ZnO nanoparticles on the degradation efficiency, a variety of photocatalytic degradation experiments were conducted to determine the amount of ZnO that is capable of degrading Rhodamine B at a fast rate. This study was done by varying the concentration of ZnO used in each case while keeping parameters such as the concentration of Rhodamine B, light power, aliquot withdrawal interval and pH constant. Aliquots were withdrawn at 30 min interval. The concentration of the Rhodamine B dye used was 20 ppm at pH 6.95 (natural water) and ZnO concentration in the range 60–200 ppm and light power of 180 W. Figure 3.7 displays control\blank experiment which was conducted by exposing the dye solution to light without the addition of the ZnO nanoparticles. This was done in order to determine the effect of light only on the concentration of Rhodamine B. This was done due to the fact that some dyes can be degraded by exposure to light only through a process known as photolysis [41-43].

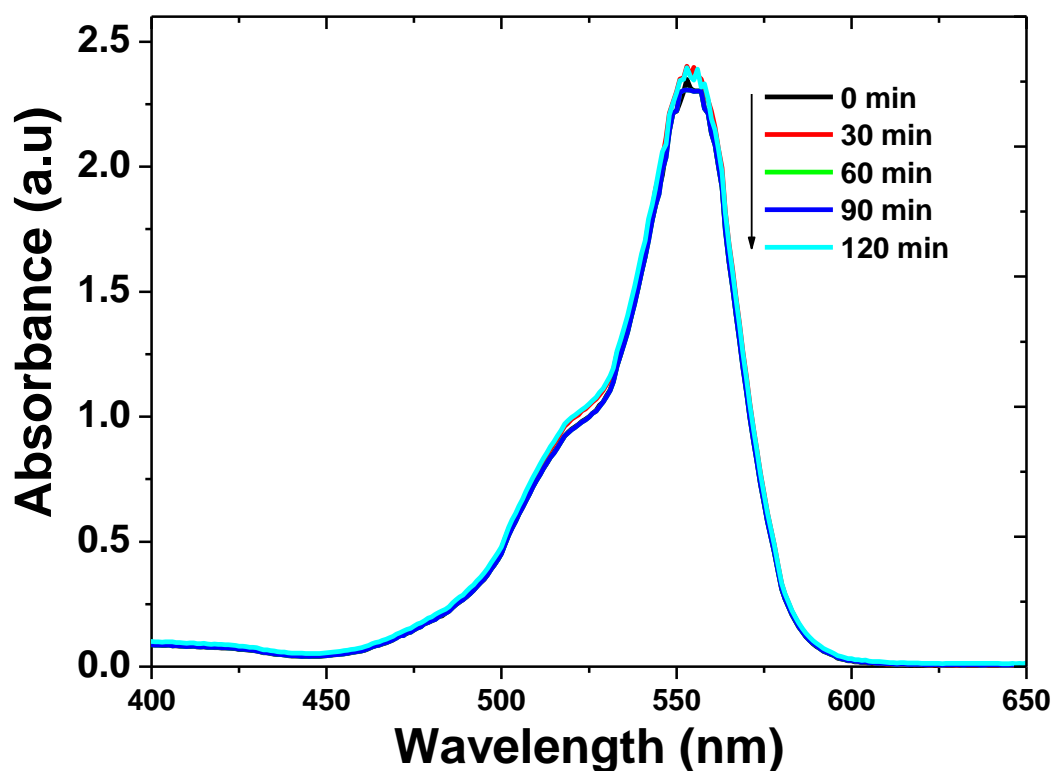


Figure 3.7: UV-Vis absorption spectra changes of Rhodamine B under UV irradiation in the absence of ZnO nanoparticles.

The spectrum of the Rhodamine B dye remained fairly constant throughout the irradiation time and there was negligible change in the absorbance of the spectrum. This indicated that the concentration of the dye was not affected by UV-light only and hence no photocatalytic degradation was occurring during the experiment. Results from experiments which were conducted during the course of the ZnO nanoparticles loading study indicated that light in conjunction with the ZnO nanoparticles were required in order to achieve dye degradation. In the results displayed in Figure 3.8, an increase in degradation efficiency with increasing ZnO nanoparticles dose was observed for up to 160 ppm ZnO concentration, after which a steady decrease in degradation efficiency occurred.

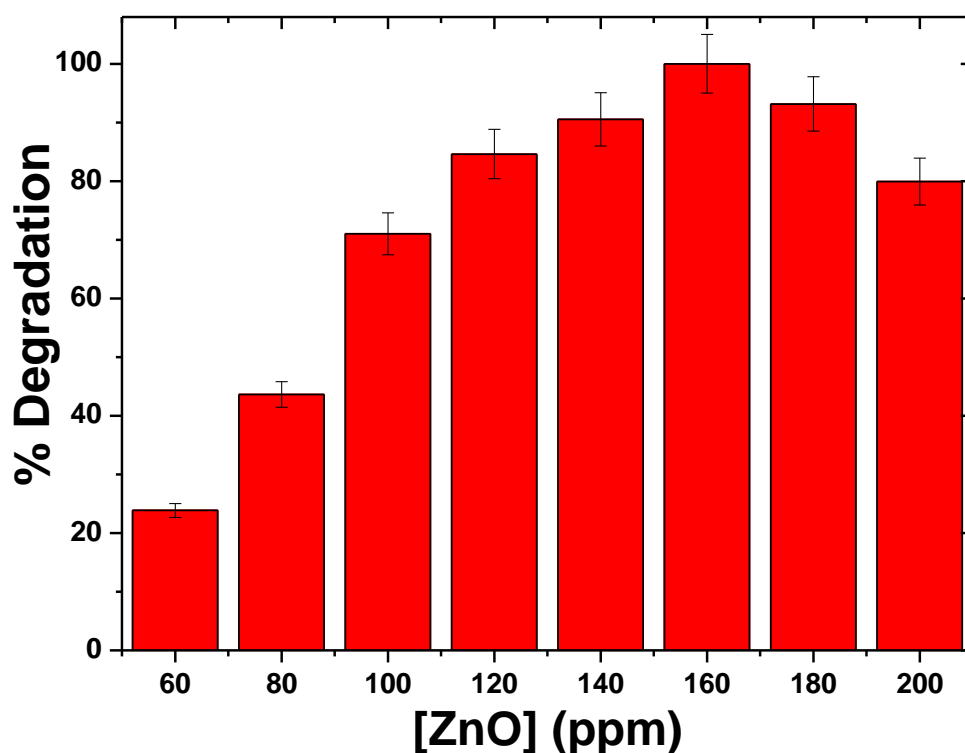


Figure 3.8: Percentage degradation of Rhodamine B as a function of ZnO concentration done over a period of 5 h.

The increase in the degradation efficiency can be explained in terms of the number of active sites available for degradation on the ZnO nanoparticles surface [44, 45]. An increase in the concentration of the ZnO nanoparticles meant more active sites were available to allow for rapid generation of hydroxyl radicals and hence the dye could be degraded quickly [46]. The opposite is true for low concentrations of ZnO nanoparticles, where the limited number of active sites

become a limiting factor resulting to decreased degradation efficiency. The decrease in the degradation efficiency above 160 ppm can be attributed to the fact that as the concentration of the ZnO nanoparticles in the dye solution increased, the turbidity and scattering effect of the solution also increased and hence light could not easily travel through the solution to activate the ZnO nanoparticles [47, 48]. This decrease may also be due to the increase in the amount of particle – particle interaction (aggregation) in the solution which means a limited number of oxidizing species are readily available for the degradation of the dye molecules [49, 50]. This trend was also reported by N. Daneshvar et al. [51] in their study of the degradation of acid red (AR14) where the maximum degradation was observed at 160 ppm ZnO concentration [51].

The kinetic study of the photocatalytic degradation of Rhodamine B using green synthesized ZnO was investigated with the Langmuir–Hinshelwood kinetic model, which also covers the adsorption properties of the substrate on the photocatalyst surface [52]. The equation is represented as follows:

$$Rate = \frac{dC}{dt} = k \frac{KC}{1+KC} \quad \text{eq. 3.10}$$

Where C is the concentration of Rhodamine B at the irradiation time, k the reaction rate constant, and K is the degradation coefficient of the reactant. Where k' is the apparent rate constant. A plot of $\ln(C_0/C)$ versus time results in a straight line; its slope is the pseudo first- order degradation rate constant (K_{app}) [52, 53]. The experimental data obtained in the kinetic study of Rhodamine B degradation at different ZnO photocatalyst concentrations were fitted with the Langmuir–Hinshelwood kinetic model. The results obtained are illustrated in Figure 3.9.

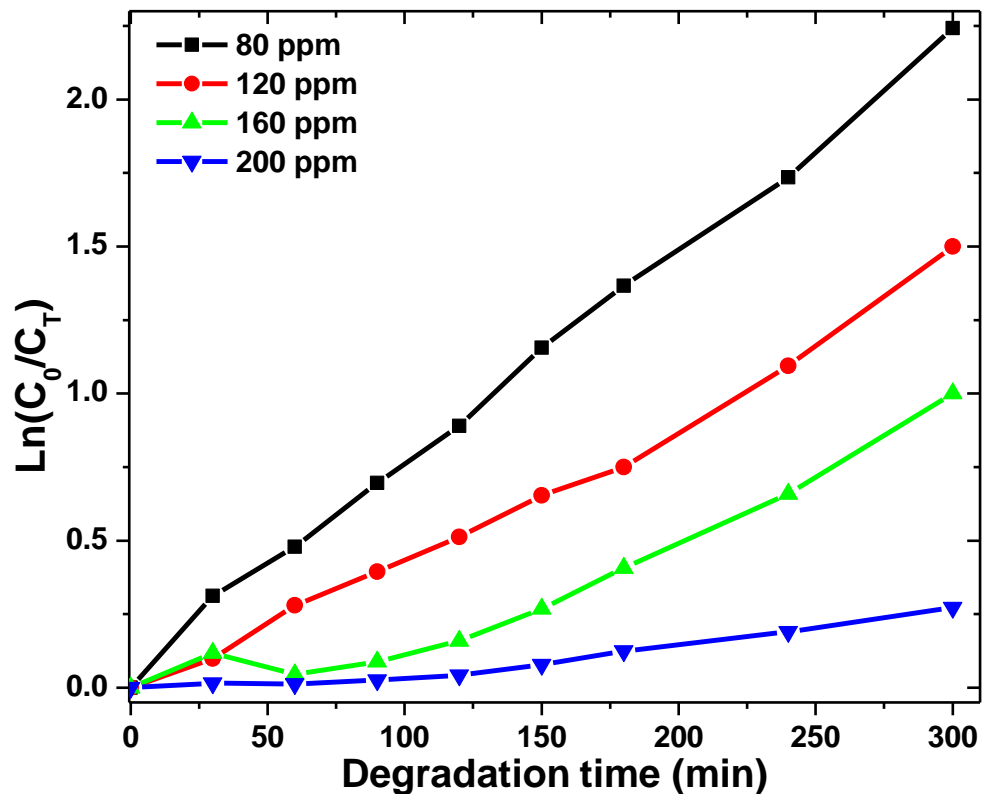


Figure 3.9: Kinetic study of the degradation of Rhodamine B (20 ppm) at different ZnO photocatalyst loading (80 – 200 ppm).

Table 3.2: Rate constants for photocatalytic degradation of Rhodamine B

No	Initial concentration	ZnO concentration	K_{app}	R^2
1	20	80	0.007	0.997
2	20	120	0.004	0.989
3	20	160	0.003	0.899
4	20	200	0.0001	0.928

The plots of the concentration data give a straight line, showing that the photocatalytic degradation of Rhodamine B can be described by the pseudo-first-order kinetic model [54]. The correlation coefficient constant for the fitted line and the rate constants are graphically obtained and their values for 4 selected concentrations are represented in table 3.2. A decrease in the rate constant was observed when the concentration of the Rhodamine B dye. This decrease in the rate constant was supportive evidence that the presence of a large amount of dye molecules results to slower rates of degradation.

3.4.3 Effect of dye concentration

To study the effect of the initial concentration of the Rhodamine B has on the rate of its degradation; a study was conducted by varying the initial concentration in the range 5–25 ppm while factors such as catalyst loading (50.5 ppm), pH 6.97 and light intensity (180 W) were kept constant. Figure 3.10 shows the percentage degradation against irradiation time plot obtained during the dye concentration study.

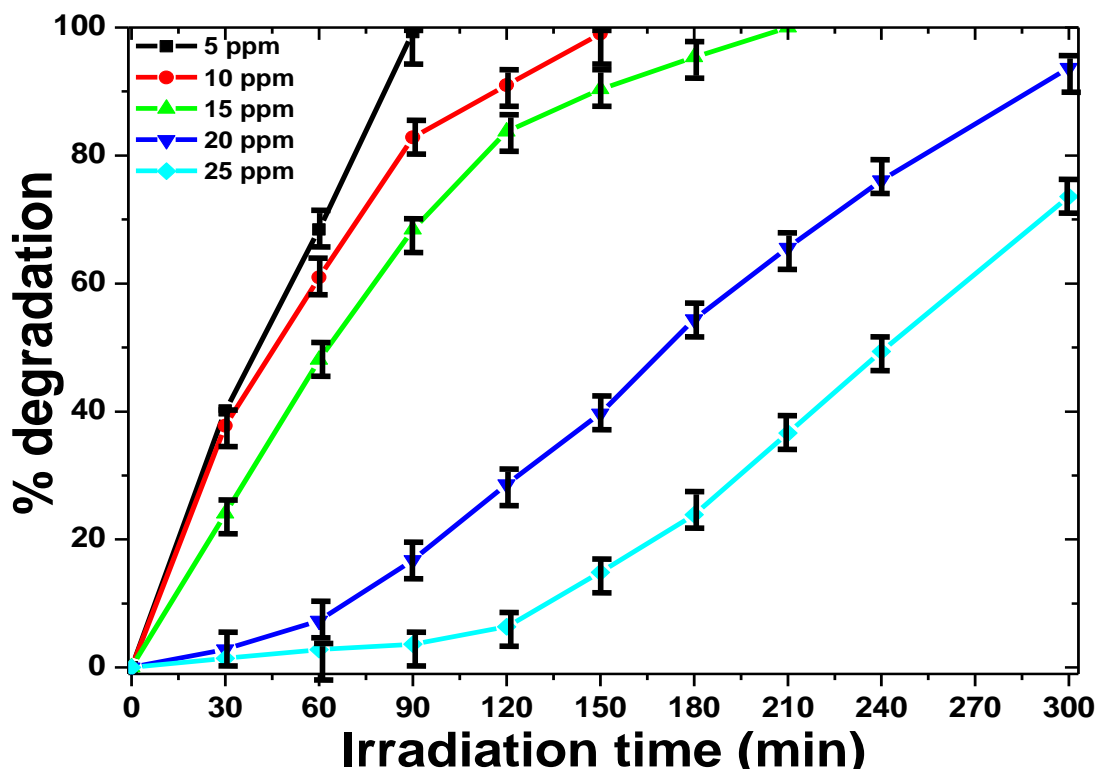


Figure 3.10: Effect of initial concentration of Rhodamine B on degradation efficiency

The decrease in the degradation efficiency as the dye concentration was increased is apparent. This observation was due to the fact when the concentration of the dye was low, it became easy for the dye molecules to reach the active sites on the surface of ZnO nanoparticles, and this interaction occurred easily when the dye concentration was low due to less competition for the active sites [55, 56]. As the concentration of the dye was increased, there was more competition for the active sites, and this increased the time that was required for all the dye molecules to come into contact with the surface of the ZnO nanoparticles [57, 58]. Complete degradation (100 %) was observed for 5, 10 and 15 ppm dye concentration in less than 210 min, when the

concentration was increased to 20 ppm, the degradation efficiency decreased to 93 % and a further decrease (73 %) was observed for 25 ppm dye concentration. An increased opacity of the dye solution at very high dye concentration retards light from efficiently interacting with the ZnO nanoparticles and this also contributes to the reduced degradation efficiency of the nanoparticles [59]. The kinetics of the degradation of Rhodamine B with an initial concentration of 20 ppm under optimized experimental conditions is shown in Figure 3.11.

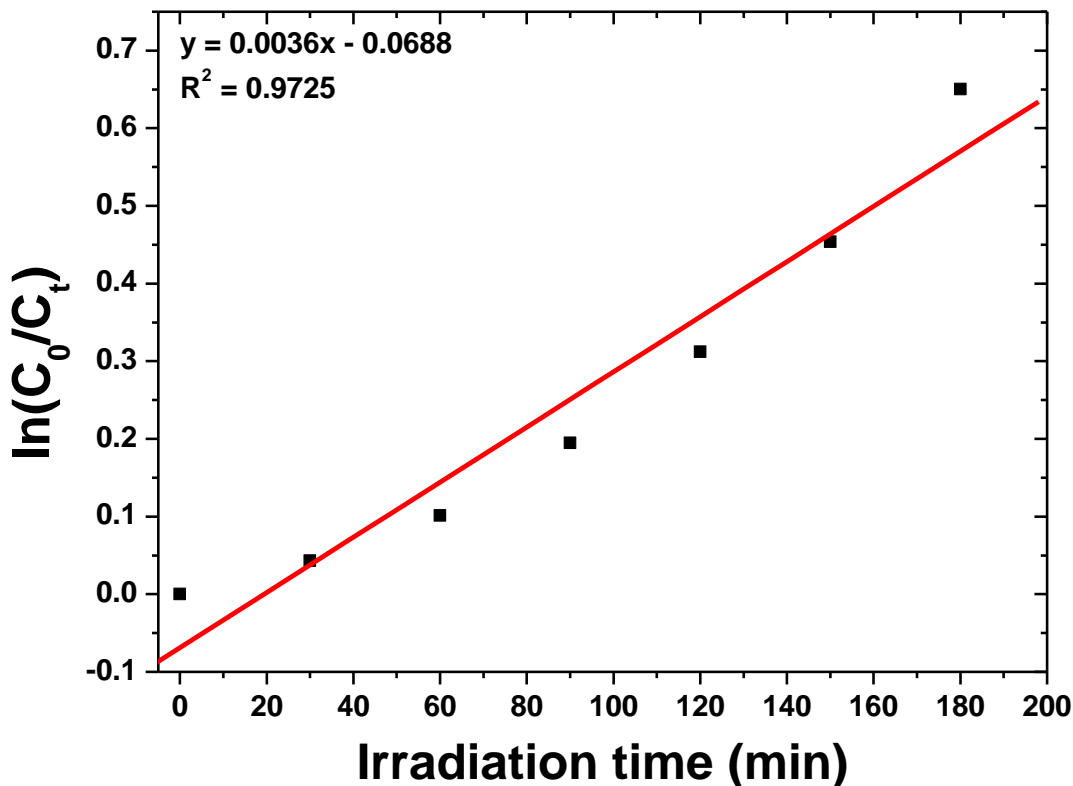


Figure 3.11: Plot of $\ln(C_0/C_t)$ against irradiation time obtained during the photocatalytic degradation of Rhodamine B.

The plot of $\ln(C_0/C_t)$ versus time gave a semi-logarithmic straight line. The straight line indicated that the photocatalytic degradation of Rhodamine B followed a pseudo first order kinetic model with a correlation constant of $R^2 = 0.9725$. The rate constant was determined using (eq. 3.11).

$$\ln(C_0/C_t) = kt \quad \text{eq. (3.11)}$$

Where C_0 represents the initial dye concentration, C_t represents the dye concentration after a certain amount of time of exposure to UV radiation, k is the reaction rate constant and t is the

time in which the reaction was run [60]. The calculated rate constant was found to be $k = 1.4 \times 10^{-5} \text{ s}^{-1}$. The rate constant, k , gives a direct measure of the relative reaction rate [61]. A very small value for the rate constant equates to a very slow reaction in general. Equally, a large value for the rate constant means a large value for the rate and that the reaction is rapid [61]. In this study, it can be noted that the obtained value of the rate constant is relatively small, indicating a low rate of degradation of the dye.

3.4.4 Effect of pH

Textile industrial waste water exists in the environment at different pH and hence it is important to conduct a study which will determine the effect of the pH of waste water has on the rate of degradation of dyes. To do this, a study was conducted at pH values in the range 2–12. Figure 3.12 shows the results obtained when the photocatalytic degradation of Rhodamine B was conducted at different pH values of the dye/ZnO mixture.

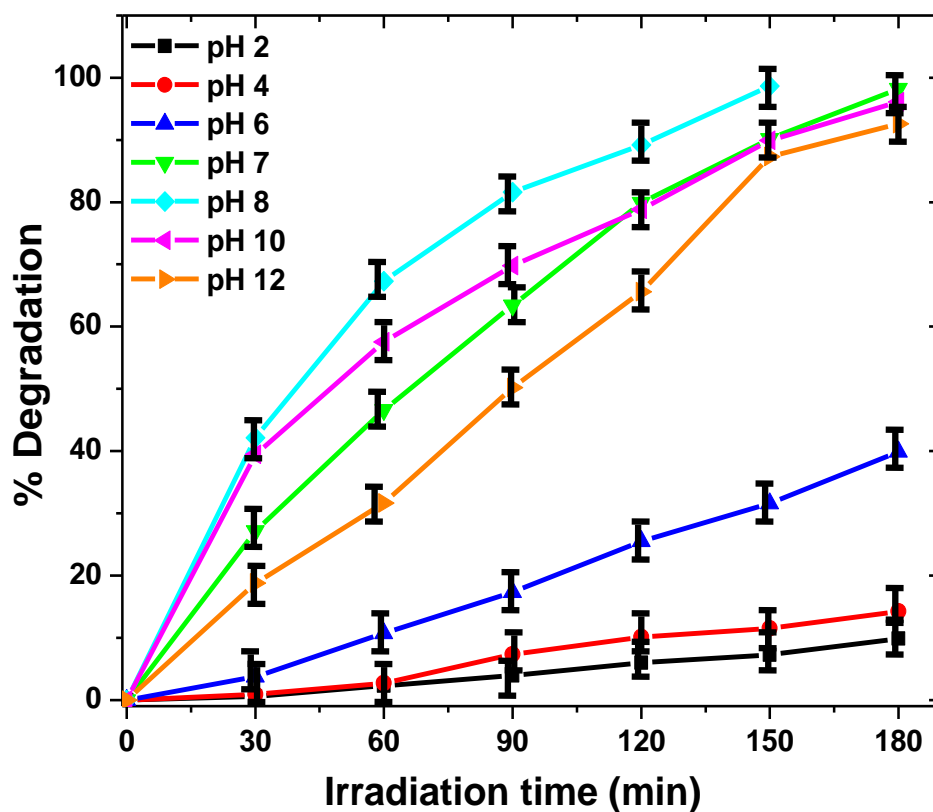


Figure 3.12: A graph showing the effect of pH on the photocatalytic degradation efficiency of ZnO nanoparticles.

It can be seen that ZnO nanoparticles are capable of degrading Rhodamine B in the entire pH range under which the study was conducted, but the extent of degradation differs significantly as the solution pH changes from acidic to neutral and finally to basic conditions. During the study, it was determined that ZnO nanoparticles were more efficient at degrading the dye under neutral and basic conditions and a significant decrease in the degradation efficiency was observed under acidic conditions. For instant, after 30 min of degradation at pH 2, 2 % of the dye was degraded

with the overall degradation reaching 10 % after 180 min. At neutral pH 7, 28 % of the dye was degraded after 30 min after which 100 % degradation was observed after 180 min. Under basic conditions such as pH 12, 18 % degradation was observed after 30 min, with only 93 % degradation observed after 180 min.

The decrease in the efficiency under acidic conditions can be explained based on the effect of pH on the surface charge properties of the ZnO and the dye. At lower pH values, the molecules of the dye become protonated and the surface of the ZnO nanoparticles also become positively charged [62]. The positive charges on the surface will thus repel the dye molecules and thus prevent the required interaction between the dye and ZnO nanoparticles. This will therefore cause a decrease in the amount of dye molecules which reach the active ZnO nanoparticles active sites and cause a decrease in the rate of degradation [63]. Also, this decrease can be explained in terms of the solubility of ZnO at different pH values. Under acidic condition, ZnO reacts directly with hydrogen ions and hence undergoes a phase change through a process which is known as chemical dissolution as shown below (eq. 3.12) [64].



When this process takes place, the metal oxide required for the photogeneration of electrons and holes exist in small quantities in solution, and hence reduced degradation was observed because not enough hydroxyl radicals were being produced. At pH 4, 14 % degradation was observed and a further decrease to 9 % degradation occurred when the pH was dropped to 2, this observation gives an idea of the extent of the repulsion force and chemical dissolution at very acidic conditions. As the pH of the solution was increased to pH 8, maximum degradation was observed as indicated by the 100 % degradation efficiency at this pH. This increase in degradation efficiency can be also be explained by focusing on the surface properties of the ZnO at different pH values. The point of zero charge (pzc) of ZnO is ± 8.6 [65], which means that the surface of ZnO is positively charged at pH values which are less than 8.6, and negatively charged at pH values greater than pH 8.6 [66]. It can then be concluded that at pH values which are close to the point of zero charge, the ZnO nanoparticles surface were not sufficiently charged to such an extent that it could repel dye molecules; this resulted in efficient dye-ZnO interactions at pH 8 which resulted in fast degradation as compared to other pH values.

A slight decrease in the degradation efficiency was observed at very basic conditions, starting from pH 8 up to pH 12. This trend observed was attributed to the fact that at higher pH values there is a high concentration of hydroxyl ions which are occupying the ZnO nanoparticles surface and they repel the negatively charged dye molecule resulting to a slight decrease in degradation when the pH is raised further away from pH 8 [67]. It is important to note that the decrease in degradation efficiency was not as high as in acidic conditions. This observation can be explained in terms of the dominant hydroxyl radical species in the oxidation process. At higher pH there is a high concentration of hydroxyl ions which are adsorbed onto the surface of the ZnO nanoparticles and it is these hydroxyl ions which are required for hydroxyl radical generation which is the principal oxidizing species in photocatalytic degradation [68]. Hence, this increased hydroxyl ion concentration overcomes the setback which results from the repulsion force that exists between the ZnO nanoparticles and dye molecules. This increase in the generation of hydroxyl radicals also provides an explanation as to why dye degradation is higher at basic condition than in acidic conditions. This study has shed light into the ideal pH range in which ZnO can be used to obtain maximum (100 %) degradation efficiency.

3.4.5 Effect of light intensity

The effect of light intensity (Figure 3.13) on the degradation efficiency of Rhodamine B was done by varying the light intensity (54, 105 and 210 W) irradiated on the dye solution while keeping all other parameters (dye concentration, pH, ZnO nanoparticles loading) constant.

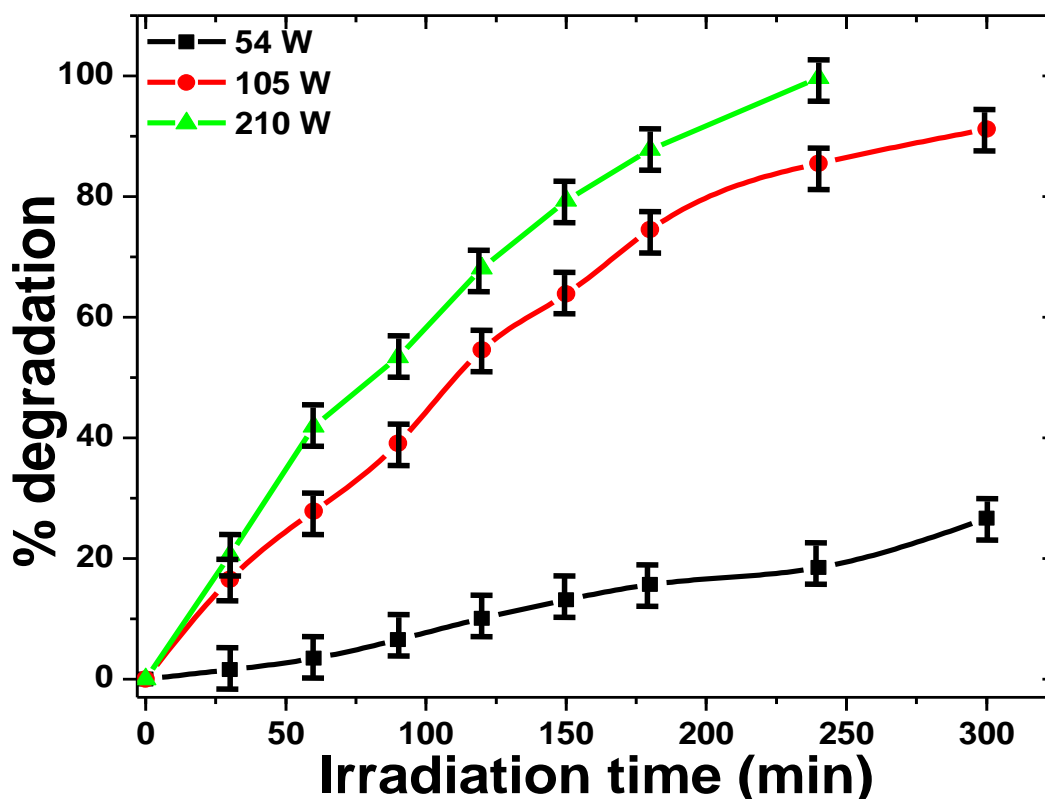


Figure 3.13: A study showing the % degradation of Rhodamine B at different light intensities.

The difference in the degradation efficiency as the intensity of the light source was varied is very significant. When the intensity was set at 210 W, 100 % degradation was achieved. A decrease in degradation was observed as the light intensity was decreased to 105 W and 54 W, with the degradation efficiency dropping to 91 % and 27 %, respectively. This high degradation efficiency at high intensity can be explained in terms of the number of photons with high enough energy to allow for the generation of electrons and holes in the ZnO nanoparticles [69]. Limited number of electrons and holes are generated at low intensity and this therefore results to a

reduced amount of hydroxyl radicals that are produced in the solution which lowers the rate of degradation [70].

3.4.6 Reusability of ZnO

The ability to recycle and reuse a catalyst in any industrial process is of importance from an economical point of view. It therefore became vital to determine if the ZnO nanoparticles can be regenerated with efficient activity. To do this, the first catalytic degradation experiment (1st cycle) was conducted with freshly synthesized ZnO nanoparticles. After the 1st cycle was complete, the ZnO nanoparticles was recovered from the dye solution by centrifugation, after which it was washed thoroughly with deionized water until the pink colour it acquired from the dye was completely removed. The recovered ZnO nanoparticles were further washed with ethanol several times and dried in an oven at 80 °C for 12 h. The same recovering, washing and drying procedure was followed for the experiments conducted using the reused ZnO nanoparticles labelled 2nd, 3rd and 4th cycles. Figure 3.14 shows a bar graph depicting the percentage degradation efficiency that was achieved by the fresh and reused ZnO nanoparticles for up to four cycles.

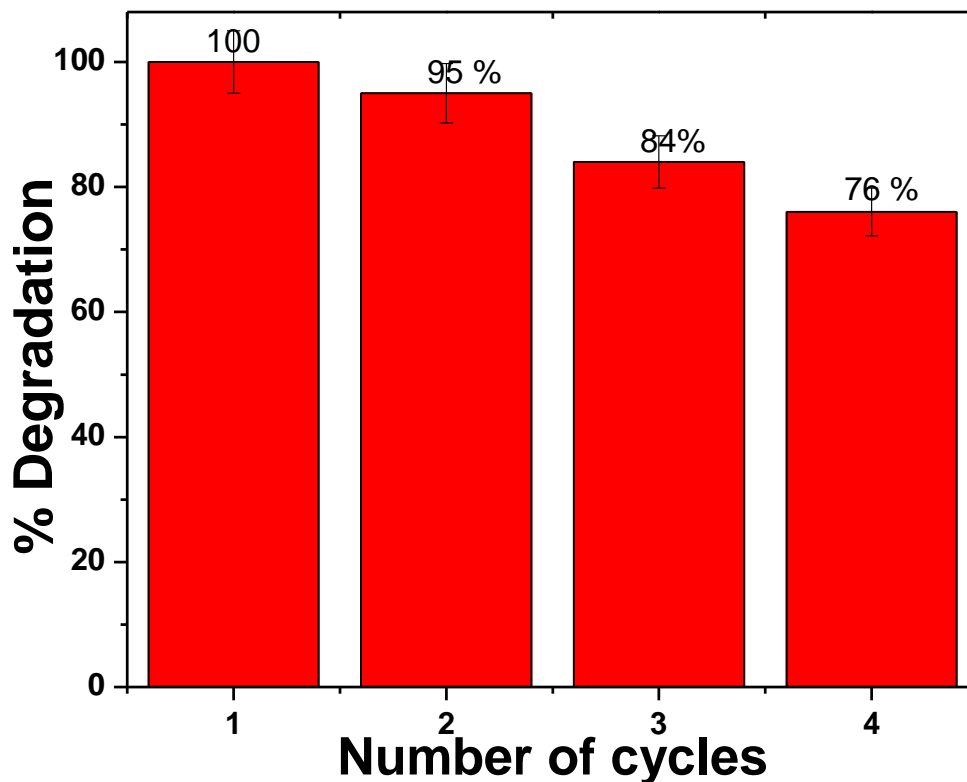


Figure 3.14: Reusability study of the ZnO nanoparticles for up to 4 cycles.

The degradation efficiency of the freshly prepared ZnO nanoparticles reached 100 % degradation after 5 h after which the degradation efficiency decreased to 95 %, 84 % and 76 % for the 2nd, 3rd and 4th cycles, respectively. The decrease in the amount of dye that was degraded after 5 h after multiple cycles indicated that the ZnO nanoparticles was no longer as efficient as it was when it was firstly used. One important factor which was noted was that when the degradation process was run for more than 5 h, the photocatalytic degradation was able to get to 100 % degradation for the 2nd, 3rd and 4th cycles. This decreased degradation efficiency of the recycled ZnO nanoparticles was attributed to a process known as catalyst poisoning [71, 72]. This occurs when certain unwanted materials which are products of the degradation of the dye bind strongly on the ZnO nanoparticles surface and hence affect the accessibility of the active sites resulting to reduced degradation efficiency [73, 74]. The unused ZnO displays prominent irregular ends (Figure 3.15), these irregular ends seems to become smothered as the ZnO nanoparticles were being reused. The proposed hypothesis for this change in morphology is the dissolution of the ZnO nanoparticles in aqueous solution [75]. Another plausible explanation to the decreased

activity of the nanoparticles was due to the increased agglomeration with multiple uses as shown Figure 3.15.

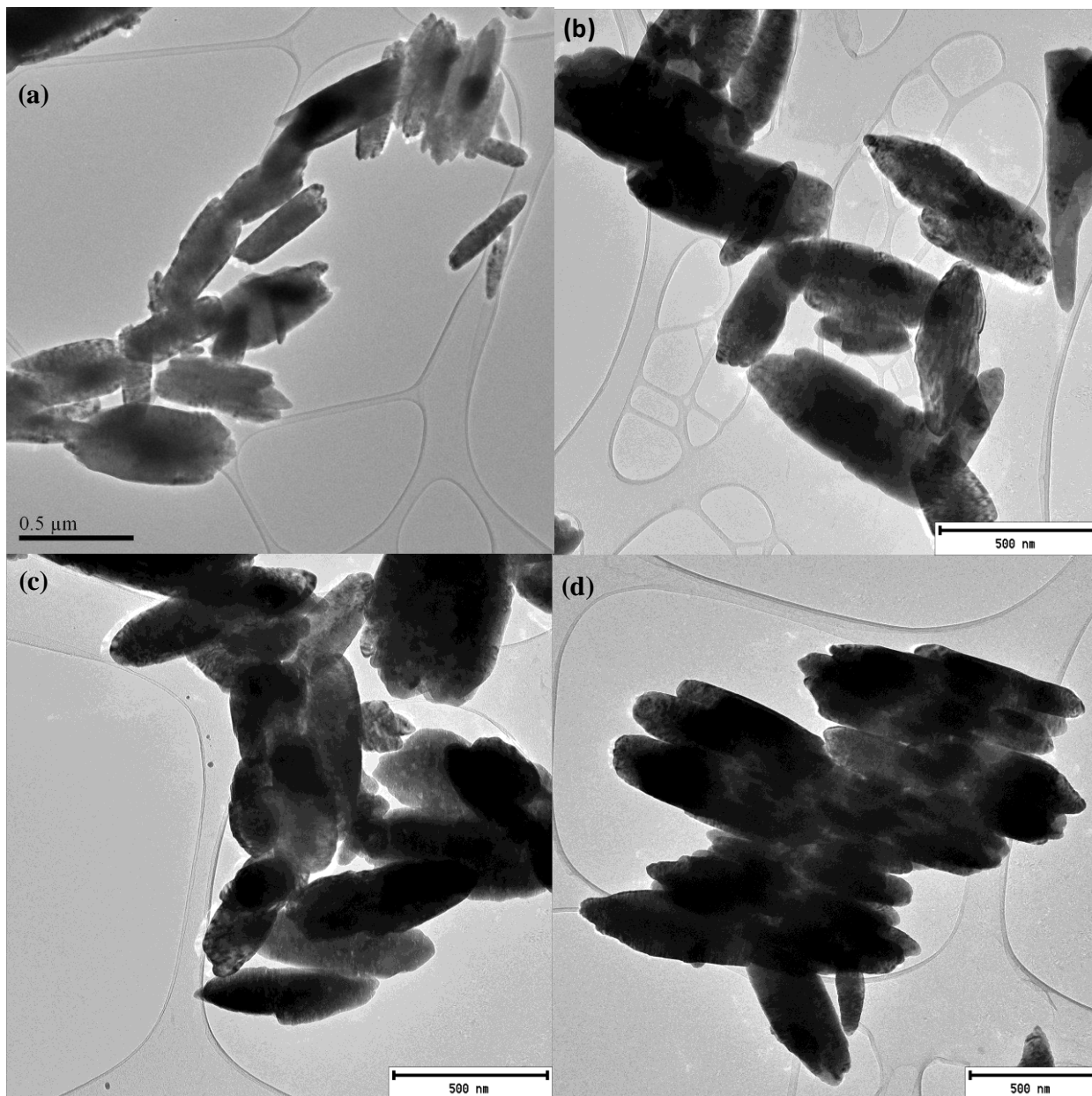


Figure 3.15: The morphological changes of ZnO nanoparticles after (a) 1st, (b) 2nd, (c) 3rd, and (d) 4th cycles of reusing the nanoparticles.

The difference in the degree of agglomeration between the ZnO after use for the different cycles is apparent. The coalescence might be because of particle-particle interaction of molecules during photocatalysis, which then allow the ZnO nanoparticles to agglomerate. The increased

agglomeration results to a reduced surface area of the reused ZnO as opposed to the one which was used in the 1st cycle [76]. Even though the activity of the recycled ZnO nanoparticles decreased, it did not influence the electronic properties of the ZnO nanoparticles as depicted in Figure 3.16.

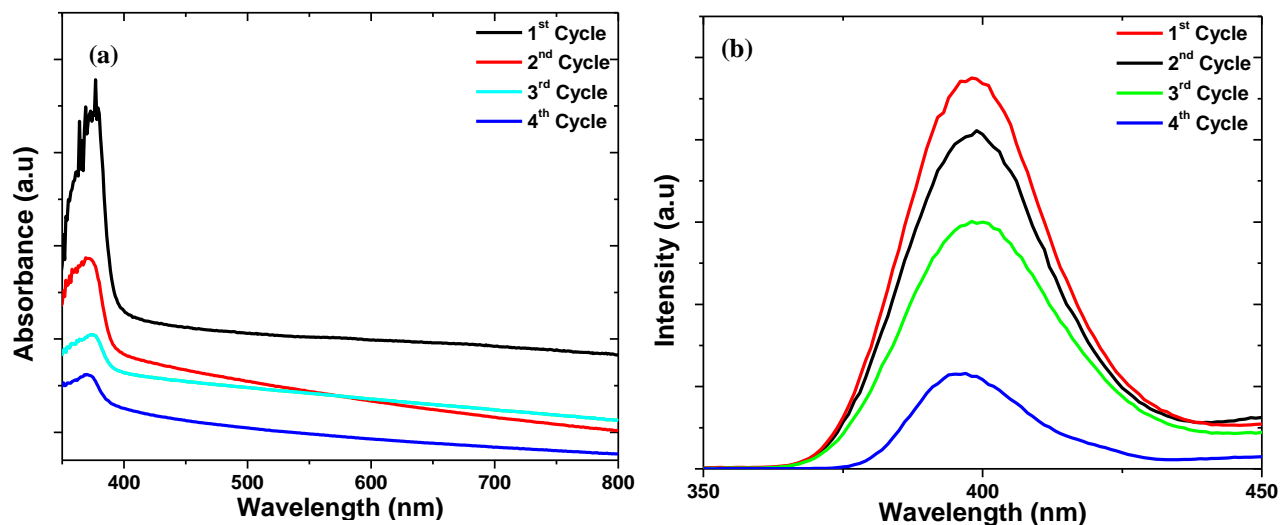


Figure 3.16: The (a) UV-Vis absorption and (b) PL spectra of the ZnO nanoparticles used for up to 4 cycles.

The PL and UV-Vis spectra of ZnO nanoparticles used in different cycles remained fairly unchanged which indicated that the structure of the ZnO nanoparticles was not compromised during the degradation of Rhodamine B. This is in line with the idea that the decreased catalytic activity was caused by the reduced proportion of catalytic active sites resulting from agglomeration and deactivation of some active sites by dye residues.

3.5 Conclusions

Microwave heating method was utilized in the synthesis of rod-like shaped ZnO nanoparticles as authenticated by PXRD, PL, UV-Vis and TEM analysis. The photocatalytic degradation experiments demonstrated that the as-synthesized ZnO was photocatalytically active and could be used to degrade Rhodamine B dye in the presence of sunlight. A variety of operational parameters (ZnO nanoparticles loading, dye concentration, pH and light intensity) were found to have a significant influence on the rate of degradation of Rhodamine B. An increased amount of the ZnO nanoparticles increased the rate of degradation until optimum point, after which it started to decrease. Increasing the concentration of the dye and lowering the intensity of the light source resulted in decreased degradation efficiency. The ZnO nanoparticles were more efficient in degrading the dye in neutral and basic conditions, with a significant decrease in efficiency observed in the acidic region. The optimum conditions for the degradation of Rhodamine B were achieved when the dye solution had a pH of 8, concentration of the ZnO = 160 ppm and light intensity of 210 W. The degradation of Rhodamine B was found to have a first order rate constant of $k = 1.4 \times 10^{-5} \text{ s}^{-1}$.

3.6 References

- [1] J. Rodrigues-Paez, A.C. Caballero, M. Villegas, C. Moure, P. Duran, and J.F. Fernandez, *Journal of European Ceramic Society*, **21**, (2001) 925–930
- [2] S. Kaluza, M.K. Schröter, R. Naumann d'Alnoncourt, T. Reinecke, and M. Muhler, *Advanced Functional Material*, **18**, (2008) 3670–3677
- [3] Z. Hu, D.J.E. Ramí' rez, B.E.H. Cervera, G. Oskam, and P.C. Searson, *Journal of Physical Chemistry B*, **109**, (2005) 11209-11214
- [4] J.N. Hasnidawani, H.N. Azlina, H. Norita¹, N.N. Bonnia, S. and Ratim, and E.S. Ali, *Procedia Chemistry*, **19**, (2016) 211–216
- [5] E.T. Soares, M.A. Lansarin, and C.C. Moro, *Brazilian Journal of Chemical Engineering*, **24**, (2007) 29-36
- [6] N. Daneshvar, M.A Behnajady, M.K.A.Mohammadi, and M.S.S. Dorraji, *Desalination*, **230**, (2008) 16-26
- [7] X. Zhou, Z.X. Xie, Z.Y. Jiang, Q. Kuang, S.H. Zhang, T. Xu, R. B. Huang, and L.S. Zheng, *Chemical Communications*, **44**, (2005) 5572–5574
- [8] R.A. Mohammad, S.J. Henley, N.G. Emerson, and S.R.P. Silva, *Nanoscale*, **6**, (2014) 235-247
- [9] G. Bandekar, N.S. Rajurkar, I.S. Mulla, U.P. Mulik, D.P. Amalnerkar, and P.V. Adhyapak, *Applied Nanoscience*, **4**, (2014) 199–208
- [10] C.A.K. Gouvea, F. Wypych, S.G. Moraes, N. Duran, N. Nagata, and P.P. Zamora, *Chemosphere*, **40**, (2000) 433–440
- [11] S.K. Hosakere, and D. Revanasiddappa, *Hindawi Publishing Corporation Journal of Catalysts*, **2013**, (2013) 582058
- [12] A. Baffoun, A.E. Ghali, and I. Hachani, *AUTEX Research Journal*, **17**, (2017) 85-95

- [13] F.M. Omar, H.A. Aziz, and S. Stoll, *Journal of Colloid Science and Biotechnology*, **3**,(2014) 1-10
- [14] K. Iraj, and A. Sadollahkhani, *Journal of Materials Science Materials in Electronics*, **27**, (2016) 256-301
- [15] H. Benhebal, M. Chaib, T. Salmon, J. Geens, A. Leonard, S.D. Lambert, M. Crine, and B. Heinrichs, *Alexandria Engineering Journal*, **52**, (2013) 517–523
- [16] A. Balcha, O.P. Yadav, and T. Dey, *Environmental Science and Pollution Research International*, **23**, (2016) 25485-25493
- [17] S. Sakthivel, B. Neppolian, M.V. Shankar, B. Arabindoo, M. Palanichamy, and V. Murugesan, *Solar Energy Materials & Solar Cells*, **77**, (2003) 65–82
- [18] C. Tseng, Y. Chou, C. Lui, Y. Liu, M. Ger and Y. Shu, *Materials Research Bulletin*, **47**, (2012) 96-100
- [19] A.M. Cardenas-Pena, J.G. Ibanez, R. Vasquez-Medrano, *International Journal of Electrochemical Science*, **7**, (2012) 6142-6153
- [20] J. Zhang, L Sun, J. Yin, H. Su, C. Lao, and C. Yan, *Chemistry Materials*, **14**, (2002) 4172-4177
- [21] W. Wu, W. Kung, and J. Ting, *Journal of the American Ceramic Society*, **94**, (2011) 699-703
- [22] H. Zhang, D. Yang, Y. Ji, X. Ma, J. Xu, and D. Que, *The Journal of Physical Chemistry B*, **108**, (2004) 3955-3958
- [23] T.K. Kundu, N. Karak, P. Barik , and S. Saha, *Materials*, **3**, (2010) 2643-2667
- [24] M. Willander, O. Nur, J.R. Sadaf, M.I. Qadir, S. Zaman, A. Zainelabdin, N. Bano and I. Hussain, *Materials*, **3**, (2010) 2643-2667
- [25] P. Kumbhakar, D. Singh, C.S. Tiwary, and A.K. Mitra, *Chalcogenide letters*, **5**, (2008) 387-39

- [26] A.K. Zak, R. Razali, W.H. Majid, and M. Darroudi, *International Journal of Nanomedicine*, **6**, (2011) 1399–1403
- [27] H. Kumar, and R. Rani, *International Letters of Chemistry, Physics and Astronomy*, **14**, (2013) 26-36
- [28] L. Qin, C. Shing, S. Sawyer, and P.S. Dutta, *Optical Materials*, **33**, (2011) 359–362
- [29] E.G. Goh, X. Xu and P.G. McCormick, *ScriptaMaterialia*, **78–79**, (2014) 49–52
- [30] S. Benramache, O. Belahssen, and H.B. Temam, *Journal of Semiconductors*, **35**, (2014)7
- [31] L.K. Jangir, Y. Kumari, A. Kumar, M. Kumar, and K. Awasthi, *Material Chemistry Frontiers*, **1**, (2017) 1413-1421
- [32] S. Pung, W. Lee, and A. Aziz, *International Journal of Inorganic Chemistry*, **2012**, (2012) 608183
- [33] Q. Rahmana, M. Ahmad, S.K. Misra, and M. Lohani, *Materials Letters*, **91**, (2013) 170–174
- [34] A. Gupta, J.R. Saurav, and S. Bhattacharya, *RSC Advances*, **5**, (2015) 71472–71481
- [35] H. Benhebal, M. Chaib, T. Salmon, J. Geens, A. Leonard, S.D. Lambert, M. Crine, and B. Heinrichs, *Alexandria Engineering Journal*, **52**, (2015) 517–523
- [36] R.T. Sapkal, S.S. Shinde, T.R. Waghmode, S.P. Govindwar, K.Y. Rajpure, and C.H. Bhosale, *Journal of Photochemistry and Photobiology B: Biology*, **110**, (2012) 15–21
- [37] Y.Q. Cao, J. Chen, H. Zhou, L. Zhu, X. Li, Z.Y. Cao, D. Wu, and A.D. Li, *Nanotechnology*, **26**, (2015) ISSUE NO024002
- [38] S.M Muthana, A.F. Al-kaim, L.M. Ahmed, and F.H. Hussein, *International Journal of Chemical Science*, **9**, (2011) 969-979
- [39] C. Han, M. Yang, B. Wenga, and Y. Xu, *The Journal of Physical Chemistry*, **16**, (2014) 16891-16903

- [40] L. Zhang, H. Cheng, R. Zong, and Y. Zhu, *Journal of Physical Chemistry C*, **113**, (2009) 2368–2374
- [41] A. Böhnhardt, R. Kühne, R.U. Ebert, and G. Schüürmann, *Journal of Physical Chemistry A*, **112**, (2008) 11391-11399
- [42] J. Oró, and G. Holzer, *Journal of Molecular Evolution*, **14**, (1979) 153–160
- [43] U. Schulze-Hennings, L. Pötschke, C. Wietor, S. Bringmann, N. Braun, D. Hayashi, V. Linnemann, and J. Pinnekamp, *Water Science and Technology*, **74**, (2016) 888-895
- [44] A. Mirzaei, Z. Chen, F. Haghghat, and L. Yerushalmi, *Sustainable Cities and Society*, **27**, (2016) 407–418
- [45] A.B. Patil, K.R. Patil, and S.K. Pardeshi, *Journal of Hazardous Materials*, **183**, (2010) 315–323
- [46] S. Benjamin, D. Vaya, P.B. Punjabi, and S.C. Ameta, *Arabian Journal of Chemistry*, **4**, (2011) 205–209
- [47] G. Meenakshi, A. Sivasamy, *Ecotoxicology and Environmental Safety*, **135**, (2017) 243–251
- [48] T.N. Ravishankar, K. Manjunatha, T. Ramakrishnappa, G. Nagarajua, D. Kumar, S. Sarakar, B.S. Anandakumar, G.T. Chandrappa, V. Reddy, and J. Dupont, *Materials Science in Semiconductor Processing*, **26**, (2014)7–17
- [49] S. Sakthivel, B. Neppolian, M.V. Shankar, B. Arabindoo, M. Palanichamy, and V. Murugesan, *Solar Energy Materials & Solar Cells*, **77**, (2003) 65–82
- [50] J. Esmaili-Hafshejania, and A. Nezamzadeh-Ejhieh, *Journal of Hazardous Materials*, **316**, (2016) 194–203
- [51] N. Daneshvar, D. Salari, and A.R. Khataee, *Journal of Photochemistry and Photobiology A: Chemistry*, **162**, (2004) 317–322
- [52] C.S. Turchi, and D.F. Ollis, *Journal of Catalysis*, **122**, (1990) ISSUE NO178
- [53] N. Barka, and Y. Ait-Ichou, *Arabian Journal of Chemistry*, **3**, (2010) 279-283

- [54] M.V. Shankar, B. Nappolian, S. Sakthivel, B. Arabindo, M, Palanichamy, and V. Murugesan, *Indian Journal of Engineering and Materials Sciences*, **8**, (2001) 104-109
- [55] C. Vidya, M.N.C. Prabha, and M.A.L.A. Raj, *Environmental Nanotechnology, Monitoring & Management*, **6**, (2016) 134–138
- [56] S. Chawla, H. Uppal, M. Yadav, N. Bahadur, and N. Singh, *Ecotoxicology and Environmental Safety*, **135**, (2017)68–74
- [57] S. Ramachandran, A. Sivasamy, and B.D. Kumar, *Ecotoxicology and Environmental Safety*, **134**, (2016)445–454
- [58] S. Singh, and S.L. Lo, *Chemical Engineering Journal*,**309**, (2017) 753–765
- [59] L.V. Barbosaa, L. Marc, E.J. Nassara, P.S. Calefia, M.A. Vicente, R. Trujillano, V. Rives, A. Gil, S.A. Korili, K.J. Ciuffi, E.H. de Faria, *Catalysis Today*, **246**, (2015) 133–142
- [60] T. Yetim and T. Tekin, *PeriodicaPolytechnica Chemical Engineering*, **61**, (2017) 102-108
- [61] C. Beyer, C. Chen, J. Gronewold, O. Kolditz, and S. Bauer, *Ground Water*, **45**, (2007) 774-785
- [62] C. Chakrabarti, and B.K. Dutta, *Journal of Hazardous Materials*, **B112**, (2004) 269-278
- [63] M. Saquiba, M.A. Tariqa, M. Faisala, and M. Muneer, *Desalination*, **219**, (2008) 301–311
- [64] A.A. Khodja, T. Sehili, J.F. Pihichowski, P. Boule, *Journal of Photochemistry and Photobiology A*, **141**, (2001)231
- [65] J. Fernandez, J. Kiwi, C. Lizama, J. Freer, J. Baeza, H.D. Mansilla, *Journal of Photochemistry and Photobiology A*, **151**, (2002) 213-221
- [66] S.A. Hosseini, and S. Babae, *Journal of Brazilian Chemical Society*, **28**, (2017) 299-307
- [67] S. Khezrianjoo, and H.D. Revanasiddappa, *Hindawi Publishing Corporation Journal of Catalysts*, **2013**, (2013) ISSUE NO 582058

- [68] M.S.T. Goncalves, A.M.F. Oliveira-Campos, E.M.M.S. Pinto, P.M.S. Plasencia, and M.J.R.P. Queiroz, *Chemosphere*, **39**, (1999) 781-808
- [69] L. Yang, and Z. Liu, *Energy Conversion and Management*, **48**, (2007) 882-889
- [70] C.S. Uyguner, and M. Bekbolet, *International Journal of Photoenergy*, **6**, (2004) 73-80
- [71] K.S. Ranjitha, and R. T.R. Kumar, *RSC Advances*, **7**, (2017) 4983-4992
- [72] J. Liqiang, X. Baifu, Y. Fulong, W. Baiqi, S. Keying, C. Weimin, and F. Honggang, *Applied Catalysis A*, **275**, (2004) 49–54
- [73] L. Li, M. Krissanasaeranee, S. W. Pattinson, M. Stefik, U. Wiesner, U. Steiner and D. Eder, *Chemical Communication*, **46**, (2010) 7620–7622
- [74] F. Huang, L. Chen, H. Wang, and Z. Yan, *Chemical Engineering Journal*, **162**, (2010) 250–256
- [75] Q. Zhou, J.Z. Wen, P. Zhao, and W.A. Anderson, *Nanomaterials*, **7**, (2017) 9-22
- [76] Y.L. Yuming, W.L. Liu, D. Wang, and W. Zhang, *Environmental Science and Pollution Research*, **21**, (2014) 5177–5186

Chapter 4: Microwave synthesis of various morphologies of ZnO and their photocatalytic activity.

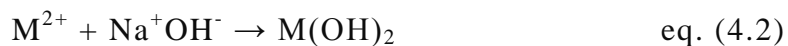
4.1 Introduction

Over the past few decades, there has been an ongoing focus in nanotechnology on the tailoring of hierarchal ZnO nanostructures such as nanobelts, nanoflowers, nanoribbons and nanorods [1-4]. Recently, the nanomaterials community has focused more on investigating the possibility of improving the optical and structural performance of different ZnO nanostructures through manipulation of chemical reaction pathways. The pathways followed by a reaction during growth control the resulting surface morphology and size of the nanocrystals [5-7]. Surface morphology is of interest, particularly in applications such as photocatalytic degradation of dyes, because the degradation mechanism is based on the interaction between the dye molecules and the surface of the ZnO nanoparticles [8-10]. The growth of ZnO nanoparticles can be manipulated by varying reaction conditions such as the concentration of the precursor, type of precursor, synthesis method, reaction temperature, and pH value of the precursor solution [11-14]. The pH value of the precursor solution is one parameter that has been manipulated previously in colloidal synthesis and resulted in various morphological forms of ZnO [15-19]. The question therefore arise as to how does the pH affect the nature in which nanocrystals grow. To answer this question, consider the sol-gel synthesis method, which is used to synthesize ZnO by using zinc metal salts (e.g. $\text{Zn}(\text{CH}_3\text{COO})_2 \cdot 2\text{H}_2\text{O}$, $\text{Zn}(\text{NO}_3)_2 \cdot 6\text{H}_2\text{O}$). Typically, a metal salt is dissolved in water according to the following reaction:

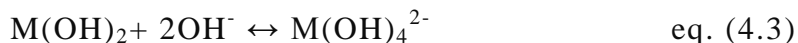


Where M is a transition metal (e.g. Zn, Ti, Co), L is a counter anion (e.g. Cl^- , NO_3^- , CH_3COO^-) and x is the stoichiometry of the hydrate. Once the metal salt has been

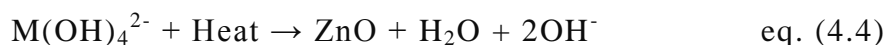
dissolved, a base such as NaOH is added to the solution and results in hydrolysis as follows:



As more OH^- ions are introduced to the solution by addition of NaOH (i.e. increased pH value), the following equilibrium reaction takes place:



It is the $M(OH)_2$ and $M(OH)_4^{2-}$ that undergo condensation when exposed to heat to form ZnO.



The reactions above show that the amount of OH^- ions present in solution determines the concentration of the $M(OH)_2$ and $M(OH)_4^{2-}$ monomers [20-22]. This means that by varying the pH of the metal-salt aqueous solution, one can alter the amount of OH^- ions that will in turn determine the growth mechanism. Different monomer concentrations have been reported to result in different morphologies. For example, at lower concentration, morphologies such as dots and rice grains dominate. As the monomers concentration is increased, rods and heavily branched structures become dominant. This variation in morphology indicates that at high monomer concentration, anisotropic growth is favoured and isotropic growth is preferred only at low monomer concentration [23-26]. The change in morphology with pH has been previously reported for colloidal synthesis, but the trend remains unclear for microwave synthesis. Colloidal synthesis has been used with great success over the years, but long reaction times associated with this method have been a challenge. Hence, in the quest to finding a synthesis method that does reactions quicker while producing uniform particle sizes, microwave has emerged as an effective method to use. Microwave assisted heating is based on heating of materials by dielectric heating effects. When a material with a permanent dipole moment is exposed to an oscillating microwave field, the dipoles in the material will align with the field [27]. This alignment causes rotation that results in friction

and ultimately in heat energy. In this way, the materials are heated homogeneously, which has proven to be advantageous since it produce monodispersed nanocrystals in a very short time [27, 28]. This study reports on the synthesis of ZnO nanoparticles of various morphologies by microwave assisted heating method using zinc acetate dihydrate, cetyltrimethylammonium bromide and sodium hydroxide. The influence of the pH (base concentration) on the morphology, optical, structural properties and photocatalytic activity of the ZnO is reported.

4.2 Synthesis Procedure

4.2.1 Chemicals and materials

Zinc acetate dihydrate, $\text{Zn}(\text{CH}_3\text{COO})_2 \cdot 2\text{H}_2\text{O}$, $\geq 98\%$, and cetyltrimethylammonium bromide (CTAB) were obtained from Sigma Aldrich. Sodium hydroxide (NaOH), $\geq 98\%$, was obtained at Glassworld and Rhodamine B was obtained at MAY and BAKER LTD. A Universal 320R sonicator (t/min = 10, RPM = 7000) was obtained from Hettich Lab Technology and a Microwave Reaction System, (Multiwave 3000 SOLV) was obtained from Anton Paar. All chemicals were used as received without any further purification.

4.2.2 Synthesis of ZnO nanoparticles at different pH values

Typically, 1.5324 g of zinc acetate dihydrate was dissolved in 37.5 mL of CTAB solution (0.1 M) in a 100 mL beaker and stirred for 5 min. Once the zinc acetate dihydrate was dissolved, the pH of the solution was adjusted to the desired pH (i.e. pH 7, 10 and 14) using 0.2 M sodium hydroxide (NaOH). The resulting white aqueous solution was then vigorously stirred with the help of a magnetic stirrer for 20 min. The white aqueous precipitate was transferred into 2 vessels and hydrothermally microwaved at 800 W for 11 min. After completion of the reaction, it was allowed to ambient temperature and the white powdered samples were collected by centrifugation. The powdered samples were washed thoroughly with deionized water and ethanol to remove impurities possibly remaining in the final products. Finally, the samples were dried at 80 °C for 12 h in an oven.

4.2.3 Characterization

For characterization (UV-Vis, PL and TEM), the ZnO nanoparticles were dissolved in ethanol and sonicated for 10 min using a digital ultrasonic cleaner (Model: PS – 20A). The optical properties were determined by Photoluminescence (PL) spectroscopy using a Varian Cary

Eclipse EL04103870 fluorescence spectrophotometer and UV-Vis absorption spectroscopy using a Varian Cary Eclipse (Cary 50) UV-Vis spectrophotometer. For visualization of the sizes and morphology of the nanoparticles, transmission electron microscopy (TEM) was used and recorded using a FEI Technai T12 TEM microscope operated at an acceleration voltage of 200 kV. TEM samples were prepared by drop-casting the ethanol diluted samples on a 300 mesh carbon coated copper grids. Structural properties were analysed by powder X-ray diffraction using a Bruker MeasSrv (D2-205530)/D2-205530 diffractometer using secondary graphite monochromated CoK α radiation ($\lambda = 1.79026\text{nm}$) at 30 kV/30 mA. Measurements were taken using a glancing angle of incidence detector at an angle of 2° , for 2θ values between $10 - 90^\circ$ in steps of 0.026° with a step time of 37 s and at a temperature of 25°C . The light source (solar simulator) used for photocatalysis was an ORIEL SOL 2A, Newport, model – 69907 with input power: 190-264 VAC, 50/60 Hz, 202 A (serial number – 1723). The specific surface area was determined from 0.2 g using a Micromeritics TriStar 3000 instruments operated at -196°C . Before analysis, the samples were degassed at 150°C in N_2 for 3 h. The specific surface area was calculated by the Brunauer–Emmett–Teller (BET) method from N_2 adsorption data in the relative pressure range $P/P_0 = 0.05-0.30$. Total pore volumes of the samples were calculated at a relative pressure range $P/P_0 = 0.995$.

4.2.4 Photocatalytic degradation of Rhodamine B

The dye degradation experiments were conducted by preparing 500 mL stock solution of Rhodamine B with the desired concentration (e.g. 20 ppm). 100 mL of the stock solution was poured into a 200 mL cut beaker and mixed with a known mass (i.e. 0.16 g) of the ZnO nanoparticles. The dye-nanoparticles mixture was sonicated for 30 min in the dark in order to ensure that the ZnO nanoparticles were well dispersed in the solution. At the end of sonication, the mixture was subsequently stirred for 60 min using a magnetic stirrer and a stirrer bar in order to allow for equilibration between the dye molecules and the nanoparticles. Before the mixture was exposed to solar radiation, an aliquot ($\sim 4\text{ mL}$) was withdrawn and its absorbance measured, and that aliquot was labelled as ‘time zero’, which meant before exposure to light. The progress of degradation was monitored using the following equation (eq. 4.5):

$$\frac{C_t}{C_0} \times 100 \% \quad \text{eq. (4.5)}$$

Where C_t refers to the concentration of the dye after a certain time of irradiation and C_0 refers to the concentration of the dye before irradiation. The light was then switched on and constantly irradiated on the mixture that was continuously stirred. Aliquots were then subsequently withdrawn at 30 min intervals and their absorbance determined. The progress of the degradation was monitored by the change in the absorbance of the excitation peak (553 nm) of Rhodamine B using UV-Vis absorption spectroscopy. The pH of the dye solution was measured using a Starter 3100 pH Bench. The distance between the dye solution and solar simulator was 12 cm.

4.3 Results and Discussion

4.3.1 Structural properties

Figure 4.1 displays the PXRD patterns of ZnO nanoparticles synthesized at pH 7, 10 and 14. The diffraction peaks in the pattern of the nanoparticles for pH 7 and 10 were indexed to the hexagonal wurtzite phase of zinc oxide with the lattice constants $a = 3.250 \text{ \AA}$ and $c = 5.199 \text{ \AA}$, space group $P6_3mc$, which was in good agreement with the standard card (JCPDS – 01-080-0074). The diffraction peaks for the nanoparticles synthesized at pH 14 were indexed to the hexagonal zincite phase of zinc oxide (JCPDS – 01-070-2551), space group $P6_3mc$, with the lattice constants $a = 3.250 \text{ \AA}$ and $c = 5.207 \text{ \AA}$.

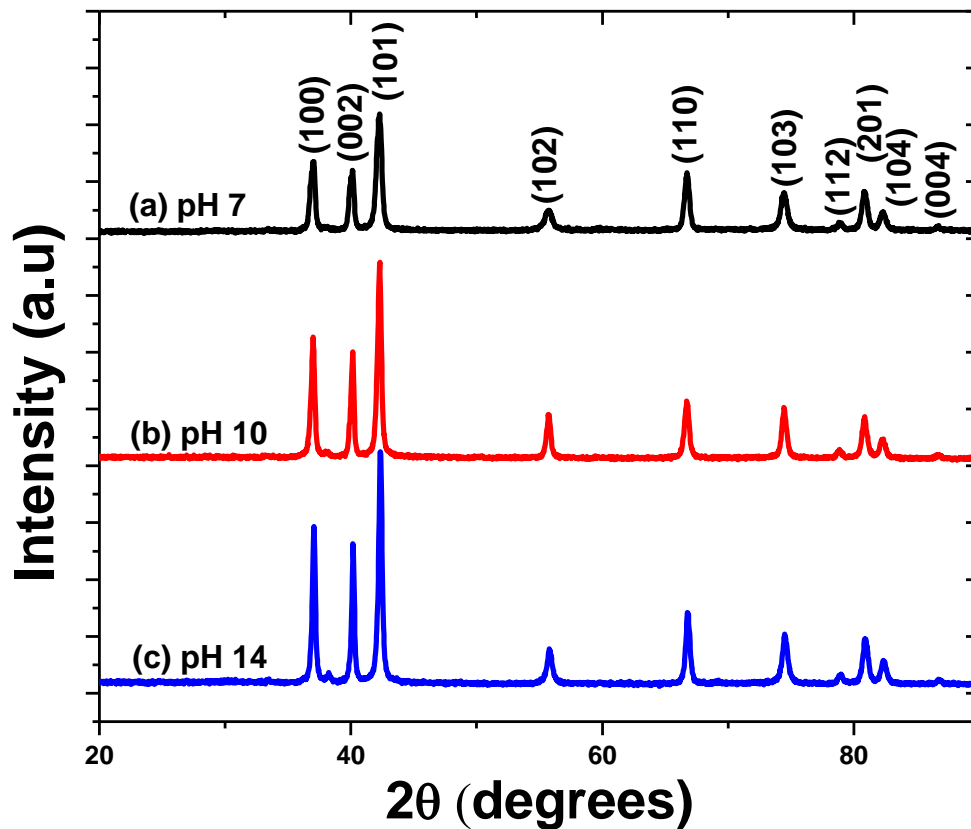


Figure 4.1: PXRD patterns of the ZnO nanoparticles synthesized at (a) pH 7, (b) pH 10, and (c) pH 14.

The good crystallinity of the synthesized ZnO nanoparticles was confirmed by the sharpness and the high intensity of the peaks. No peaks were correlated to any other phase, which indicated that the nanoparticles synthesized were free of any impurities. There is a small noticeable difference in values of the lattice constants, with the nanoparticles prepared at pH 7 and 10 having lattice constant $c = 5.199 \text{ \AA}$, while that of the nanoparticles at pH 14 was found to be longer at $c = 5.209 \text{ \AA}$. The increase in the length of the lattice constant can be attributed to the formation of rods that are oriented along the c -axis. An increase in the relative intensity of the (101) peak specifically for the nanoparticles synthesized at pH 14 indicated the presence of many planes along the c -axis of the ZnO nanoparticles [29].

The variation in the morphology of ZnO nanoparticles as the pH of the precursor solutions was altered is shown in Figure 4.2(a-c). A systematic morphological variation of the ZnO nanoparticles was observed as it changed from pseudo-spherical (Figure 4.2(a)), to bullet-like (Figure 4.2(b)), and further to rod-like (Figure 4.2(b)) morphology as the pH was varied from 7, 10 and 14, respectively. The trend observed was a change in the preferred growth direction as the pH was increased from neutral conditions (i.e. pH 7) to more basic conditions (i.e. pH 14). At neutral conditions, pseudo-spherical nanoparticles were formed, indicating that isotropic growth was favoured [30]. As the pH was increased to 10 and 14, it was observed that the preferred growth direction showed a deviation from isotropic growth (i.e. pseudo-spherical nanoparticles) into more anisotropic growth (i.e. bullet- and rod-like nanoparticles) [31].

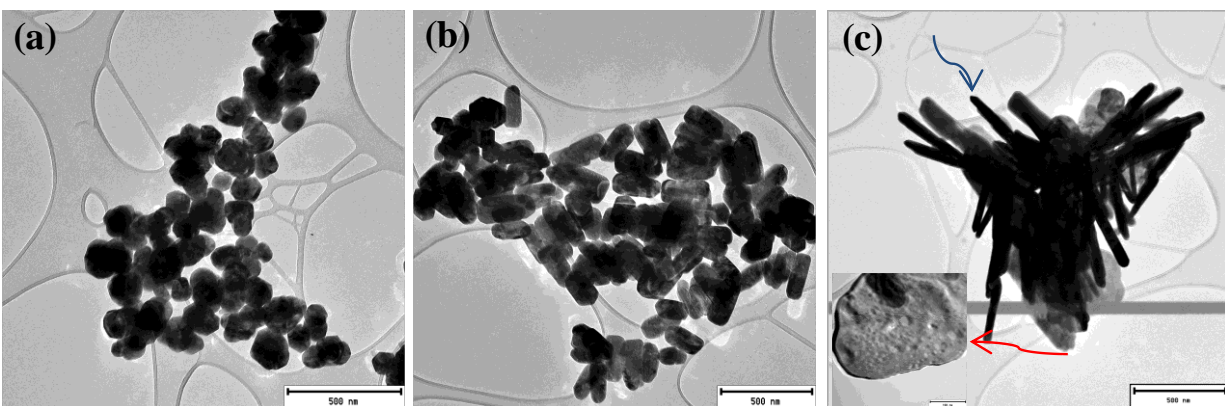


Figure 4.2: TEM micrographs of the different morphologies of ZnO nanoparticles synthesized at (a) pH 7, (b) pH 10, and (c) pH 14.

The change in the growth nature of the ZnO nanoparticles could be explained by looking at the concentration effects of OH⁻ and H⁺ ions on the growth mechanism [32, 33]. At medium pH values, (i.e. pH = 7), the H⁺ ions effective density was expected to be higher as opposed to very high pH values. The presence of sufficient concentrations of H⁺ in the precursor solution can prohibit the condensation and hydrolysis processes that took place during the growth process, which resulted in the polycondensation process forming smaller and fewer Zn(OH)₄²⁻ aggregates [34, 35]. The presence of low concentrations of the monomer was not sufficient to sustain anisotropic growth, as it requires the presence of abundant monomers. The high concentration of the H⁺ ions preferably reacted with the OH⁻ ions thus inhibiting growth along the [0001] plane (c-plane), favouring isotropic growth of the pseudo-spherical crystals. As the pH was increased by the addition of NaOH, the concentration of the H⁺ ions were decreased. The change in the dominant type of ions in the reaction medium from H⁺ to OH⁻ ions resulted in high rates of hydrolysis and polycondensation processes, which formed larger and many Zn(OH)₄²⁻ aggregates that promoted growth along the [0001] plane (c-axis) as confirmed by PXRD [34, 35]. Favoured growth along the [0001] direction (c-axis) formed anisotropic crystals such as bullets and rods. The inset in Figure 3.2(c) shows the plate-like nanoparticles (red arrow) that occurred in conjunction with the rod-like nanoparticles as the pH was increased to 14. At pH = 14, the effective OH⁻ ions density was increased and that resulted in unselective and uncontrollable condensation/hydrolysis processes. This resulted in the formation of larger particles (sheet-like), with no preferred growth direction, and rods that are interconnected to form branched like structures [34-37]. The possible growth mechanism for the branched like nanoparticles is shown in Figure 4.3.

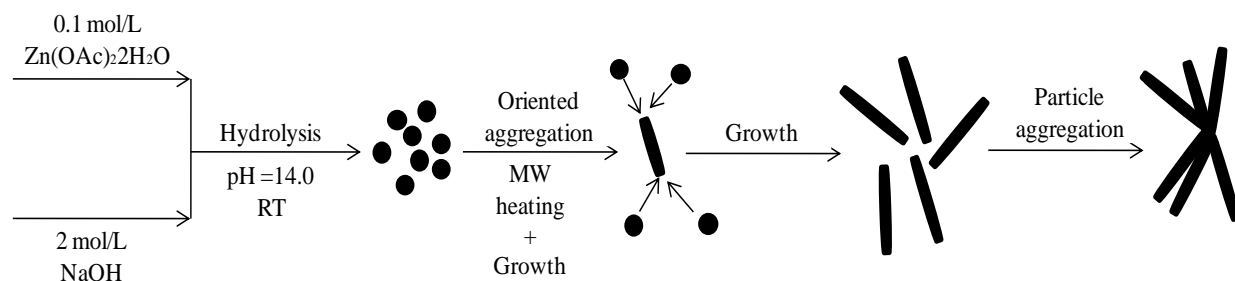


Figure 4.3: Possible growth mechanism of the aggregated rod like nanostructures.

The reaction between $\text{Zn}(\text{CH}_3\text{COO})_2 \cdot 2\text{H}_2\text{O}$ and NaOH produces the $\text{Zn}(\text{OH})_4^{2-}$ precipitate, which is transformed to ZnO upon exposure to heat. During the reaction, the rods grow and come into contact with one another. At the surface of the rods where contact occurs, nucleation takes place resulting in the formation of branched nanostructures [38]. Similar observation, that is, the formation of branched structures and flowers from nanorods has been observed previously by Jiang et al. [39]. A closer look at the ends of the rod-like nanoparticles (Figure 4.2(c)) reveals that they have tapered tips (blue arrow). This behaviour can be explained by the two processes, mass transport and dissolution, which are involved during crystal growth [40-42]. In the presence of sufficient monomers, mass transport dominates and promotes diffusion of the monomers into already formed crystal nuclei, allowing for further growth. As the reaction proceeds, the concentration of the $\text{Zn}(\text{OH})_4^{2-}$ monomers is reduced, and the effects of dissolution, which involves the removal of precursor components such as atoms, ions and molecules to the already formed crystal nuclei dominates [43-45]. The dissolution along the polar [0001] plane results to tapered ends. Peng [46] reported that in a given reaction medium, the required monomer concentration decreases in the following order: branched structures, rods, rice grains, and the dots. This means that decreasing the concentration of the monomers in the reaction medium, elongated shapes (e.g. rods) can be converted into dots if the monomer concentration is not sufficient. Also, dot shapes can be converted into elongated shapes at high monomer concentration [46]. SEM analysis (Figure 4.4) was performed to further confirm the morphological variation of ZnO because of pH.

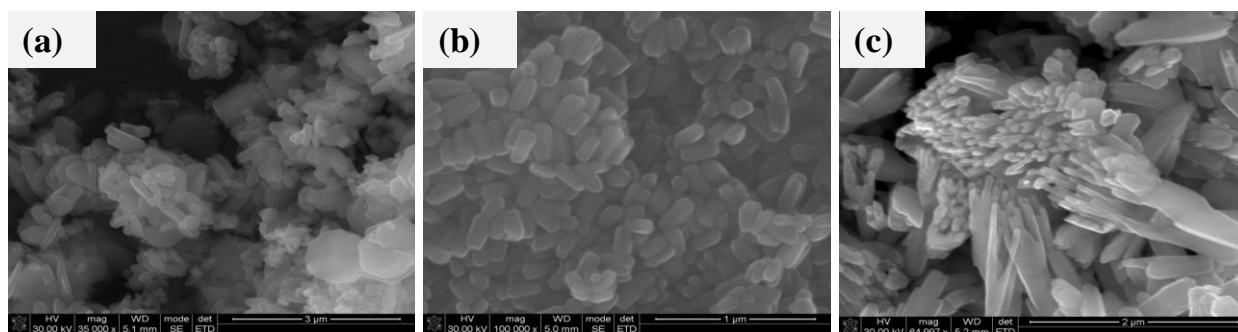


Figure 4.4: SEM images of the different morphologies of ZnO nanoparticles synthesized at (a) pH 7, (b) pH 10, and (c) pH 14.

The ZnO nanoparticles synthesized at pH 7 (Figure 4.4(a)) showed a pseudo spherical morphology. The sample is composed primarily of particles of nanometric sizes that are highly dispersed. Most of the nanoparticles have poorly defined crystal edges which resemble hexagonal shape. The nanoparticles synthesized at pH 10 (Figure 4.4(b)) showed bullet like nanoparticles that are monodispersed. Figure 4.4(c) shows the flower like morphology of the nanoparticles synthesized at pH 14. The morphology is made of rod like nanoparticles that have agglomerated such that they form a flower like structure. SEM analysis has therefore provided conclusive evidence that varying the pH of the precursor solution during synthesis result in changes to the morphology of ZnO

The specific surface area is an important structural parameter of nanoparticles and is highly dependent on the morphology. In this study, the variation in the surface area is easy to understand. The BET surface area of the pseudo-spherical, bullets and rods were found to be 14.73, 10.05 and 8.43 $\text{m}^2.\text{g}^{-1}$, respectively. Such results show an improved N_2 adsorption ability by the different morphologies and the highest surface area for the pseudo-spherical nanoparticles.

4.3.2 Optical properties

Using room temperature UV-Vis absorption and photoluminescence spectroscopy, the optical properties of the ZnO nanoparticles synthesized at different pH values were examined and are demonstrated in Figure 4.5 and 4.6. In the UV-Vis absorption spectra, exciton peak was observed for all the different morphologies, an absorption edge at ~ 388 nm was observed for all, which is characteristic of bulk hexagonal wurzite phase of ZnO.

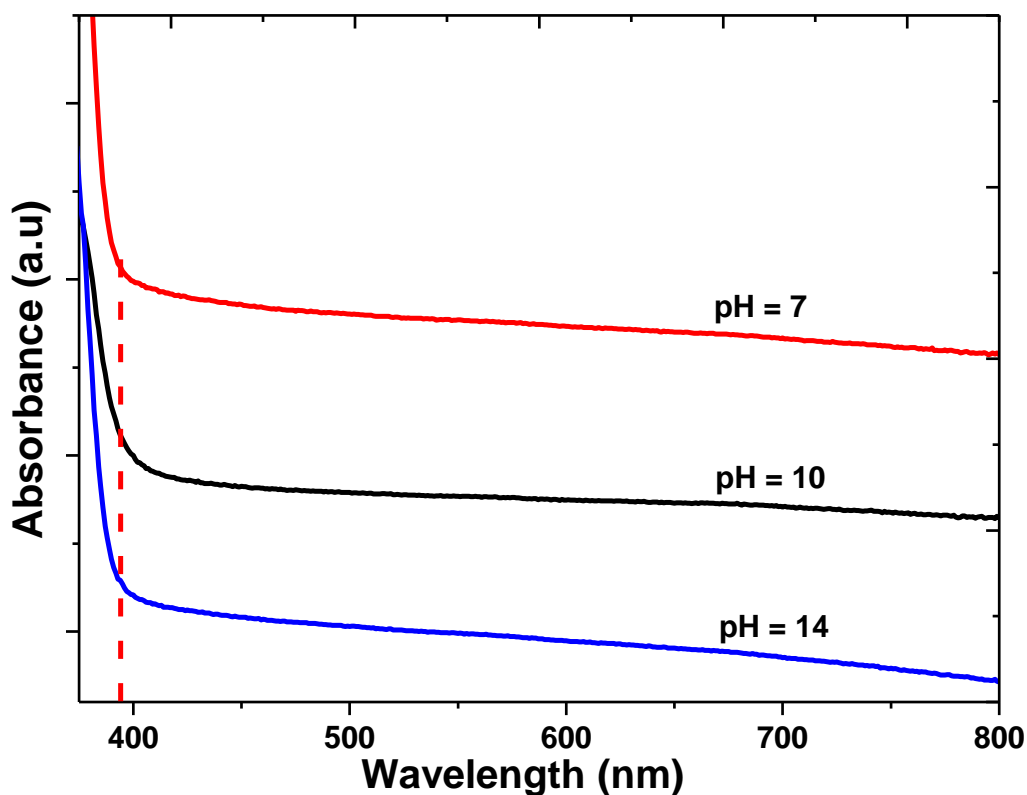
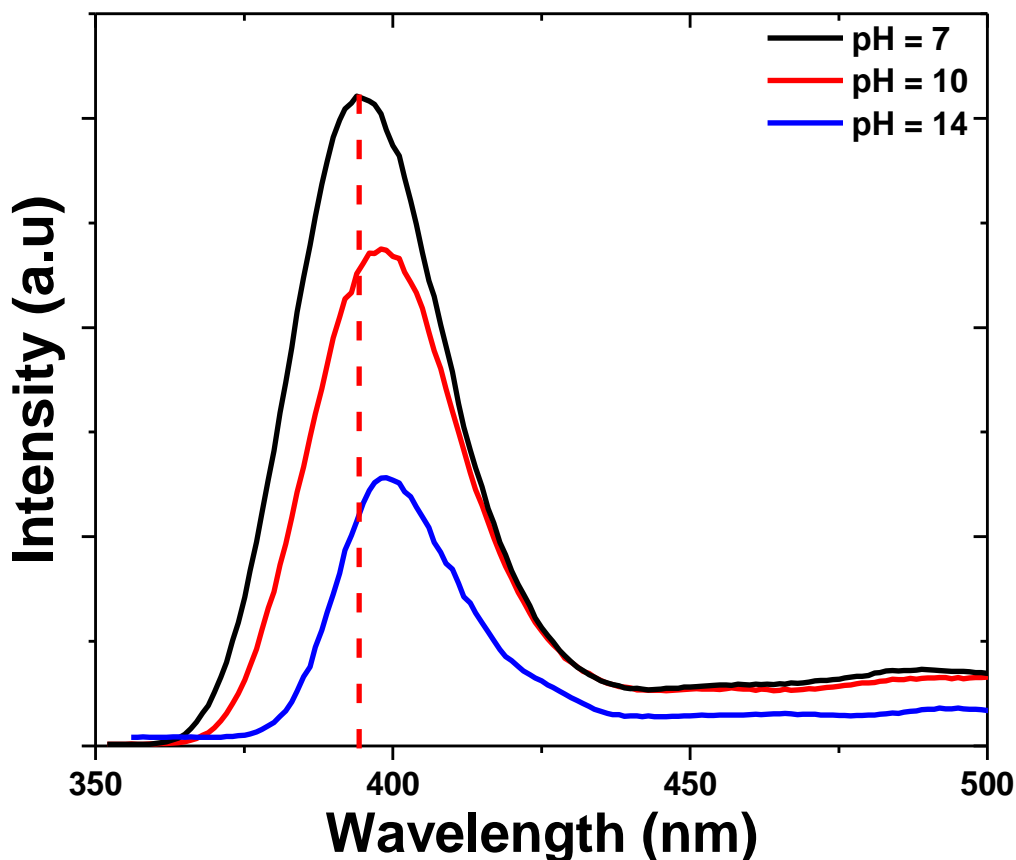


Figure 4.5: Room temperature absorption spectra of ZnO nanoparticles synthesized at different pH values.

The results obtained were found to be different and as such, a difference was expected in the absorption edge due to the size and morphology differences, which wasn't observed in UV-Vis results. The expectation was that the absorption edges of the smaller sized (i.e. higher surface area) nanoparticles were going to be blue shifted relative to those with larger sizes (i.e. lower surface area). It was presumed

that the reason this difference were not detected was because the difference in the nanoparticles was not so large to such an extent that a shift is observed. This phenomenon occurs when the nanoparticles are in the weak quantum confinement regime, which means that even though they differ from each other, they still exhibit optical properties which resemble those observed in their bulk counterpart [47]. A small degree of tailing was observed on the spectra of the different nanoparticles, which indicated that the nanoparticles were polydispersed. Contrary to the results obtained from UV-Vis absorption spectroscopy, a noticeable difference in the emission wavelength for the different morphologies was observed in the PL results as demonstrated in Figure 4.6.



4.6: Room temperature emission spectra and of the ZnO nanoparticles synthesized at different pH values.

Indicated by the red dotted line in the spectra, a blue shift was observed for the pseudo-spherical nanoparticles relative to the bullet- and rod like nanoparticles

which displayed emission maxima at 392, 397, and 399 nm, respectively. Although not significant, the blue shift of the emission wavelength relative to one another confirms the different sizes which were confirmed by the measured surface areas and TEM. Similarly to the explanation given in UV-Vis absorption spectra, it is assumed that the weak quantum confinement regime in the nanoparticles synthesized at different pH still dominates and hence the small variation in the emission wavelength was observed [47]. It is proposed that the small shift observed in PL was not observed in UV-Vis due to the fact that different techniques have different sensitivity in detecting small change in the property of a particular material. In this case, PL was the more sensitive technique able to reveal the blue shift as the morphology of the nanoparticles was changed.

The broadness of the peaks (i.e. large FWHM) in the spectra speaks to the polydispersed nature of the nanoparticles. An anomaly is observed with the emission wavelengths observed in PL as they are red shifted compared to the bulk ZnO emission wavelength of 388 nm this anomaly was attributed to the fact that since the size of the nanoparticles were much larger than the exciton Bohr radius of bulk ZnO the quantum size effect is very small to be observed [48]. Secondly, synthesis of nanoparticles using capping agents allows for presence of oxygen vacancies in the crystal structure of ZnO. The interaction between the capping agents and the interstitial oxygen vacancies promotes formation of trapped states. The trapped states form a series of energy level that are metastable within the band gap. The metastable energy levels promote red-shift of the band gap of ZnO [48].

4.4 Photocatalytic degradation of Rhodamine B

To show the dependence of photocatalytic activity of ZnO on morphology, the photocatalytic degradation of Rhodamine B was assessed by testing the activity of the pseudo-spherical, bullet- and rod-like nanoparticles. Time-dependent UV-Vis of Rhodamine B obtained during the degradation experiment conducted using the ZnO nanoparticles synthesized at pH 14 (i.e. rod-like particles) are shown in Figure 4.7. The absorbance of the absorption peak located at 553 nm

decreased as the dye solution was being exposed to light, and diminished after 210 min, which indicated that the dye molecules had been degraded. Apart from the decrease in absorbance, the shade of the pink colour of Rhodamine B changed with time until it was colourless. This colour change was also indicative of the removal of the dye molecules in the solution. All other morphologies followed a similar trend.

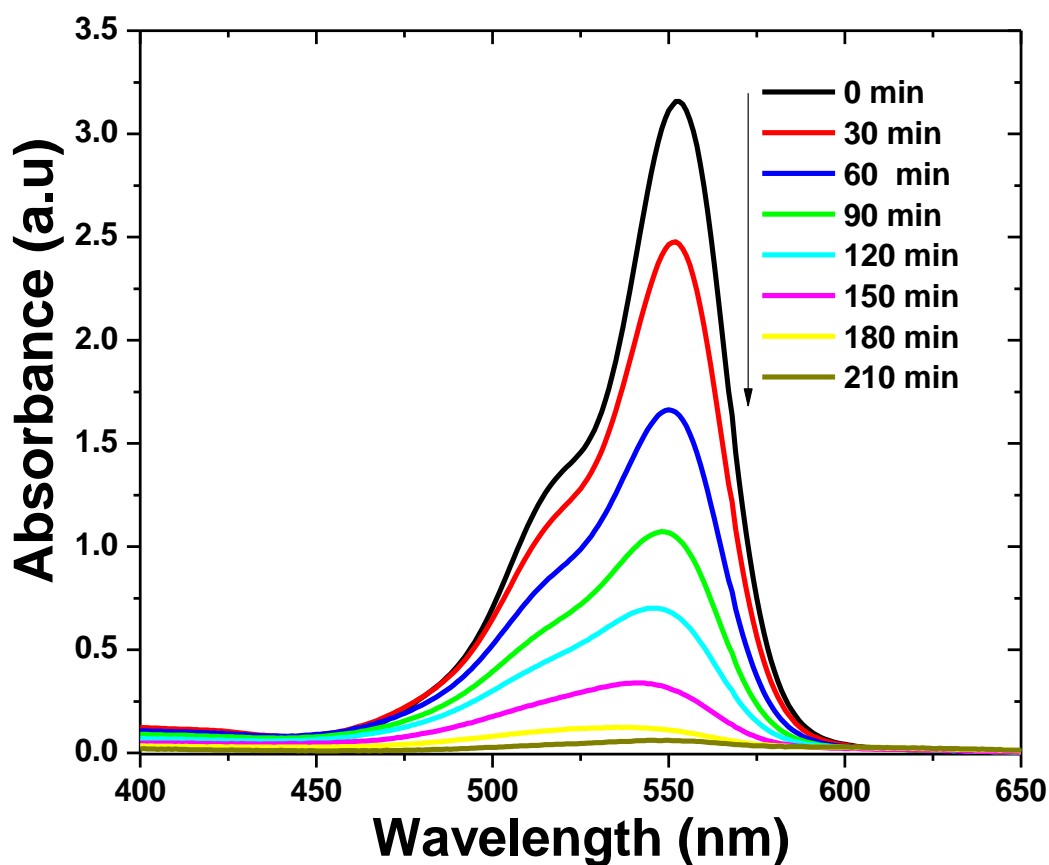


Figure 4.7: Typical UV-Vis spectra changes of Rhodamine B (20 ppm, neutral water pH) upon irradiation in the presence of ZnO (160 ppm) nanoparticles synthesized at pH 14.

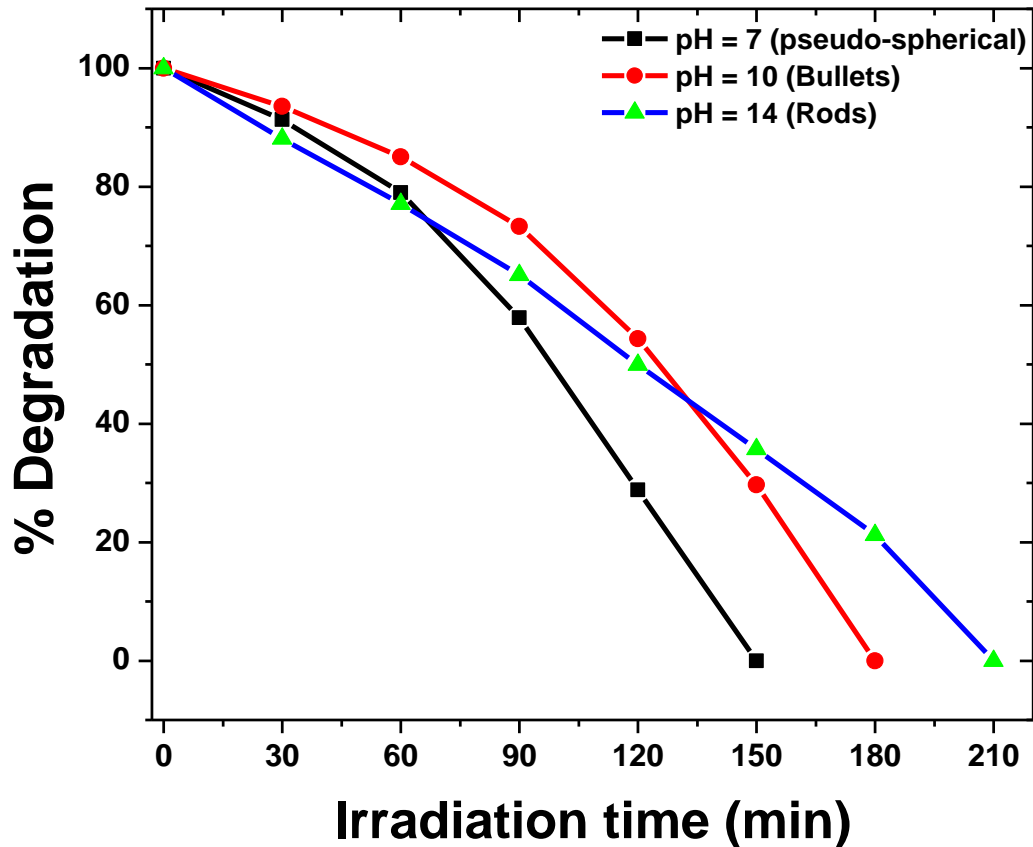


Figure 4.8: The % degradation versus irradiation time plot for the pseudo-spherical, bullet- and rod-like nanoparticles.

Figure 4.8 shows that the three different morphologies (i.e. pseudo-spherical, bullets and rods) were all able to degrade the dye but at slightly different rates. The pseudo-spherical, bullet and rod-like nanoparticles took 150, 180 and 210 min to completely degrade the dye, respectively. This difference in the photocatalytic activity of the different morphologies can be explained based on surface area and the proportion of exposed polar surfaces on the surface of ZnO. In this study, it was observed that the nanoparticles with the smallest aspect ratio (length of rod/rod diameter), being the pseudo-spherical nanoparticles, showed the highest efficiency in degrading the Rhodamine B dye. This showed that there was a size effect that influenced the rate of degradation. The BET results gave specific surface areas of 14.70, 10.05 and 8.430 $\text{m}^2\cdot\text{g}^{-1}$ for the, pseudo-spherical, bullets and rod-like nanoparticles, respectively. Nanoparticles with a high surface area are known to be more catalytically active due to the high amount of active sites that are readily available to degrade the dye molecules in solution. Another important factor that

hasn't been reported extensively in literature is the effect of certain crystal facets that are present in different morphologies of the nanoparticles [49-51]. Rod-like nanoparticles grow along the c-axis and are composed mainly of non-polar facets that are parallel to the c-axis. Spherical/hexagonal nanoparticles on the other hand undergo lateral growth and are composed mainly of polar facets that are perpendicular to the c-axis [52, 53]. Each of these morphologies differs from one another by the proportion of the [0001] and [000-1] polar facets that are exposed on the surface of ZnO crystals. Figure 4.9 clearly shows that the spherical/hexagonal nanoparticles have a higher proportion of polar [0001] and [000-1] facets than the bullet- and rod-like nanoparticles. The [0001] and [000-1] ($\gamma^0(0001\text{-Zn}) = 2.49 \pm 0.0063$, $\gamma^0(000-1\text{-O}) = 1.35 \pm 0.0063$) facets of ZnO have the highest surface energy than any other facets in ZnO nanocrystals [53].

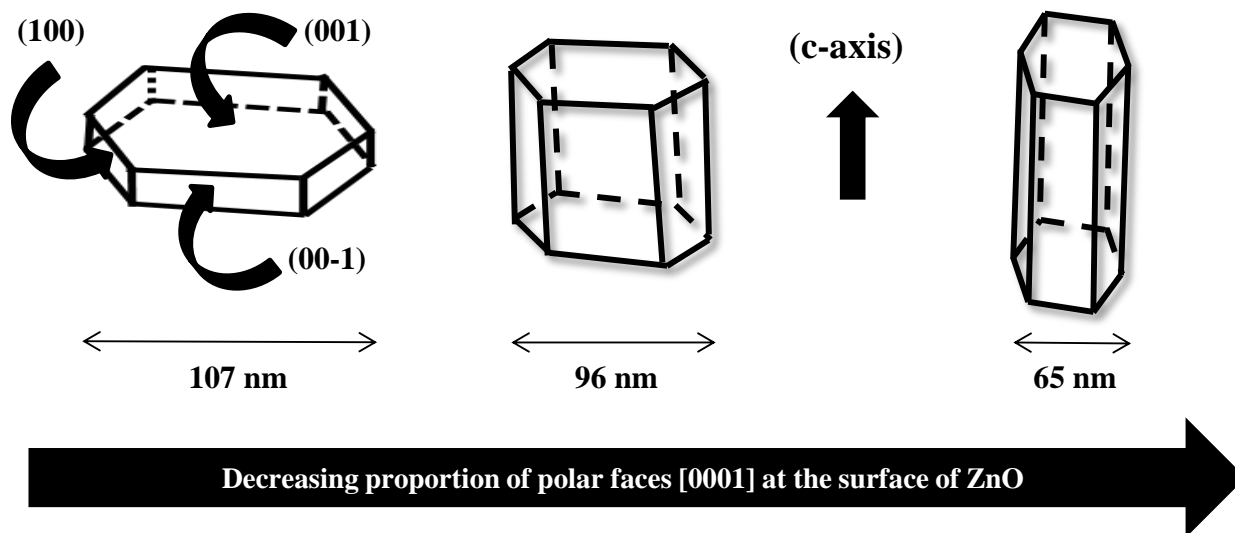


Figure 4.9: The dominant facets present on the surface of ZnO with different morphologies (modified from [53]).

This high surface energy means that the OH^- ions can be easily adsorb onto the [0001] face because of its positive charge caused by the high surface energy. The OH^- ions are the ones that have to come into contact with the surface of ZnO nanoparticles in order to be converted in OH^\bullet species that are responsible for degrading with the dye molecules [53, 54]. The high photocatalytic activity of the pseudo-spherical ZnO compared to the bullet- and rod-like nanoparticles is therefore attributed to both high surface area and large proportion of polar surfaces present. The rod-like nanoparticles that have a high aspect ratio (length of rods/rods

diameter) were the least effective in the degradation of Rhodamine B. Results obtained by Li et al. [55], provided a new way to look at the effect of morphology on photocatalytic activity [55]. They reported a good correlation between the amount of surface oxygen vacancies and the proportion of exposed polar surfaces on the surface of ZnO. Presence of high content of oxygen vacancies allow for good electron-hole pair separation because of the ability of oxygen to trap the photogenerated electrons. The rapid charge recombination is a drawback in ZnO and hence introducing a potential well for the electrons aids high photocatalytic activity [55]. In another study reported by McLaren et al. [56], they found that the plate-like particles were > five times more efficient in degrading methyl blue than rod-like particles [56]. They attributed the high photocatalytic activity of the plate-like particles to be due to the presence of high proportions of the [0001] and [000-1] facets which are more active than the non-polar (100) and (101) facets dominating in rod-like particles [58].

The kinetic study of the photocatalytic degradation of Rhodamine B using as-synthesized ZnO was investigated with the Langmuir–Hinshelwood kinetic model, which also covers the adsorption properties of the substrate on the photocatalyst surface [59]. The equation is represented as follows:

$$Rate = \frac{dC}{dt} = k \frac{KC}{1+KC} \quad \text{eq. 4.6}$$

Where C is the concentration of Rhodamine B at the irradiation time, k the reaction rate constant, and K is the degradation coefficient of the reactant. Where k' is the apparent rate constant. A plot of $\ln(C_0/C)$ versus time results in a straight line; its slope is the pseudo first- order degradation rate constant (K_{app}) [59, 60]. The experimental data obtained in the kinetic study of Rhodamine B degradation when different ZnO photocatalyst morphologies were used was fitted with the Langmuir–Hinshelwood kinetic model. The results obtained are illustrated in ANNEXURE A.

The plots of the data gave a straight line, showing that the photocatalytic degradation of Rhodamine B can be described by the pseudo-first-order kinetic model [59]. The correlation coefficient constant for the fitted line and the rate constants are graphically obtained (ANNEXURE A) and their values are represented in table 4.1.

Table 4.1: Rate constants for photocatalytic degradation of Rhodamine B using different ZnO morphologies.

Morphology	Initial concentration (ppm)	ZnO concentration (ppm)	K_{app}	R^2
Pseudospherical	20	160	0.022	0.968
Bullets	20	160	0.020	0.966
Rods	20	160	0.018	0.981

The rate constant for the degradation of Rhodamine B using the different morphological forms confirm that the rate at which the pseudo-spherical nanoparticles degraded the dye molecules was faster compared to the bullets and rod-like nanoparticles.

4.5 Conclusion

This study showed that the application of an easy and quick microwave assisted heating method for the synthesis of pure ZnO nanoparticles of various controlled morphologies and their activity in photocatalysis. A methodical investigation of the effect of pH on the morphology showed that the pH of the precursor solution has a significant influence on the structural properties of ZnO nanoparticles. Small pseudo-spherical nanoparticles were formed at pH 7 and changes were observed when the pH was increased to 10 and 14, resulting in bullet- and rod-like nanoparticles. On the basis of microscopic (TEM) results, it can be concluded that the morphology/size of the ZnO nanoparticles can be manipulated by varying the pH of the precursor solution. Compositional analysis (PXRD) showed that the synthesized ZnO nanoparticles were pure and were highly crystalline. Furthermore, the results from UV-Vis absorption and photoluminescence spectroscopy showed that the as-synthesized ZnO nanoparticles possessed good optical properties, which are comparable to those observed in bulk ZnO. The surface area influenced the photocatalytic activity with the nanoparticles having the highest surface area being more efficient in degrading Rhodamine B. Apart from higher surface area resulting in high degradation rates; it was proposed that the type of facets that are exposed on the different ZnO morphologies played a role in influencing the rate of degradation. The morphology with more polar facets ([0001] and [000-1]) was more photocatalytically active than the morphologies composed dominantly of polar facets (100).

4.6 References

- [1] P. Rai, W.K. Kwak, and Y.T. Yu, *ACS Applied Material Interfacets*, **5**, (2013) 3026-3032
- [2] S.K.N. Ayudhya, P. Tonto, M. Okorn, V. Pavarajam, P. Praserttham, *Crystal Growth and Design*, **6**, (2006) 2446-2450
- [3] M. Navaneethan, J. Archana, and Y. Hayakawa, *CrystEngComm*, **15**, (2013) 8246-8249
- [4] M. Navaneethan, J. Archana, M. Arivanandhan, Y. Hayakawa, *Physica Status Solidi Rapid Research Letters*, **6**, (2012) 120-122
- [5] M. Hasanpoora, M. Aliofkhazraeia, H. Delavaria, *Procedia Materials Science*, **11**, (2015) 320–325 [6] S. Li, Z. Wu, W. Li, Y. Liu, R. Zhuo, D. Yan, W. Juna, P. Yanab, *CrystEngComm*, **15**, (2013)1571
- [7] G.O. Siqueira, T. Matencio, H.V. Silva, Y.G. Souza, J.D. Ardisson, G.M. Limaa, A.O. Porto, *Physical Chemistry*, **15**, (2013) 6796
- [8] I. Mouritys, P. Silva, G. Byzynski, C. Ribeiroc, E. Longo, *Journal of Molecular Catalysis A: Chemical*, **417**, (2016) 89–100
- [9] K. Zhou, X. Hu, B. Chen, C. Hsueh, Q. Zhang, J. Wang, Y. Lin, C. Chang, *Applied Surface Science*, **383**, (2016) 300–309
- [10] C. Chang, J. Wang, T. Ouyang, Q. Zhang, Y. Jing, *Materials Science and Engineering B*, **196**, (2015) 53–60
- [11] H.C. Lee, W. Liu, S. Chai, A.R. Mohamed, C.H.Voon, U. Hashim, M. K. Arshad, P.Y.P Adelyn, A.R.N. Huda, S.M. Kahar, N.M.S Hidayah, C.W. Lai, C. Khe, *Procedia Engineering*, **184**, (2017) 460–468
- [12] S. Sathish, S. Balakumar, *Journal of Luminescence*, **190**, (2017) 272–278
- [13] R. Bekkari, L. laâna, D. Boyer, R. Mahiou, B. Jaber, *Materials Science in Semiconductor Processing*, **71**, (2017) 181–187

- [14] M. Zimmermann, B. Temel, and G. Garnweitner, *Chemical Engineering and Processing*, **74**, (2013) 83–89
- [15] R. Ashraf, S. Riaz, S.S. Hussain, and S. Naseem, *Materials Today: Proceedings*, **2**, (2015) 5754-5759
- [16] J. Ungula, B.F. Dejene, H.C. Swart, P.B. Bhargav, N. Ahmed, B. Chandra, and S. Dhara, *Physica B: Condensed Matter*, **457**, (2015) 96-102
- [18] H. Yuan, L. Zhang, M. Xu, and X. Du, *Journal of Alloys and Compounds*, **651**, (2015) 571-577
- [19] S.S. Alias, A.B. Ismail, and A.A. Mohamad, *Journal of Alloys and Compounds*, **499**, (2010) 231-237
- [20] K. Dai, G. Zhu, Z. Liu, Q. Liu, Z. Chen, and L. Lu, *Materials Letters*, **67**, (2012) 193–195
- [21] K. Engelkemeier, O. Grydin, and M. Schaper, *Powder Technology*, **319**, (2017) 204–209
- [22] B. Cao, and W. Cai, *Journal of Physical Chemistry C*, **112**, (2008) 680-685
- [23] Z.A. Peng, and X. Peng, *Journal of American Chemical Society*, **124**, (2002) 13
- [24] M. Hasanpoor, M. Aliofkhazraei, and H. Delavari, *Procedia Materials Science*, **11**, (2015) 320-325
- [25] H. Wang, C. Li, H. Zhao, J. Liu, *Advanced Powder Technology*, **24**, (2013) 599–604
- [26] N.A. Khaldoon, N. Bidin, *Applied Surface Science*, **394**, (2017) 498–508
- [27] F. Motasemi, M.T. Afzal, *Renewable and Sustainable Energy Reviews*, **28**, (2013) 317–330
- [28] M. Bhattacharyaa, L. Punathilb, T. Basak, *International Communications in Heat and Mass Transfer*, **82**, (2017) 145–153
- [29] S. Kundu, S. Sain, B. Satpati, S.R. Bhattacharyy and S.K. Pradhan, *RSC Advances*, **5**, (2015) 23101–23113
- [30] T. Hsieh, J. Chen, C. Huang and W. Wu, *Chemistry of Materials*, **28**, (2016) 4507–4511

- [31] F. Fenske, B. Selle and M. Birkholz, Japanese Journal of Applied Physics, **44**, (2005) 662–664
- [32] Y. Xia, J. Wang, R. Chen, D. Zhou and L. Xiang, Crystals, **6**, (2016) 11-16
- [33] J. Wang, S. Hou, L. Zhang, L. Chen and J. Xiang, CrystEngComm, **16**, (2014) 7115–7123
- [34] J. Li, S. Srinivasan, G. N. He, J. Y. Kang, S. T. Wu, and F. A. Ponce, Journal of Crystal Growth, **310**, (2008) 599–603.
- [35] R. Wahab, Y. Kim, and H. Shin, Materials Transactions, **50**, (2009) 2092–2097
- [36] F.M. Omar, H.A. Aziz, and S. Stoll, Journal of Colloid Science and Biotechnology, **3**, (2014) 1–10
- [37] S.S. Alias, A.B. Ismail, A.A. Mohamad, journal of Alloys and Compounds, **499**, (2010) 231–273
- [38] S. Pung, W. Lee, and A. Aziz, International Journal of Inorganic Chemistry, **2012**, (2012) ISSUE NO 608183
- [39] Y. Jiang, X. Wu, W. Zhang, L. Ni, and Y. Sun, Journal of Semiconductors, **32**, (2011) 3-13
- [40] J. Shen, Y. Li, H. Gu, F. Xia, and X. Zuo, Chemical Reviews, **114**, (2014) 7631 - 7677
- [41] J. Polte, Royal Society of Chemistry, **17**, (2015) 609 – 6830
- [42] E. Matejevic, and P. Scheiner, Journal of Colloid and Interface Science, **63**, (1978) 509–524
- [43] S. Cho, S. Jung, and K. Lee, Journal of Physical Chemistry C, **112**, (2008) 12769–12776
- [44] J. Zhang, L. Sun, J. Yin, H. Su, C. Liao and C. Yan, Chemistry of materials, **14**, (2002) 4172-4177
- [45] A. Wei, X.W. Sun, C.X. Xu, Z.L. Dong, Y. Yang, S.T. Tan, and W. Huang, Nanotechnology, **127**, (2006) 1740 – 1744
- [46] X. Peng, Advanced Materials, **15**, (2003) 459–463

- [47] R.U. Joep, J.H. Pijpers, E. Groeneveld, R. Kool, C. Donega, D. Vanmaekelbergh, C. Delerue, G. Allan, and M. Bonn, *Nano Letters*, **12**, (2012) 4937–4942
- [48] X. Wu, B. Zou, J. Xu, B. Yu, G. Tang, G. Zhang, and W. Chen, *Nanostructured Materials*, **8**, (1997) 179-189
- [49] R. Boppella, K. Anjaneyulu, P. Basak, and S. V. Manorama, *Journal of Physical Chemistry C*, **117**, (2013) 4597–4605
- [50] E. Debroye, J.V. Loon, H. Yuan, K.P. F. Janssen, Z. Lou, S. Kim, T. Majima, and M.B.J. Roeffaers, *Journal of Physical Chemistry Letters*, **8**, (2017) 340–346
- [51] S. Das, K. Dutta, and A. Pramanik, *CrystEngComm*, **15**, (2013) 6349-6358
- [52] A. Pimentel, J. Rodrigues, P. Duarte, D. Nunes, F. M. Costa, T. Monteiro, R. Martins, and E. Fortunato, *Journal of Material Science*, **50**, (2015) 5777–5787
- [53] M. Rezapour, and N. Talebian, *Material Chemistry and Physics*, **129**, (2011) 249–255
- [54] R. Mohammad, A.S. Alenezi, K. D. G. I. Jayawardena, M.J. Beliatis, S.J. Henley, and S.R. P. Silva, *Journal Physical Chemistry C*, **117**, (2013) 17850–17858
- [55] S. Kuriakose, B. Satpati and S. Mohapatra, *Physical Chemistry*, **16**, (2014) 12741-12749
- [56] G. R. Li, T. Hu, G. L. Pan, T. Y. Yan, X. P. Gao and H. Y. Zhu, *Journal of Physical Chemistry C*, **112**, (2008) 11859–11864
- [57] A. McLaren, T. Valdes-Solis, G. Li, and S.C Tsang, *Journal of American Chemical Society C*, **131**, (2009) 12540–12541
- [58] C.S. Turchi, and D.F. Ollis, *Journal of Catalysis*, **122**, (1990) ISSUE NO178
- [59] N. Barka, and Y. Ait-Ichou, *Arabian Journal of Chemistry*, **3**, (2010) 279-283
- [60] M.V. Shankar, B. Nappolian, S. Sakthivel, B. Arabindo, M. Palanichamy, and V. Murugesan, *Indian Journal of Engineering and Materials Sciences*, **8**, (2001) 104-109

Chapter 5: Effect of reaction time on the size, morphology and photocatalytic activity of ZnO nanoparticles.

5.1 Introduction

Scientists have been fascinated by the ability to prepare mono-dispersed nanoparticles of specific sizes ever since Faraday prepared gold solutions composed of various colours in 1857 [1]. Since then, researchers have attempted to synthesize various morphological forms such as spheres, rods, flowers, belts, and disks with sizes ranging from a few nanometres to several micrometres [2-4]. The drive behind this is not only to achieve morphological and size diversity, but also to get a better understanding of the underlying principles that allow for the formation of a distinct morphology and the different properties associated with the various synthetic materials [6, 7]. In any synthetic products that are produced, it is important to find a plausible growth mechanism that led to the formation of that particular morphology or size [5].

Previously accepted descriptions of particle growth have been focused on the Ostwald ripening mechanism. According to this mechanism, nucleation causes the formation of very small nuclei in a reaction medium that has reached supersaturation. Once the critical cluster size has been ascertained, growth proceeds through addition and removal of precursor components such as atoms, ions and molecules to the already formed crystal nuclei through processes known as mass transport and dissolution. The rate of removal of precursor components from an already formed particle is said to increase rapidly for smaller particles. As a result, in a reaction medium made up of different sized particles, the large particles tend to grow at the expense of the smaller ones forming much larger particles [8-10].

Due to the simplicity of the Ostwald ripening mechanism, it was generally accepted as a plausible way to look at the growth of spherical crystals. More advanced research has managed to produce more complex shapes (e.g. rods, bullets, disks, etc.) whose growth process cannot be easily explained using the Ostwald ripening mechanism. This meant that crystal growth took place using other mechanisms [11]. One plausible mechanism that has been proposed is called oriented attachment. This mechanism is based on the idea that when particles that are close to

each other and oriented along the same crystallographic direction, they can change their orientation spontaneously and rearrange in such a way that they are able to coalesce, resulting in further growth.

Nanocrystals grown in this way commonly show a great deal of anisotropic growth characterized by shapes that are highly irregular. In the case where the nature of the orientation occurs in an orderly fashion, larger single crystals may be formed through aggregation of primary particles [8-11]. In the case where surface area is important, such as when the synthesized nanoparticles have to be used as photocatalysts, the formation of larger particles reduces the photocatalytic activity of the nanoparticles. Hence, it became important to put in an effort to synthesize different sizes of ZnO nanoparticles and study the effect that the size of the ZnO nanoparticles had on the photocatalytic activity. Herein, we report on the synthesis of ZnO nanoparticles using microwave assisted heating method. The effect of different heating conditions on the size, morphology and photocatalytic activity of the ZnO nanoparticles on the degradation of Rhodamine B has been evaluated. Various methods such as sol-gel, CVD and colloidal synthesis methods have been previously used to produce ZnO. These methods are however associated with long reaction times and high temperatures. In the quest to finding a synthesis method capable of reducing reaction times while producing uniform particle sizes, microwave has emerged as an effective method to use [12]. Microwave heating method is based on heating materials by dielectric heating effects. When a material that has a permanent dipole is exposed to an oscillating microwave field, the dipoles in the material will align with the field. This alignment causes rotation that results in friction, and ultimately in heat energy [13, 14].

5.2 Synthesis procedure

5.2.1 Chemicals and materials

Zinc acetate dehydrate ($\text{Zn}(\text{CH}_3\text{COO})_2 \cdot 2\text{H}_2\text{O}$), 98 %, was obtained from Sigma Aldrich, 98 % sodium hydroxide (NaOH) from Glassworld and reagent grade urea ($\text{CO}(\text{NH}_2)_2$) was obtained from Promark Chemicals. Rhodamine B was obtained at MAY and BAKER LTD. A Universal 320R sonicator (t/min = 10, RPM = 7000) was obtained from Hettich Lab Technology and a Microwave Reaction System, (Multiwave 3000 SOLV) was obtained from Anton Paar. All chemicals were used as received without any further purification.

5.2.2 Synthesis of ZnO nanoparticles

ZnO was synthesized using a simple microwave (MW) assisted heating method. Zinc acetate dehydrate was dissolved in 37.5 mL of deionized water in a 100 mL beaker to make a 0.1 M solution. About 0.6 g of urea was dissolved separately in 10 mL deionized water and added to the 0.1 M zinc acetate dihydrate solution in order to aid the hydrolysis of the Zn^{2+} cations. The mixture was then adjusted to pH 10 using 0.2 M NaOH, which resulted in the formation of a white aqueous precipitate [1]. The precipitate was then vigorously stirred with the help of a magnetic stirrer for 20 min at room temperature. The white aqueous precipitate was transferred into two vessels and hydrothermally microwaved at 400 W (5 min step time) for 30 min until the final temperature reached 200 °C, this sample was denoted as 'time 30'. Using the same method, four other samples were synthesized by varying the microwave power which resulted in reaction times of 18, 15, 11 and 8 min. These products were denoted as time 18, 15, 11 and 8, respectively. The time differences were achieved as follows: time 18 and 15 were synthesized at MW powers of 600 and 800 W, respectively, using a 5 min step time. Time 11 was synthesized at MW power of 800 W with 1 min step time. Lastly, time 8 was first heated to 50 °C using a hot plate then microwaved at 800 W with 1 min step time. After completion of the reaction, the resulting white powder was allowed to naturally cool to room temperature and was collected by centrifugation. The powdered samples were then washed thoroughly with deionized water and

ethanol to remove impurities possibly remaining in the final products. Finally, the samples were dried at 80 °C for 12 h using an oven.

5.2.3 Photocatalytic degradation of Rhodamine B

Typically, the dye degradation experiment was conducted by preparing 100 mL solution of Rhodamine B (i.e. test dye) with the desired concentration (i.e. 20 ppm) in a 200 mL beaker and mixed with a known concentration (160 ppm) of the ZnO nanoparticles. The dye-photocatalyst mixture was sonicated for 30 min in the dark in order to ensure that the ZnO nanoparticles were well dispersed in the solution. At the end of sonication, the mixture was subsequently stirred for 60 min using a magnetic stirrer and a stirrer bar in order to allow for equilibration between the dye molecules and the photocatalyst. Before the mixture was exposed to solar radiation, an aliquot was withdrawn and its absorbance measured, and that aliquot was labelled as ‘time zero,’ which meant before exposure to light. The progress of degradation was monitored using the following equation:

$$\frac{C_t}{C_0} \times 100\% \quad \text{eq. (5.1)}$$

Where C_t refers to the concentration of the dye after a certain time of irradiation and C_0 refers to the concentration of the dye before irradiation. The light was then switched on and constantly irradiated on the mixture that was continuously stirred. Aliquots were then subsequently withdrawn at 30 min intervals and their absorbance determined. Each aliquot (~ 4 mL) was collected using a 10 mL syringe fitted with a 0.2 μm syringe filter. The syringe filter was used to ensure that no residual ZnO nanoparticles were in the aliquot during the analysis of the dye solution. The progress of the degradation was monitored by the change in the absorbance of the excitation peak (553 nm) of Rhodamine B using UV-Vis Spectroscopy.

5.2.4 Characterization

Prior to characterization, the ZnO nanoparticles were dissolved in ethanol and sonicated for 10 min using a Digital ultrasonic cleaner (Model: PS-20A). The optical properties were determined by photoluminescence (PL) spectroscopy using a Varian Cary Eclipse EL04103870 fluorescence spectrophotometer and UV-Vis absorption spectroscopy using a Varian Cary Eclipse (Cary 50) UV-Vis spectrophotometer. For visualization of the sizes and morphology of the nanoparticles, Transmission Electron Microscopy (TEM) was used and recorded using a FEI Technai T12 TEM microscope operated at an acceleration voltage of 120 kV. TEM samples were prepared by drop-casting the ethanol diluted samples on a 300 mesh copper grids. Structural properties were analysed by Powder X-ray Diffraction using a Bruker MeasSrv (D2-205530) diffractometer equipped with a secondary graphite monochromated $\text{CoK}\alpha$ radiation ($\lambda = 1.79026$ nm) at 30 kV/30 mA. Measurements were taken using a glancing angle of incidence detector at an angle of 2° , for 2θ values between 10 - 90° in steps of 0.026° with a step time of 37 seconds and at a temperature of 25°C . The light source (solar simulator) used for photocatalysis was an ORIEL SOL 2A, Newport, model – 69907 with input power: 190-264 VAC, 50/60 Hz, 202 A (serial number – 1723).

5.3 Results and Discussion

5.3.1 Structural properties

To determine the crystal phase and crystallinity of the nanoparticles synthesized at various periods (i.e. 8, 11, 15, 18, and 30 min), PXRD analysis was performed and the results are shown in Figure 5.1. All the nanoparticles were single phase compounds as they could be matched to the hexagonal phase of ZnO as reported in the JCPDS [15] database as shown in Table 5.1. The strong and sharp peaks of the different nanoparticles showed that they were highly crystalline. There were no additional peaks in the diffractograms which indicated that the crystalline ZnO nanoparticles were the sole component synthesized with no impurities present. Varying the reaction time had no significant influence on the crystal structure of the nanoparticles as there were no significant differences in the position of the peaks for all the difference samples. However, there were slight differences in the full width half maximum values (FWHM) as shown in Table 5.1.

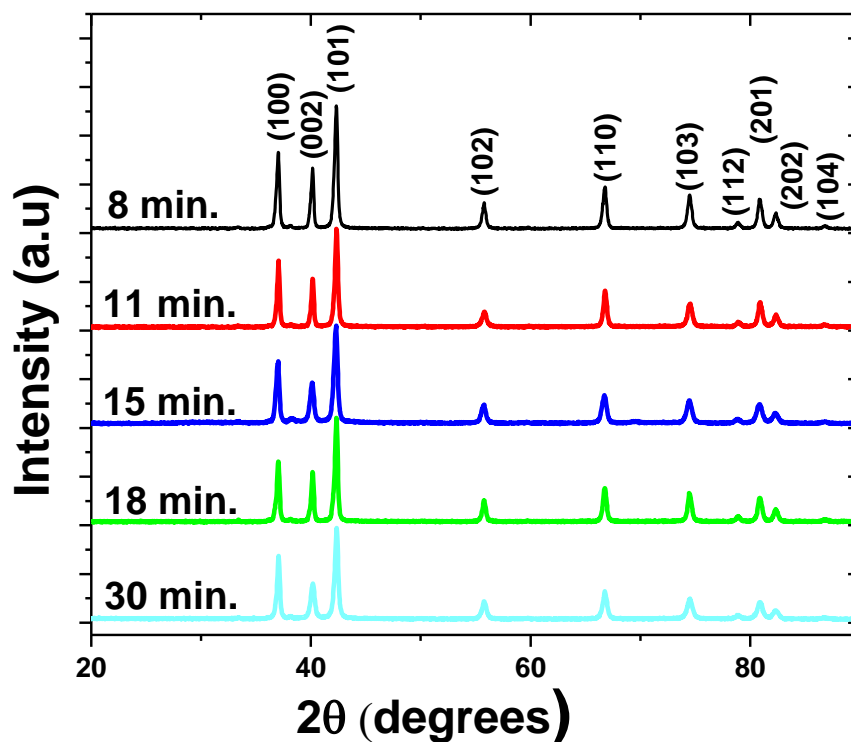


Figure 5.1: PXRD diffractograms of ZnO nanoparticles prepared at different reaction times using microwave assisted heating.

Table 5.1: Corresponding PXRD data of the different ZnO.

Reaction time	Compound name	Card number	FWHM (10^{-3}) (radians)	Crystallite Size (nm)
8	Zincite, Syn	01-070-2551	8.64	20.0
11	Zincite, Syn	01-070-2551	6.21	27.8
15	Zincite, Syn	01-070-2551	5.47	31.6
18	ZnO	01-079-2205	5.45	31.7
30	ZnO	01-079-2205	4.35	39.7

The difference in the FWHM is characteristic of the size of the nanoparticles [16]. It has been reported that the internal reflections that occur within a system (i.e. ZnO) due the smaller sized nanoparticles are capable of promoting intense spreading of the diffraction peaks [17]. This principle is supported by the size of the crystallites (Table 5.1) calculated using the Scherrer's equation (eq. 5.2):

$$D = 0.9\lambda/\beta\cos\theta \quad \text{eq. (5.2)}$$

Where D is the crystallite size, λ the wavelength of Co K_{α} radiation (0.179026 nm), β the full-width half maximum (FWHM) of the most intense peak (101 plane) in the diffraction pattern, θ is the angle which is obtained from the 2θ corresponding to the (101) plane (maximum intensity peak) in radians. The increase in particle size with increasing reaction time is indicative of coalescence occurring during the course of the reaction resulting in larger nanoparticles. Overall, the microwave assisted heating route comes with the benefit of obtaining pure ZnO nanoparticles at both short and long reaction times.

TEM micrographs of the ZnO nanoparticles synthesized at different reaction times are illustrated in Figure 5.2. The sizes of the nanoparticles (N = 100) were determined using ImageJ. The diameter of the nanoparticles was reported for hexagonal nanoparticles and for bullet-like nanoparticles both the width and length are reported. For reaction time of 8 min, the average length and width of the bullet-like nanoparticles was 158 and 80 nm, respectively, while the hexagonal nanoparticles had an average diameter of 69 nm. At 11 min reaction time, the average length and width of the bullet-like nanoparticles was found to be 87 and 165 nm, respectively, with the hexagonal nanoparticles having an average diameter of 92 nm. The mean nanoparticles diameter was found to be 91, 168, 332 nm for the hexagonal nanoparticles synthesized for 15, 18 and 30 min, respectively. From the calculated dimensions of the nanoparticles, a positive correlation between the size of the ZnO nanoparticles and the reaction time was observed. The size of the ZnO nanoparticles increased as the reaction time increased and decreased as the reaction time was decreased.

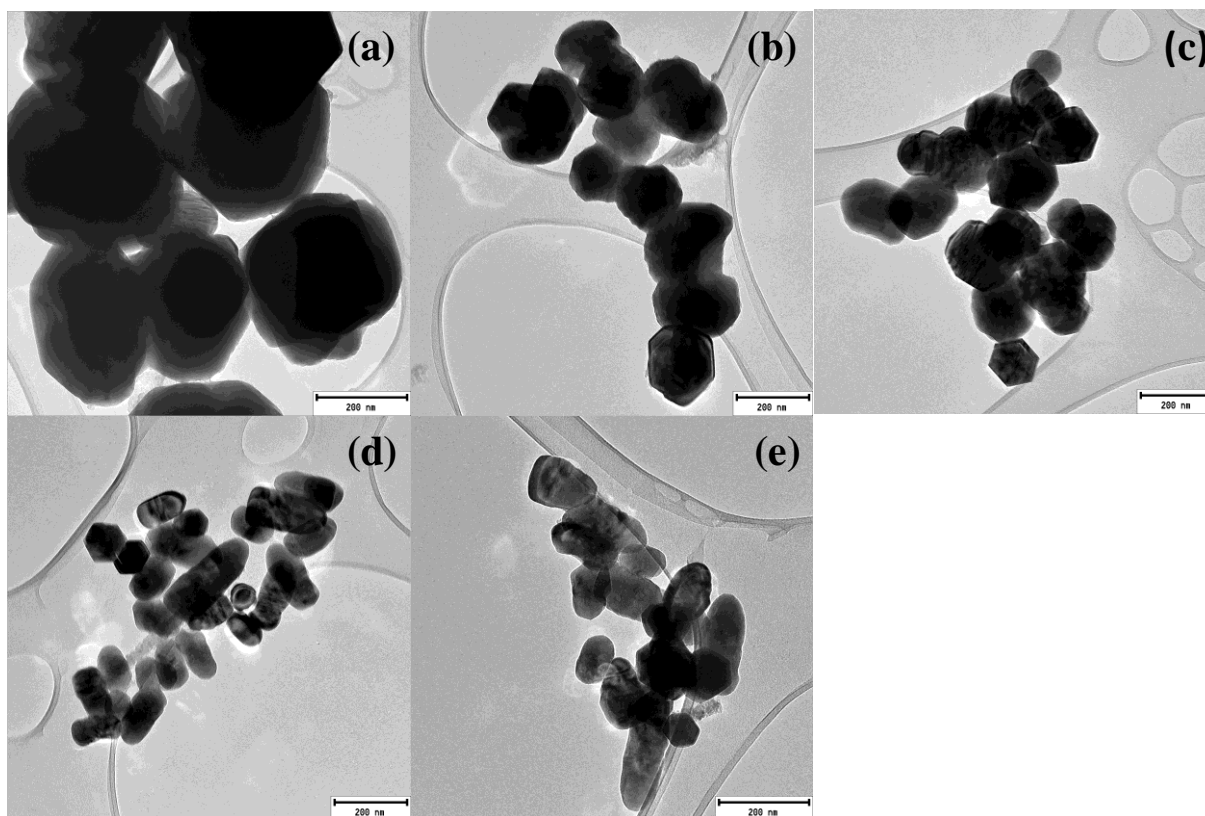


Figure 5.2: TEM micrographs of the ZnO nanoparticles synthesized for (a) 8, (b) 11, (c) 15, (d) 18, and (e) 30 min via microwave assisted heating.

The reason for this observed trend is because longer reaction time allows enough time for the precursor components to diffuse to the interface of the particles that are already growing, resulting in further growth. Also, the diffusion process is limited at fast reaction, therefore, already existing particles don't have enough time to aggregate and form larger particles [18–20]. It was observed that the naturally preferred growth of ZnO to form a rod-like morphology (i.e. growth along the c-axis) was hindered for shorter reaction times and resulted in the formation of hexagonally shaped particles. However, the growth along the c-axis was preferred when reaction was ran for longer, resulting in a bullet-like morphology. The hindrance of the growth rate along the c-axis resulted in the formation of hexagonal ZnO structures when the microwave power was set to 400, 600, 800 W at 5 min step time (30, 18 and 15 min reaction times). A slight change in the morphology, from solely hexagonal nanostructures to a mixture of hexagonal and bullet shaped nanostructures, was observed when the microwave power was set to 800 W at 1 min step

time (8 and 11 min reaction times). The reason for this change in morphology can be explained in terms of the surface energy of the initially formed crystallites and viscosity changes in the reaction mixture. It is postulated that when the heating rate is increased rapidly enough energy is supplied to the reaction mixture to allow for burst of crystal nuclei in the reaction medium [21]. As the particles begin to grow, they do so quickly such that smaller sized particles are abundant in the reaction mixture. Smaller sized particles possess high surface energy and hence will undergo self-organization that will lead to reduced surface energy via oriented attachment. The fusion of the hexagonal particles sharing a common crystallographic orientation leads to the formation of the bullet-like morphology [22, 23]. Another plausible reason is that when the temperature of the aqueous mixture increases rapidly, it causes a rapid decrease in the viscosity of the reaction medium, which in turn allows more collision of the initially formed crystallites. The decreased viscosity causes the water medium to be unstable, making it easy for the ZnO crystallites to undergo aggregation [24]. In a study done by Taung et al. [24] on the synthesis of TiO₂, they noticed through careful observation, that the diameter of the smallest nanorods was comparable to the diameter of the spherical particles [25]. This served as an indication that the formation of nanorods occurred through nucleation growth of the smaller spherical nanoparticles [25]. This observation agrees with the results in this study as it was also noted that the smallest nanobullets had a width that is comparable to diameter of the smallest hexagonal nanoparticles. It is important to note that there is a significant difference between the sizes estimated using the Scherrer's equation and TEM. This difference may be due to the fact that when using the Scherrer's equation, it calculates the size of individual crystallites, while TEM gives the size of individual grains that may have formed as a result of the particles that aggregated during growth because of the high-energy nature of nanometric crystals [26].

5.3.2 Optical properties

The UV-Vis absorption spectra of the ZnO nanoparticles are shown in Figure 5.3. The spectra display strong absorption peaks in the range 374–378 nm (3.32–3.28 eV), which are attributed to electronic transitions between the valence and conduction band characteristic of pure hexagonal ZnO phase.

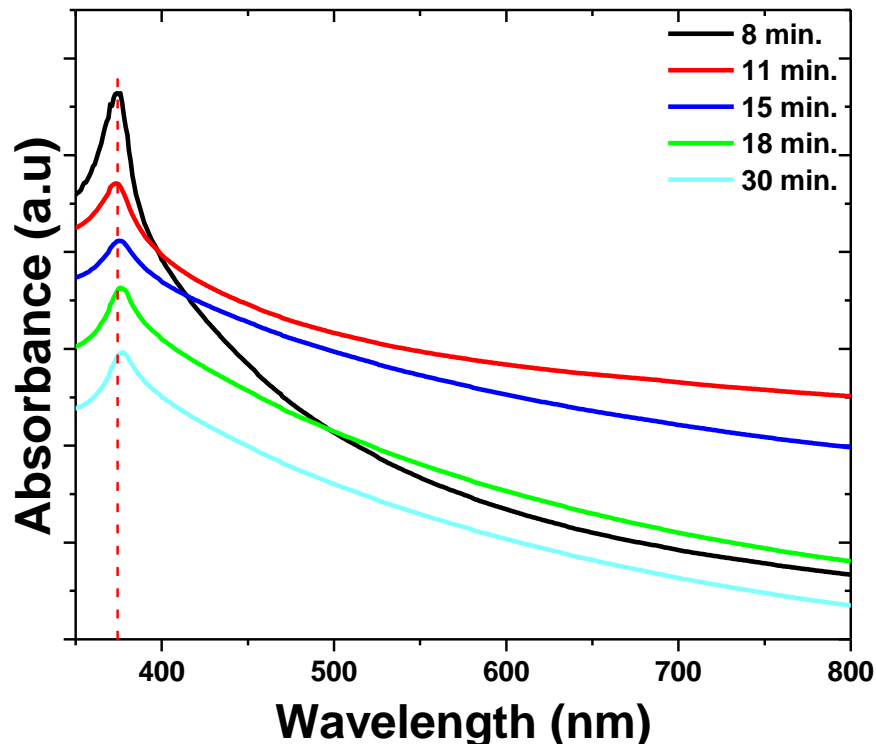


Figure 5.3: The UV-Vis absorption spectra of the as synthesized ZnO nanoparticles.

The absorption peaks in the range of 374-378 nm are slightly blue shifted from that of the exciton state in the bulk which occurs at wavelength of ~ 387 (3.33 eV) [27]. This blue shift is not too significant for the different sizes as also observed in the PL spectra. The shift to lower absorption wavelength as the size of the particles is decreased is known as quantum confinement [28]. However, this phenomenon has been mainly reported for particles with sizes that are nearly equal to the Bohr radius of the nanocrystals, which is not the case in our study whereby the smallest nanocrystals are much larger (≥ 20 nm) than the Bohr radius of ZnO (2.34 nm). This discrepancy of applying the term ‘quantum confinement’ only to quantum dots has been recently described as inaccurate and has in turn led to the introduction of regimes of quantum confinement based on the ratio between the nanocrystals (R) and the bulk exciton-radius (a_B) [28]. Under the weak regime of quantum confinement observed in this study, the changes in electronic and optical properties due to particle sizes are not as pronounced and therefore resemble those observed in bulk materials. The presence of this absorption peak alone in the spectrum support the high purity of the synthesized nanoparticles as observed in PXRD diffractograms.

Room-temperature PL spectra (Figure 5.4) of ZnO nanoparticles were obtained using an excitation wavelength of 290 nm in order to get a better understanding of the optical properties of the synthesized nanoparticles.

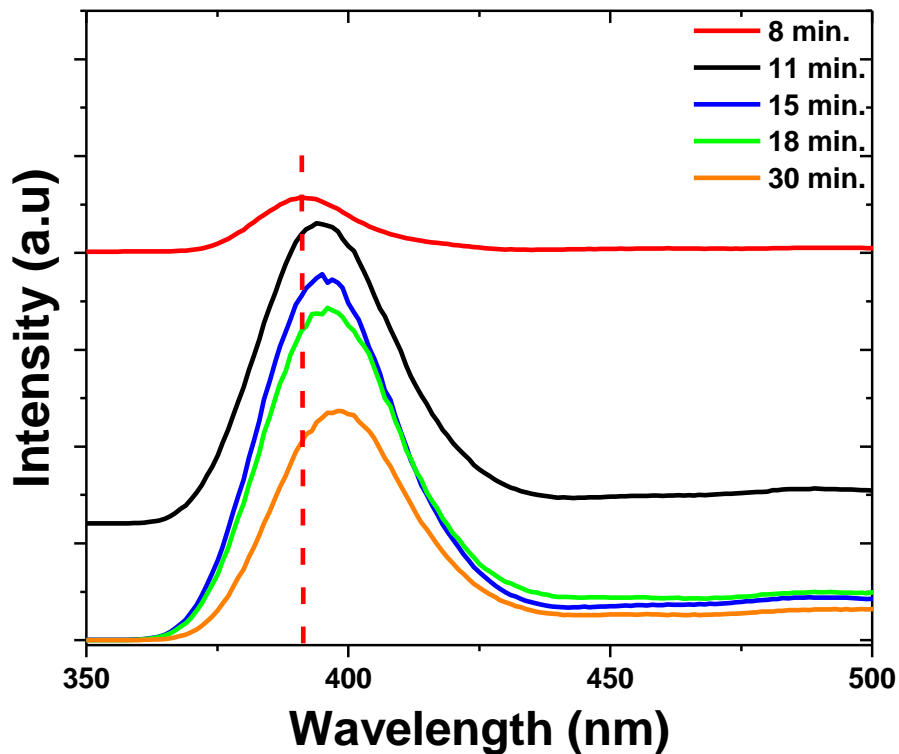


Figure 5.4: PL spectra of ZnO synthesized over 8, 11, 15, 18 and 30 min reaction time via microwave assisted synthesis.

The PL spectra of the as-synthesized ZnO nanoparticles all showed well defined broad peaks in the range of 391–398 nm that are characteristic of pure bulk ZnO. As the reaction time was reduced, the emission peak wavelength slightly moved to lower wavelength (blue shifted) as indicated by the red dotted line in Figure 5.4 (illustrating the top most position of the peaks relative to the one for the nanoparticles synthesized at 8 min). This was postulated to be due to the size differences between the nanoparticles. The broadness of the peaks (i.e. large FWHM) in the spectra speaks to the polydispersed nature of the nanoparticles.

5.4 Photocatalytic degradation studies

A typical time-dependent UV-Vis spectrum of Rhodamine B obtained during the degradation experiment conducted using the ZnO nanoparticles synthesized for 8 min is shown in Figure 5.5 (a). The absorbance of the absorption peak located at 553 nm decreased as it was being exposed to light, and diminished after 120 min which indicated that the dye molecules had been degraded. The change in concentration (i.e. absorbance) of the dye during irradiation is represented as the % degradation which was calculated as ratio of the dye concentration after certain amount of time of irradiation (C_t) to the dye concentration before irradiation multiplied by 100 ($\frac{C_t}{C_0} \times 100$ %). The time-dependent changes in the concentration of Rhodamine B solutions when they were irradiated in the presence of the ZnO nanoparticles synthesized at different reaction times (8, 11, 15, 18 and 30 min) are shown in Figure 5.5. The decrease in the concentration of the dye (% degradation) during photocatalysis using the as-synthesized ZnO was an indication that they were all photoactive.

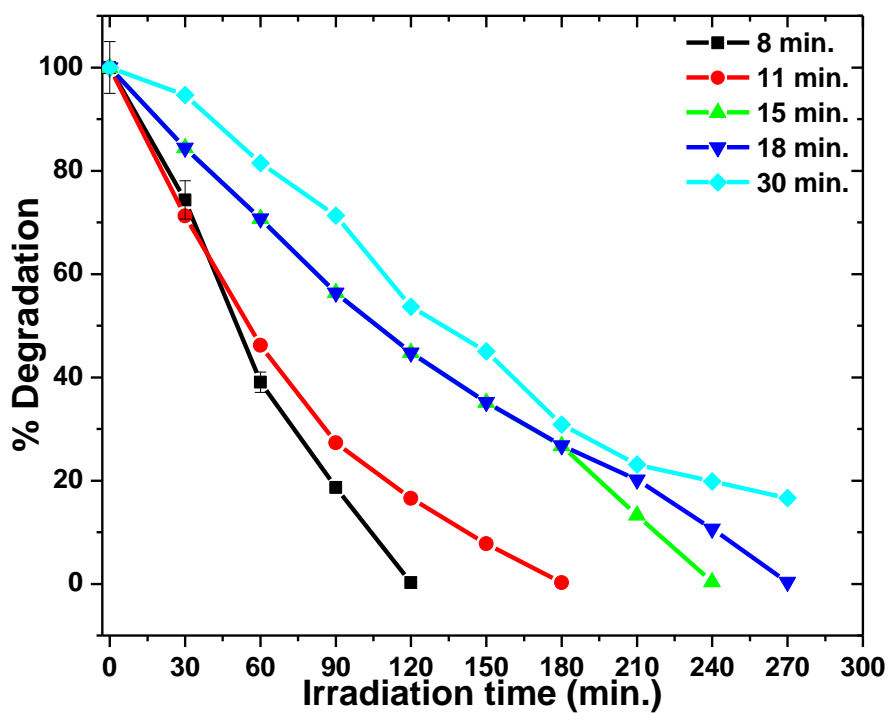
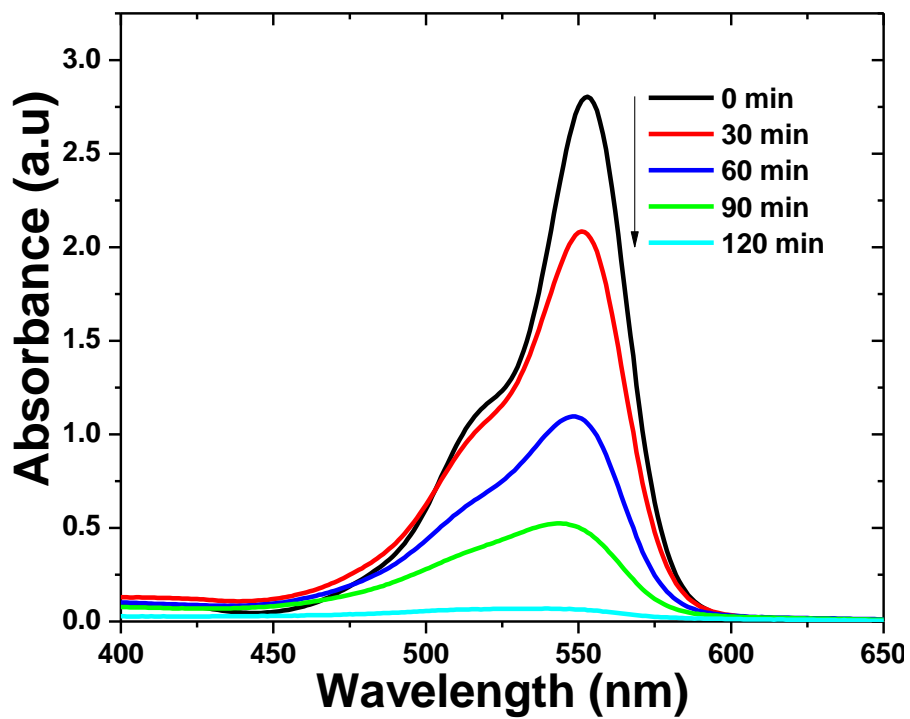


Figure 5.5: (a) UV-Vis absorption spectra changes of Rhodamine B and (b) % degradation for the photocatalysts synthesized at different reaction times.

There is a significant difference in the rate of degradation between the photocatalyst synthesized at different reaction times. It can be observed that the ZnO synthesized for short reaction times resulted in high degradation rates, while the rate of degradation significantly decreased when ZnO synthesized for long reaction time was used in the degradation of Rhodamine B. The ZnO nanoparticles synthesized at short reaction times were found to be smaller than those synthesized at longer reaction times. This observation indicated that the extent to which Rhodamine B was adsorbed and hence be degraded on the suspended ZnO photocatalyst was high when the size of the nanoparticles was small. The ZnO photocatalyst synthesized for 8, 11, 15 and 18 min achieved 100 % degradation efficiency in 2, 3, 4 and $4\frac{1}{2}$ hours, respectively. For the photocatalyst synthesized for 30 min, only 83 % degradation was achieved after $4\frac{1}{2}$ hours. The significant difference in the time that it took to completely degrade the dye can be explained in terms of the number of active sites available for dye degradation. The photocatalyst synthesized for a short period was composed of small sized nanoparticles, which can be correlated with a high surface area [29]. The high surface area meant that there were more photocatalytic active sites available for the dye molecules to bind and be degraded, which resulted in a high degradation rate. Long reaction times produced very large nanoparticles which have a smaller surface area. The limited number of exposed photocatalytic active sites for larger nanoparticles resulted in a reduced degradation efficiency [29–32]. The trend observed in this study is consistent with the work of Xu et al. [33] on their study of the effect of the particle size of TiO₂ on the degradation of methyl blue [33]. Contrary to what most researchers have found about the reduced particle size resulting to high degradation rates, Zhang et al. [34] reported a reduced rate of degradation at very small particle sizes. They have attributed this trend to the increased rate of recombination of the charge carriers due to the small distance between the electron and holes which aids recombination, but only at quantum size region [34].

The kinetic study of the photocatalytic degradation of Rhodamine B using as-synthesized ZnO was investigated with the Langmuir–Hinshelwood kinetic model, which also covers the adsorption properties of the substrate on the photocatalyst surface [35]. The equation is represented as follows:

$$Rate = \frac{dC}{dt} = k \frac{KC}{1+KC} \quad \text{eq. 5.3}$$

Where C is the concentration of Rhodamine B at the irradiation time, k the reaction rate constant, and K is the degradation coefficient of the reactant. Where k' is the apparent rate constant. A plot of ln (C0/C) versus time results in a straight line; its slope is the pseudo first- order degradation rate constant (K_{app}) [35, 36]. The experimental data obtained in the kinetic study of Rhodamine B degradation when different ZnO photocatalyst morphologies were used was fitted with the Langmuir–Hinshelwood kinetic model. The results obtained are illustrated in ANNEXURE B,

The plots of the data gave a straight line, showing that the photocatalytic degradation of Rhodamine B can be described by the pseudo-first-order kinetic model [37]. The correlation coefficient constant for the fitted line and the rate constants are graphically obtained (ANNEXURE B) and their values are represented in table 5.2.

Table 5.2: Rate constants for photocatalytic degradation of Rhodamine B using ZnO nanoparticles synthesized at different reaction times.

Reaction time	Initial concentration (ppm)	ZnO concentration (ppm)	K _{app}	R ²
8	20	160	0.069	0.908
11	20	160	0.054	0.816
15	20	160	0.053	0.766
18	20	160	0.045	0.949
30	20	160	0.030	0.769

The rate constant for the degradation of Rhodamine B using ZnO nanoparticles synthesized at different reaction times confirm that the rate at which the dye molecules were degraded was faster when the nanoparticles synthesized at short reaction time was used.

Conclusion

It was shown that ZnO nanoparticles possessing high photocatalytic activity can be prepared by using short reaction times at relatively low temperature (200 °C) using a cheap, simple and effective microwave assisted synthesis method. All the nanoparticles prepared showed a high degree of agglomeration indicating the moderate ability of urea to act as a capping agent. The size of the nanoparticles was found to be highly dependent on the reaction time. Long reaction time produced large nanoparticles with hexagonal morphology while shorter reaction times produced small particles with mixed hexagonal and bullet-like morphologies. Particle size influenced the photocatalytic activity with the smaller sized nanoparticles being more efficient in degrading Rhodamine B than the larger nanoparticles. The reason for the high catalytic activity was attributed to higher surface area.

5.5 References

- [1] C.B. Bhattacharjee, D.D. Purkayastha, S. Bhattacharjee, and A. Nath, **7**, Assam University Journal of Science and Technology, (2011) 122-127
- [2] M. Faraday, Philosophical Transactions of the Royal Society of London A, **147**, (1857) 145-181
- [3] J. Hu, T.W. Odom, and C.M. Lieber, Accounts of Chemical Resolutions, **32**, (1999) 435-445
- [4] X. Duan, Y. Huang, J. Wang, and C.M. Lieber, Nature, **401**, (2001) 66-75
- [5] H. Dai, Surface Science, **500**, (2002) 218-241
- [6] J. Zhang, L.D. Sun, H.Y. Pan, C.S. Liao, and C.H. Yan, New Journal of Chemistry, **26**, (2002) 33-41
- [7] J. Zhao, M. Li, J. Sun, L. Liu, P. Su, Q. Yang and C. Li, Chemistry – A European Journal, **18**, (2012) 3163–3168
- [8] S. Gopinath, and J. Philip, Materials Chemistry and Physics, **145**, (2014) 213-221
- [9] J. Shen, Y. Li, H. Gu, F. Xia, and X. Zuo, Chemical Reviews, **114**, (2014), 7631-7677
- [10] J. Polte, Royal Society of Chemistry, **17**, (2015), 609–683
- [11] E. Matejevic, and P. Scheiner, Journal of Colloid and Interface Science, **63**, (1978) 509-523
- [12] R.L. Penn, and J.F. Banfield, Geochimica et Cosmochimica Acta, **63**, (1999) 1549-1557
- [13] A.K. Singh, and U.T. Nakate, Advances in nanoparticles, **2**, (2009) 66-70
- [14] L. Perreux, and A. Loupy, Tetrahedron, **57**, (2001) 9199-9223
- [15] N. Thanh, N.D. Giang, L.Q. Vinh, and H.T. Dat, Communications in Physics, **24**, (2014) 153-161
- [16] D. Gultekin, M. Alaf, and H. Akbulut, Acta Physica Polonica Series a, **123**, (2013) 274-276

- [17] J. Chauhan, N. Shrivastav, A. Dugaya, and D. Pandey, *Journal of Nanomedicine and Nanotechnology*, **429**, (2017) 2157-7439
- [18] G. C. Collazzo, S. L. Jahn, N. L. V. Carreño and E. L. Foletto, *Brazilian Journal of Chemical Engineering*, **28**, (2011) 26–272
- [19] K.D. Kim, and H. Kim, *Materials Letters*, **57**, (2003) 3211–3216
- [20] J. FlorS, A.M. Lima and R. Davolos, *Surface and Colloid Science*, **128**, (2004) 239-243
- [21] G. Oskam, *Journal of Sol-Gel Science and Technology*, **37**, (2006)161–164
- [22] Y. Liu, K. Kathan, W. Saad, and R.K. Prud'homme, *Physical Review Letters*, **98**, (2007) 55-62
- [23] C.J. Dalmaschio, C. Ribeiro, and E.R. Leite, *Nanoscale*, **2**, (2010) 2336-2345
- [24] J. Polte, *CryEngComm*, **17**, (2015) 6809-6830
- [25] R. Al-Gaashania, S. Radimana, N. Tabetb, and A.R. Dauda, *Materials Chemistry and Physics*, **125**, (2011) 846–852
- [26] P.B Taunk, R. Das D.P Bisen, and R. Tamrakar, *Journal of Radiation Research and Applied Sciences*, **8**, (2015) 433-438
- [27] A. M. Pourrahimi, D. Liu, L. K. H. Pallon, R. L. Andersson, A. M. Abad, J. M. Lagar'on, M. S. Hedenqvist, V. Str'om, U. W. Geddea, and R. T. Olsson, *RSC Advances*, **4**, (2014) 35568-35577
- [28] D. Brida, E. Fortunato, I. Ferreira, H. Aguas, and R. Martins, *Journal of Non-Crystal Solids*, **299**, (2011) 1272-1276
- [29] R.U. Joep, J. H. Pijpers, E. Groeneveld, R. Kool, C. Donega, D. Vanmaekelbergh, C. Delerue, G. Allan, and M. Bonn, *NanoLetters*, **12**, (2012) 4937–4942
- [30] K.G. Chandrappa, and T.V. Venkatesha, *Nano-Micro Letters*, **4**, (2012) 14-24
- [31] A.B. Lavand, and Y.S. Malghe, *Journal of Asian Ceramic Society*, **3**, (2015) 305–310

-
- [32] O. Sheikhejad-Bishe, F. Zhao, A. Rajabtabar-Darvishi, E. Khodadad, and Y. Huang, *International Journal of Electrochemical Science*, **9**, (2014) 3068-3077
- [33] Z. Wang, C. Chen, F. Wu, B. Zou, M. Zhao, J. Wang and C. Feng, *Journal of Hazardous Materials*, **164**, (2009) 923-928
- [34] N. Xu, Z. Shi, Y. Fan, J. Dong, J. Shi, and M.Z.C. Hu, *Industrial and Engineering Chemistry Research*, **38**, (1999) 373-379
- [35] Z. Zhang, C. Wang, R. Zakaria, and J.Y. Ying, *The Journal of Physical Chemistry B*, **102**, (1998) 10871-10878
- [36] N. Barka, and Y. Ait-Ichou, *Arabian Journal of Chemistry*, **3**, (2010) 279-283
- [37] M.V. Shankar, B. Nappolian, S. Sakthivel, B. Arabindo, M. Palanichamy, and V. Murugesan, *Indian Journal of Engineering and Materials Sciences*, **8**, (2001) 104-109

CHAPTER 6: The role of zinc metal salts on size, morphology and photocatalytic activity of ZnO

6.1 Introduction

A lot of interest has risen towards ZnO in nanotechnology due to the wide range of properties that it possesses such as semiconducting, piezoelectricity, conductivity, photoactivity and ferromagnetism [1–3]. There is therefore a need to gradually produce ZnO nanostructures suitable for use in the broad range of industrial applications. Recently, ZnO has shown superior properties as a photocatalyst used in the photocatalytic degradation of dyes (e.g. methyl orange, Rhodamine B, crystal violet) in aqueous solution [4-7]. The environmental friendliness and cheapness associated with photocatalytic degradation of dyes has changed the scientific focus when it comes to solving problems such as water pollution in rivers, which go against environmental protection laws. One way that has been used to ensure that water pollution caused by dyes in rivers is effectively removed is to synthesize nanomaterials that are effective as photocatalysts. Effective photocatalysts have been previously obtained by using nanoparticles with certain morphologies and sizes, and this can be achieved by varying the way in which the nanoparticles are synthesized [8, 9]. Manipulation of the synthesis procedure has been the main focus in improving the catalytic activity of ZnO nanoparticles. Varying synthesis reaction parameters, such as using shorter reaction times to produce small nanoparticles with high quantum efficiency, and capping agents to manage the final particle morphology has led to improved activity of ZnO nanoparticles [10]. Even though reaction time and capping agents have produced the desired results before, changing the type of precursor used during synthesis has also been reported to be capable of producing nanoparticles that demonstrate superiority in the degradation of organic pollutants. Changing the type of precursor that's used doesn't only have an effect on the structural properties (i.e. size, morphology etc.) of the nanoparticles; it also affects the way in which the desired product performs in applications such as photocatalysis, gas sensing and biomedical application [11, 12]. In a study done by Mayekar et al. [13], they reported the role of the precursor in the enhancement of the antibacterial activity of ZnO, which results mainly because of the change in morphology as the precursor is varied [13]. Different

zinc metal salts ($\text{Zn}(\text{CH}_3\text{COO})_2 \cdot 2\text{H}_2\text{O}$, $\text{Zn}(\text{NO}_3)_2 \cdot 6\text{H}_2\text{O}$, ZnCl_2 and $\text{ZnSO}_4 \cdot \text{H}_2\text{O}$) are made up of different counter anions such as NO_3^- , CH_3COO^- , Cl^- and SO_4^{2-} . These different counter anions are important because their electrostatic stabilizing ability in each metal salt is different, hence it is expected that this difference will influence the sizes and morphology depending on how it interacts with the individual nuclei that form during the reaction [14]. Counter anions with a high stabilizing ability such as CH_3COO^- , have the ability to bind to growing crystal planes during a reaction, inhibiting growth. The stabilizing ability results in the formation of smaller sized nanoparticles. The counter anions such as NO_3^- which doesn't possess any stabilizing result in the formation of larger nanoparticles [14]. This study reports on the microwave synthesis of ZnO nanoparticles using different zinc metal salts in conjunction with the resulting optical (PL and UV-Vis), structural (PXRD, TEM and BET) and photocatalytic activity of the resulting nanoparticles.

6.2 Synthesis procedure

6.2.1 Chemicals and materials

Zinc acetate dihydrate ($\text{Zn}(\text{CH}_3\text{COO})_2 \cdot 2\text{H}_2\text{O}$), $\geq 98\%$, zinc nitrate hexahydrate ($\text{Zn}(\text{NO}_3)_2 \cdot 6\text{H}_2\text{O}$), $\geq 98\%$, zinc chloride (ZnCl_2), $\geq 98\%$, and zinc sulphate monohydrate ($\text{ZnSO}_4 \cdot \text{H}_2\text{O}$), $\geq 98\%$, were obtained from Sigma Aldrich. Sodium hydroxide (NaOH), $\geq 98\%$, was obtained from Glassworld and reagent grade urea ($\text{CO}(\text{NH}_2)_2$) was obtained from Promark Chemicals. Rhodamine B was obtained from MAY and BAKER LTD. A Universal 320Rsonicator ($t/\text{min} = 10$, $\text{RPM} = 7000$) was obtained from Hettich Lab Technology and a Microwave Reaction System, (Multiwave 3000 SOLV) was obtained from Anton Paar. All chemicals were used as received without any further purification.

6.2.2 Synthesis of ZnO nanoparticles using different precursors

The ZnO nanoparticles were prepared under the same experimental conditions, with only the zinc metal salt being varied. Typically, the desired zinc metal salt (i.e. $\text{Zn}(\text{CH}_3\text{COO})_2 \cdot 2\text{H}_2\text{O}$, $\text{Zn}(\text{NO}_3)_2 \cdot 6\text{H}_2\text{O}$, ZnCl_2 or $\text{ZnSO}_4 \cdot \text{H}_2\text{O}$) was dissolved in 37.5 mL deionized water in a 100 ml beaker to make a 0.1 M solution. 0.6 g of urea ($\text{CO}(\text{NH}_2)_2$) was dissolved separately in 10 ml deionized water and added to the 0.1 M precursor solution in order to aid the hydrolysis of the Zn^{2+} cations. The mixture was then adjusted to pH 10 using 0.2 M NaOH . The resulting white precipitate was vigorously stirred with the help of a magnetic stirrer for 20 min. The white precipitate was transferred into 2 vessels and hydrothermally microwaved at 800 W for 11 min, with the maximum temperature set to $200\text{ }^\circ\text{C}$ for all the samples. After completion of the reaction, it was allowed to naturally cool to room temperature and the white powder collected by centrifugation. The white powdered samples were washed several times with deionized water and ethanol to acquire maximum purity in the final products. Finally, the samples were dried at $80\text{ }^\circ\text{C}$ for 12 h in an oven. The four samples synthesized were labelled as $\text{S}_{\text{NO}_3^-}$, $\text{S}_{\text{CH}_3\text{COO}^-}$, S_{Cl^-} and $\text{S}_{\text{NO}_3^-}$ based on the type of counter anion in the zinc metal salt.

6.2.3 Characterization

For characterization (UV-Vis, TEM and PL), the ZnO nanoparticles were dissolved in ethanol and sonicated for ten min using a Digital ultrasonic cleaner (Model: PS – 20A). The optical properties were determined by Photoluminescence (PL) spectroscopy using a Varian Cary Eclipse EL04103870 fluorescence spectrophotometer and UV-Vis spectroscopy using a Varian Cary Eclipse (Cary 50) UV-Vis spectrophotometer. For visualization of the sizes and morphology of the nanoparticles, Transmission Electron Microscopy (TEM) was used and recorded using a FEI Technai T12 TEM microscope operated at an acceleration voltage of 200 kV. TEM samples were prepared by drop-casting the ethanol diluted samples on a 300 mesh copper grids. Structural properties were analysed by Powder X-ray Diffraction using a Bruker MeasSrv (D2-205530)/D2-205530 diffractometer using secondary graphite monochromated CoK α radiation ($\lambda = 1.79026\text{nm}$) at 30 kV/30 mA. Measurements were taken using a glancing angle of incidence detector at an angle of 2° , for 2θ values between $10\text{-}90^\circ$ in steps of 0.026° with a step time of 37 s and at a temperature of 25°C . The specific surface area was determined from 0.2 g using a Micromeritics TriStar 3000 instruments operated at -196°C . Before analysis, the samples were degassed at 150°C in N_2 for 3 h. The specific surface area was calculated by the BET method from N_2 adsorption data in the relative pressure range $P/P_0 = 0.05\text{-}0.30$. Total pore volumes of the samples were calculated at a relative pressure range $P/P_0 = 0.995$.

6.2.4 Photocatalytic degradation of Rhodamine B

The dye degradation experiments were conducted by preparing 100 ml solution of Rhodamine B with the desired concentration of 20 ppm in a 200 ml beaker and mixed with a known concentration (160 ppm) of the zinc oxide photocatalyst. The dye-photocatalyst mixture was sonicated for 30 min in the dark in order to ensure that the zinc oxide nanoparticles were well dispersed in the solution. At the end of sonication the mixture was subsequently stirred for 60 min using a magnetic stirrer and a stirrer bar in order to allow for equilibration between the dye molecules and the photocatalyst. Before the mixture was exposed to solar radiation, an aliquot was withdrawn and its absorbance measured, and that aliquot was labelled as ‘time zero,’ which meant before exposure to light. The progress of degradation was monitored using the following equation:

$$\frac{C_t}{C_0} \times 100\% \quad \text{eq. (6.1)}$$

Where C_t refers to the concentration of the dye after a certain time of irradiation and C_0 refers to the concentration of the dye before irradiation. The light was then switched on and constantly irradiated on the mixture that was continuously stirred. Aliquots were then subsequently withdrawn at 30 min intervals and their absorbance determined. Each aliquot (4mL) was collected using a 10 mL syringe fitted with a 0.2 μm syringe filter. The syringe filter was used to ensure that no residual ZnO nanoparticles were in the aliquot during the analysis of the dye solution. In this study, four photocatalytic degradation experiments were done to compare the activity of the different ZnO nanoparticles prepared using the different zinc metal salts. The pH of the dye solution was measured using a Starter 3100 pH Bench.

6.3 Results and Discussion

6.3.1 Structural properties

Figure 6.1 displays the PXRD patterns of the ZnO nanoparticles synthesized using microwave assisted heating method for 11 min. The diffraction data of the nanoparticles synthesized using $\text{Zn}(\text{NO}_3)_2 \cdot 6\text{H}_2\text{O}$ ($\text{S}_{\text{NO}_3^-}$), $\text{Zn}(\text{CH}_3\text{COO})_2 \cdot 2\text{H}_2\text{O}$ ($\text{S}_{\text{CH}_3\text{COO}^-}$) and ZnCl_2 (S_{Cl^-}) were well indexed to the zincite (syn) structure of ZnO with the lattice constants $a = 3.249 \text{ \AA}$ and $c = 5.199 \text{ \AA}$, space group $\text{P6}_3\text{mc}$, which was in good agreement with the standard card (JCPDS – 00-005-0664) [15]. The diffraction data of the nanoparticles synthesized using $\text{ZnSO}_4 \cdot \text{H}_2\text{O}$ ($\text{S}_{\text{SO}_4^{2-}}$) was indexed to the hexagonal wurzite structure of ZnO with the lattice constants $a = 5.249 \text{ \AA}$ and $c = 5.207 \text{ \AA}$, space group $\text{P6}_3\text{mc}$, which was in good agreement with the standard card (JCPDS – 01-089-0511) [16].

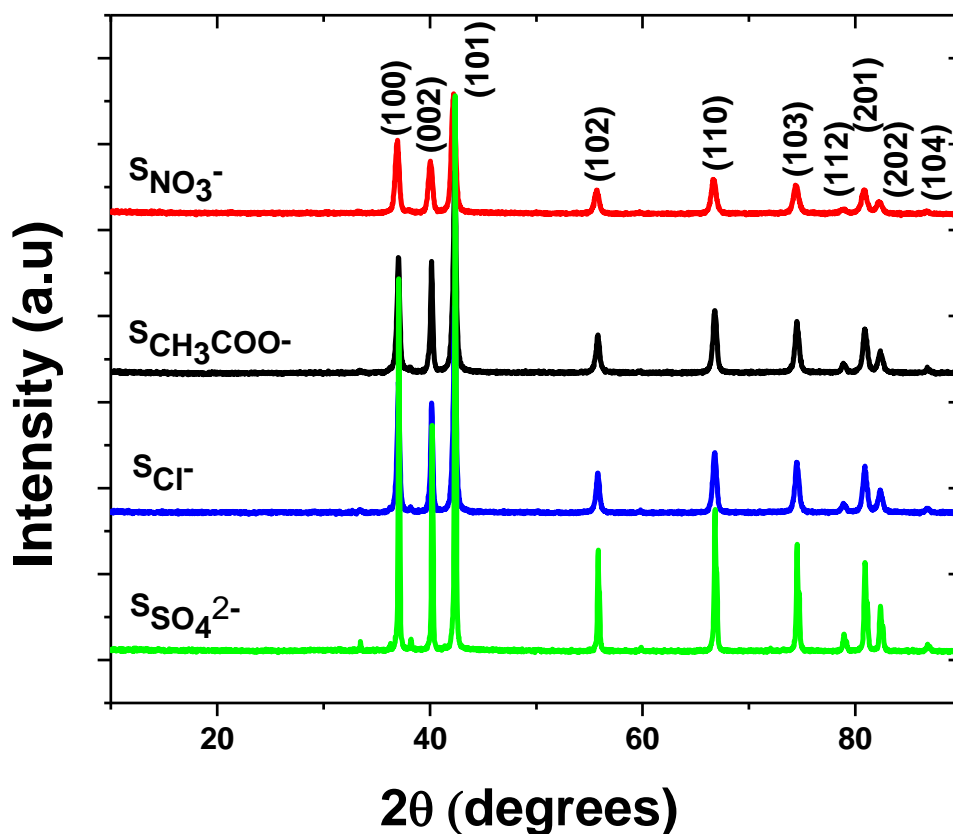


Figure 6.1: PXRD of ZnO nanoparticles synthesized using different zinc metal salt precursors.

The good crystallinity of the synthesized ZnO nanoparticles was confirmed by the sharpness and the high intensity of the peaks. No peaks were correlated to any other phase, which indicated that the nanoparticles synthesized were free of any impurities. The high intensity of the (101) peak in all the diffractograms indicated that the synthesized nanoparticles had a preferred growth direction being the c-axis. This preferred growth direction is particularly prominent for $S_{SO_4^{2-}}$ which is supported by its morphology that is elongated in one direction (Figure 6.2) [17]. The intensity of the (101) plane for the $S_{NO_3^-}$ is the lowest of all the nanoparticles, which might be an indication of the high proportion of spherical morphology which indicated dominant isotropic growth over anisotropic growth.

To estimate the size of the crystallites, the Debye-Scherrer's equation was used (eq. 6.2) [18].

$$D = 0.9\lambda/\beta\cos\theta \quad \text{eq. (6.2)}$$

Where D is the crystallite size, λ the wavelength of Co K_α radiation (0.179026 nm), β the full-width half maximum (FWHM) of the most intense peak (101 plane) in the diffraction pattern, θ is the angle that is obtained from the 2θ corresponding to the (101) plane (maximum intensity peak) in radians. The different sizes of the crystallites for the ZnO nanoparticles synthesized using different zinc metal salts are shown in Table 6.1.

Table 6.1: Full-width half maximum and relative crystallite sizes of the ZnO nanoparticles.

Sample names	θ (radians)	FWHM (10^{-3}) (radians)	Crystallite size (nm)
$S_{NO_3^-}$	0.371	8.43	20.5
$S_{CH_3COO^-}$	0.371	6.55	24.6
S_{Cl^-}	0.371	6.07	26.5
$S_{SO_4^{2-}}$	0.372	3.15	54.9

It is known that there is an inversely proportional relationship between the width of the peak (FWHM) and the size of the crystallites. Represented in Table 6.1 are the results that show that as the peaks in the diffractogram gets broader (i.e. large FWHM), the size of the crystallites become smaller. This difference in the sizes of the crystallites was also confirmed by the shift of the emission peaks to lower wavelength (i.e. higher energy) in the PL spectra shown in Figure 6.4. A similar trend was observed by Sheikhnejad-Bishe et al. [19], in their study of reaction time on the photocatalytic properties of TiO₂ [19].

Shown in Figure 6.2(a-d) are the electron micrographs of the ZnO nanoparticles synthesized using different zinc metal salts. The micrographs clearly show that changing the type of precursor used during synthesis has an influence on the size and morphology of the nanoparticles.

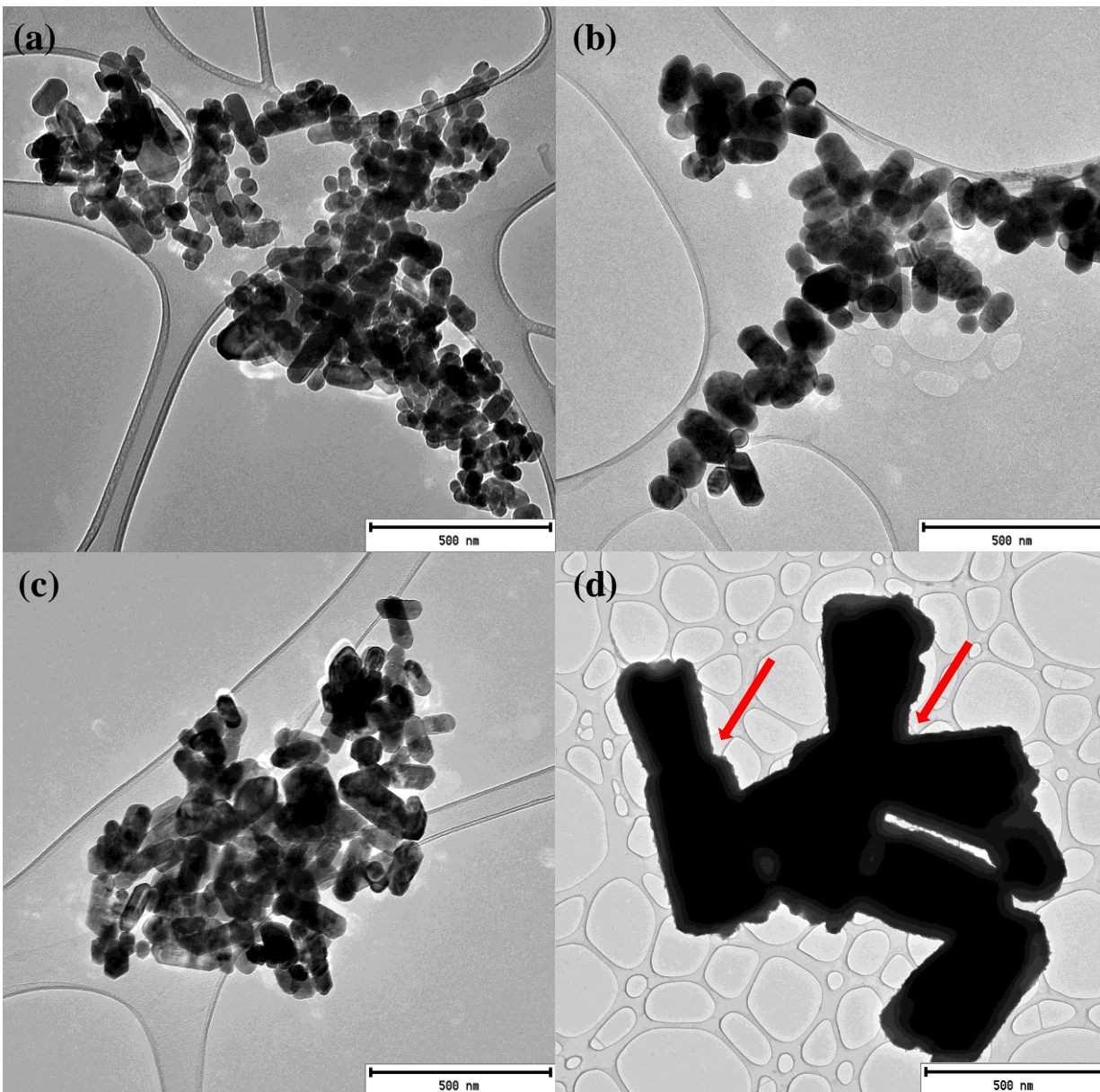


Figure 6.2: TEM micrographs of ZnO synthesized using (a) $S_{NO_3^-}$, (b) $S_{CH_3COO^-}$, (c) S_{Cl^-} , and (d) $S_{SO_4^{2-}}$ zinc metal salts. (Red arrows – Oriented attachment)

The micrographs for the $S_{NO_3^-}$, $S_{CH_3COO^-}$ and S_{Cl^-} samples are made up of a mixture of spherical and rod-like nanoparticles, with varying proportions of the spherical and rod-like morphology. The $S_{NO_3^-}$ sample is composed mainly of small spherical nanoparticles with an average diameter of 40nm; the rod-like nanoparticles have an average width of 50 nm and length of 128 nm.

Poly dispersity and agglomeration in the $S_{\text{CH}_3\text{COO}^-}$ nanoparticles was observed, similarly to what was observed in the $S_{\text{NO}_3^-}$ nanoparticles. The $S_{\text{CH}_3\text{COO}^-}$ sample is composed mainly of the rod-like nanoparticles with a much larger width of 67 nm, length of 118 nm, which was shorter than that of $S_{\text{NO}_3^-}$. The spherical nanoparticles had an average diameter of 65 nm. In the S_{Cl^-} photocatalyst, it was observed that the morphology took on a predominantly rod-like morphology of varying sizes with only a handful of spherical particles observed. The spherical nanoparticles had an average diameter of 65 nm, and the rod-like nanoparticles were found to have an average width of 78 nm and length of 189 nm. For the $S_{\text{NO}_3^-}$, $S_{\text{CH}_3\text{COO}^-}$ and S_{Cl^-} nanoparticles, it could be noted that there was an increase with regards to the type of dominant morphology, the $S_{\text{NO}_3^-}$ photocatalyst favoured the formation of more spherical particles and this preferred growth direction seem to change as the counter anion is changed to either Cl^- and CH_3COO^- . It can therefore be concluded that the formation of more rod-like nanoparticles occurs with the change of the counter anion in the order $\text{Cl}^- > \text{CH}_3\text{COO}^- > \text{NO}_3^-$. A significant change in the morphology was observed for the $S_{\text{SO}_4^{2-}}$ sample, which adopted a trapezium-shaped morphology in which the particles are linked together through self-oriented assembly as indicated by the arrow in Figure 6.2(d). Figure 6.3 depicts the proposed mechanism for the formation of self-oriented trapezium shaped ZnO nanoparticles. Self-oriented assembly occurs when there are specific interactions among particles that result in particle aggregation as shown in [20].

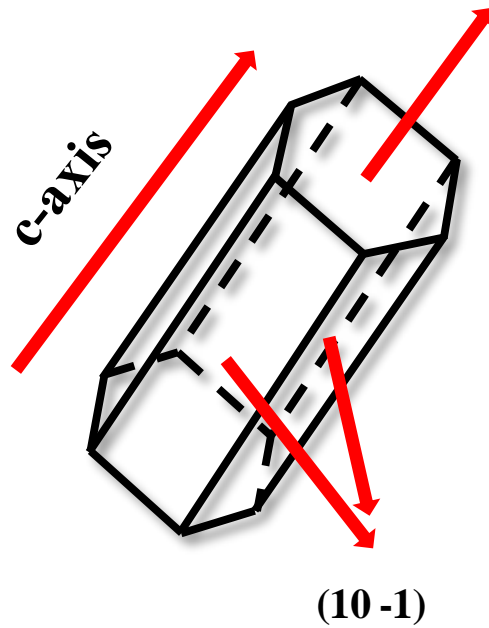


Figure 6.3: Proposed mechanism through which ZnO nanoparticles undergo oriented attachment.

The formation of the spherical and rod-like nanoparticles in this study can be explained by considering the crystal structure of ZnO. ZnO is designed such that in the hexagonal form, the crystals are made up of both [0001] polar facets and [10-1] non-polar facets, which are parallel to the c-axis as shown in Figure 6.4(a-b). Axial growth (Figure 6.4(a)) is observed when the [0001] polar facets are more favoured for growth resulting to rod like morphology, whereas hexagonal

morphology dominates when equatorial growth (Figure 6.4(b)) along the (10-1) non-polar facets is favoured.

(a) (001) – Axial growth



(b)

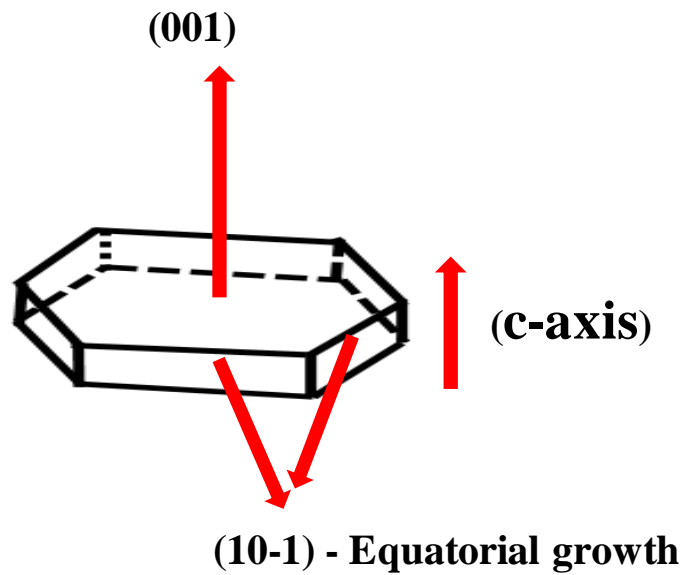


Figure 6.4: ZnO crystal showing the axial and equatorial face specific growth which formed (a) rod- and (b) hexagonal nanoparticles, respectively.

The polar Surfaces have a very high surface energy ($\gamma^0(0001\text{-Zn}) = 2.49 \pm 0.0063$, $\gamma^0(000\text{-1-O}) = 1.35 \pm 0.0063$), which makes them thermodynamically unstable compared to the non-polar facets [21-23]. This means that the growth rate of ZnO along the c-axis is enhanced during crystal growth in a reaction medium. In the $S_{\text{NO}_3^-}$ photocatalyst, the dominant morphology observed is the spherical nanoparticles which results due to an enhanced growth rate along the non-polar facets. This enhanced growth rate along the non-polar facets could be due to the presence of excess NO_3^- ions in the solution, which binds to the [0001] growth plane, reducing access of the precursor components to this plane resulting in the formation of more spherical nanoparticles. In the case of the $S_{\text{CH}_3\text{COO}^-}$, S_{Cl^-} and $S_{\text{SO}_4^{2-}}$ nanoparticles, it was proposed that the formation of more elongated nanoparticles was due to the Cl^- , CH_3COO^- and SO_4^{2-} counter anions inability to inhibit the fast growth along the (0001) plane. In order to get a better understand of the size differences that results when different zinc metal salts are used to synthesize zinc oxide, BET method was used to determine the specific surface area, pore volume and pore diameter and the results are shown in Table 6.2.

Table 6.2: BET results of the synthesized ZnO nanoparticles

Sample	Surface area ($\text{m}^2 \cdot \text{g}^{-1}$)	Pore width (nm)	Pore volume ($\text{cm}^3 \cdot \text{g}^{-1}$)
$S_{\text{NO}_3^-}$	13.25	41.53234	0.139084
$S_{\text{CH}_3\text{COO}^-}$	12.34	42.37589	0.135425
S_{Cl^-}	12.02	44.04713	0.134994
$S_{\text{SO}_4^{2-}}$	1.24	19.01317	0.005899

From the experimental results, it can be noted that the surface area is largely affected by the change in precursor. An inversely proportional relationship between the particle size and surface area is known to exist, and states that as the size of the particles decrease, the surface area increases. Using this relationship together with the estimated particle size estimated from TEM, it can be said that the size of the ZnO synthesized using different precursors increase in the order $S_{\text{NO}_3^-} > S_{\text{CH}_3\text{COO}^-} > S_{\text{Cl}^-} > S_{\text{SO}_4^{2-}}$, which is in good agreement with the reported surface area measurements. Using different zinc metal salts which contain different counter anions has been studied in the synthesis of ZnO due to the belief that it will result in different nucleation and growth kinetics [24-26]. The different nucleation and growth kinetics tend to influence the morphology, size, photoluminescence and crystallographic properties of the resulting nanoparticles. In the study done by W. Tang [27], where three different precursors were used to prepare zinc oxide, they found that changing the zinc metal salts resulted in rod-like, rice-like and granular like morphologies when $\text{Zn}(\text{NO}_3)_2 \cdot 6\text{H}_2\text{O}$, ZnCl_2 and $\text{Zn}(\text{CH}_3\text{COO})_2 \cdot 2\text{H}_2\text{O}$ were used, respectively. The different nanoparticles showed different activity in the degradation of Methyl Orange, which was attributed to surface area differences with the degradation rate increasing in the order granular-like > rice-like > rod-like [27].

In another study done by Pourrahimi et al. [28], they reported that the counter anion, which has the strong ability to stabilize nuclei during growth, will produce particles that are more mono dispersed than those with a counter anion with no coordinating ability. In their study, they found that the zinc metal salt containing the CH_3COO^- counter anion produced smaller sized particles since it is capable of coordinating either with the uni- or bidentate oxygen to the nuclei composed of positively charged zinc atoms. The absence of coordinating functional groups in the NO_3^- , Cl^- and SO_4^{2-} meant that there was no stabilization of the zinc atoms which allowed for extensive fusion during growth resulting too much larger particles [28]. Apart from the stabilizing ability of the counter anion, it is reported that the morphology and growth rate might also be influenced by how the Na^+ cation from NaOH (i.e. precipitating agent used during synthesis) interact with the different counter anions [28]. The trend reported by Pourrahimi et al. [29] is different from our observation where we found that the zinc metal salt containing the NO_3^- counter anion produced smaller sized particles than the precursor composed of the CH_3COO^- counter anion. This difference could be due the type of synthesis method used as they used a reactor vessel for synthesis and we used microwave assisted heating in our study. It is

important to note that there is a significant difference between the sizes estimated using the Scherrer's equation and TEM. This difference may be due to the fact that when using the Scherrer's equation, it calculates the size of individual crystallites, while TEM gives the size of individual grains that may have formed as a result of the particles that aggregated during growth because of the high-energy nature of nanometric crystals [29].

The minimum amount of energy that is needed to transfer an electron from the Highest Occupied Molecular Level (HOMO) to the Lowest Unoccupied Molecular Orbital (LUMO) is known as the band gap energy and can be determined using UV-Vis spectroscopy [30]. Determining the band gap of a material is important because it provides information about the type of material being dealt with (i.e. insulator, semiconductor or metal). Figure 6.5 display the different absorption spectra of the ZnO nanoparticles synthesized using zinc metal salts made up of different counter anions (NO_3^- , CH_3COO^- , Cl^- , and SO_4^{2-}).

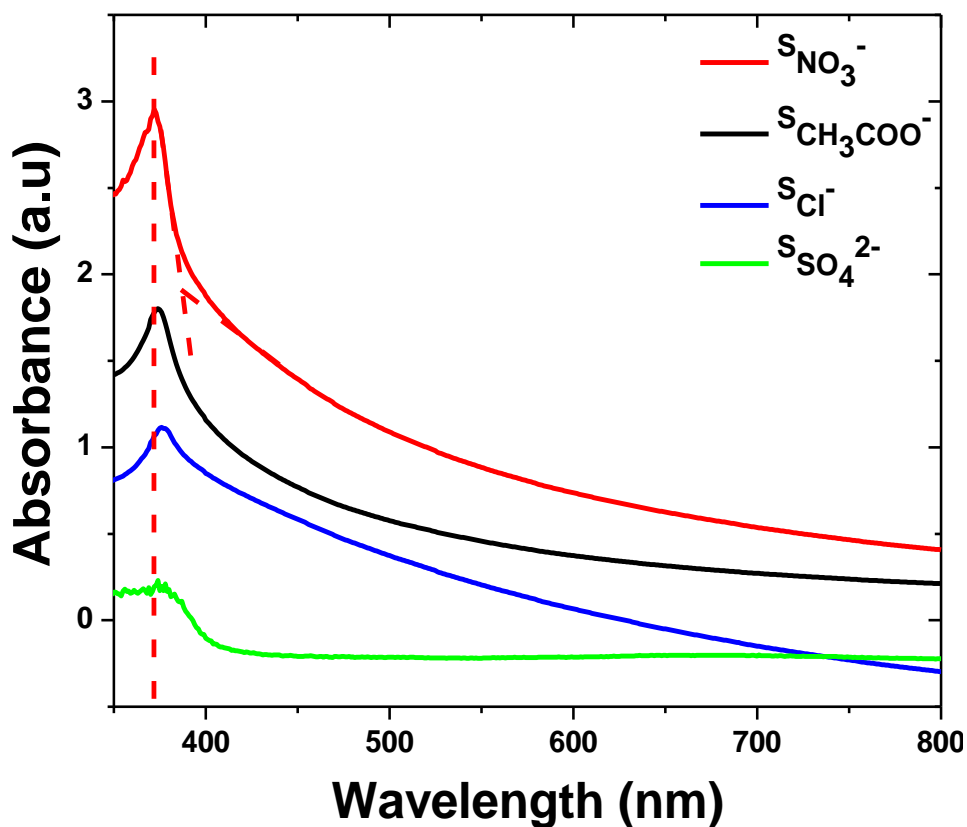


Figure 6.5: Absorption spectra of ZnO nanoparticles synthesized under the same experimental conditions varying only the zinc metal salts.

The different ZnO nanoparticles display the maximum absorption peaks in the range 372–385 nm. The polydispersed nature of the $S_{NO_3^-}$, $S_{CH_3COO^-}$ and S_{Cl^-} ZnO nanoparticles is responsible for the tailing of their respective UV-Vis spectra. This polydispersed nature is in agreement with the different morphologies and sizes depicted in TEM micrographs (Figure 6.2(a–c)). This tailing is however not prominent in the spectra of the $S_{SO_4^{2-}}$ photocatalyst. This is expected since the nanoparticles for this photocatalyst are composed of only trapezium shaped morphology with a very narrow size distribution.

Figure 6.6 depicts room temperature emission spectra of the ZnO nanoparticles that were run using an excitation wavelength of 290 nm. The UV-range ($\lambda < 400$ nm) in which the nanoparticles show a strong emission peak (UV near band edge) is apparent. The broadness of the peaks in the spectra is indicative of the polydispersed nature of the nanoparticles as observed in TEM micrographs, which shows the mixture of morphologies and sizes in the different nanoparticles prepared.

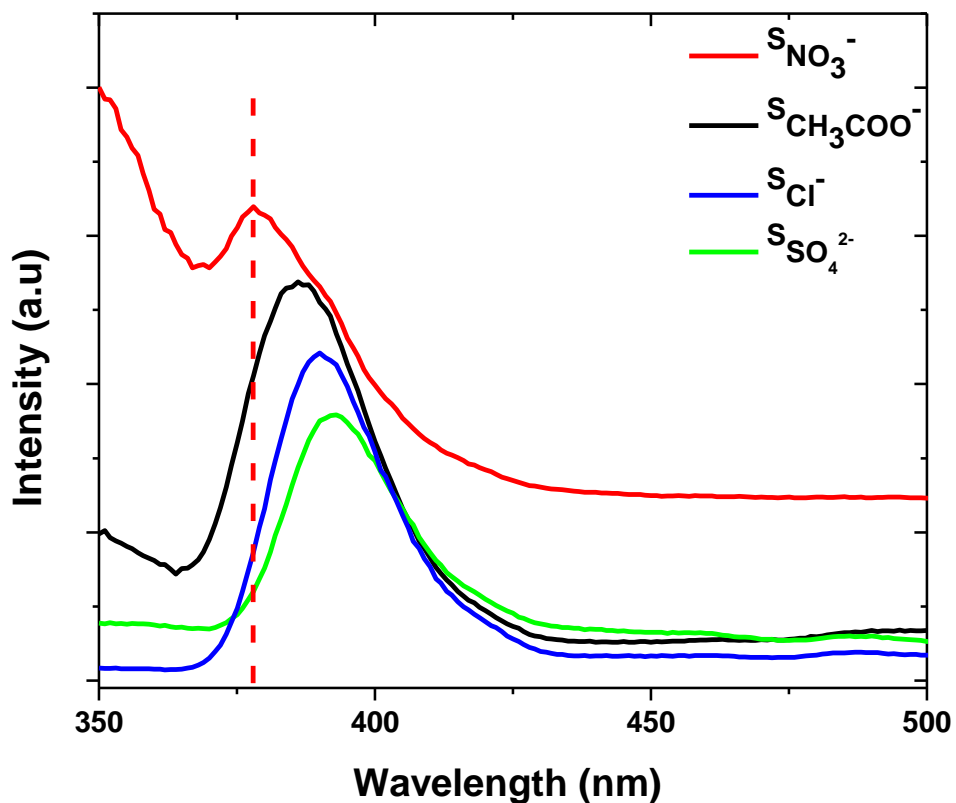


Figure 6.6: Room temperature emission spectra of ZnO synthesized using different zinc metal salts.

The spectra shows a slight shift to higher energy (i.e. lower wavelength) as the precursors are changed with the order of $S_{NO_3^-} > S_{CH_3COO^-} > S_{Cl^-} > S_{SO_4^{2-}}$, in terms of increasing emission energy. This shift to lower wavelength is beneficial in nanoparticles with a wide band gap such as ZnO as it allows for absorption of the UV light from the sun which is needed for photoexcitation in wide band gap nanoparticles. The correlation between the emission wavelength and efficiency of a photocatalyst was observed in the photocatalytic study (Figure 6.7) where the $S_{NO_3^-}$ photocatalyst was more efficient than the other nanoparticles ($S_{CH_3COO^-}$, S_{Cl^-} , and $S_{SO_4^{2-}}$) which have an emission peak at slightly higher wavelength relative to it. In the work of Moore et al. [31], where they studied the effect of particle size on the photocatalytic activity, they reported that the blue shift of the emission wavelength was due to size differences of the ZnO nanoparticles that cause a phenomenon known as quantum size effect or quantum confinement [31]. This effect emerges when the size of the nanoparticles is so small to such an extent that it's

comparable to the Bohr radius of the charge carrier (i.e. ZnO) resulting to changes in its optical properties relative to those observed in bulk material[31, 32].

6.4 Photocatalytic degradation of Rhodamine B

In order to study the activity of $S_{NO_3^-}$, $S_{CH_3COO^-}$, S_{Cl^-} and $S_{SO_4^{2-}}$ nanoparticles, photocatalytic degradation studies were conducted by running the degradation experiments under the same experimental conditions ($[ZnO] = 160$ ppm, $[Dye] = 20$ ppm, $pH = 6.8$ (natural water)), with only the type of nanoparticles being varied. Figure 6.7(a-d) displays typical time-dependent UV-Vis spectra of the Rhodamine B solutions obtained during the photocatalytic degradation process together with % degradation versus irradiation time plot (Figure 6.7 (e)) showing the amount of the dye degraded in every 30 min interval for the different nanoparticles.

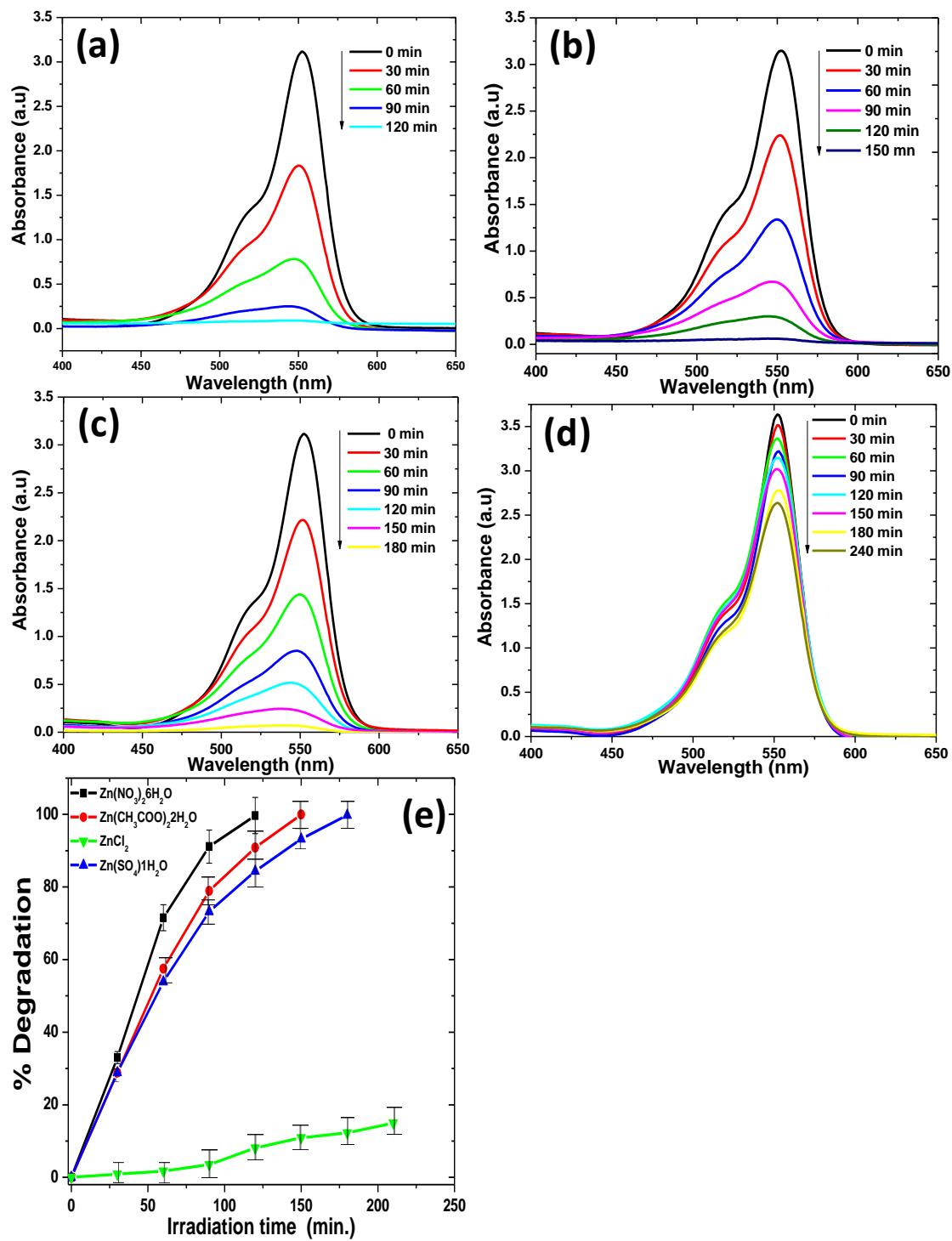


Figure 6.7: UV-Vis spectral changes of Rhodamine B during the course of degradation using (a) SNO_3^- , (b) SCH_3COO^- , (c) SCl^- , and (d) SSO_4^{2-} nanoparticles.

For the $S_{NO_3^-}$ photocatalyst, the absorbance of the peak located at wavelength 553 nm was decreased by 71 % after being irradiated for 60 min, after 120 min of being exposed to solar light, the absorbance decreased to zero, showing 100 % degradation of the dye Figure 6.7(a). Using $S_{CH_3COO^-}$, S_{Cl^-} and $S_{SO_4^{2-}}$ nanoparticles, 57 %, 54 %, 2 % of the dye was degraded after 60 min of exposure to light, respectively. Complete degradation was observed after 150 and 180 min for the $S_{CH_3COO^-}$ and S_{Cl^-} nanoparticles. The $S_{SO_4^{2-}}$ photocatalyst managed to degrade only 15 % of the dye after 210 min, making it the less effective in the four nanoparticles synthesized in this study. The difference in the degradation efficiency of the different nanoparticles tested in our study is easy to understand based on the surface area measurements as shown in Table 6.2. The surface area of the nanoparticles follows the order $S_{NO_3^-} > S_{CH_3COO^-} > S_{Cl^-} > S_{SO_4^{2-}}$. The correlation between the rate of degradation and surface area is apparent, showing that as the surface area increase, the rate of degradation increase. Hence the $S_{NO_3^-}$ catalyst with the highest surface area achieved complete degradation in the shortest time (120 min) compared to the other photocatalyst as shown in Figure 6.7(e). Since the oxidation/reduction reactions that results to the degradation of the dye occurs at the surface of the catalyst, it is expected that the high surface area provides more photocatalytic active sites which are available for the dye molecules to bind and be degraded resulting to a high degradation rate [33, 34]. In a study done by Tang et al. [27], looking at the degradation of methyl orange using ZnO (rod-like, granular and rice-like) synthesized using different metal salts, they found the rod-like morphology to be the less effective as opposed to the granular and rice morphologies. Low surface area was described to be the reason for the low activity, which is in good agreement with the results of this study where the morphology showed significant anisotropic growth (i.e. trapezium shaped) having low degradation efficiency. Surface area is an important factor that controls the efficiency of a photocatalyst but other factors, such as the proportion of certain crystallographic facets exposed in a photocatalyst also play a role. In the study conducted by McLaren et al. [35], they reported that hexagonal plate like particles were more active in degrading methylene blue than rod-shaped particles. They attributed the difference in activity to be due to the terminal [0001] and [000-1] facets being more active than the [100] and [101] facets which are perpendicular to them [36]. In this study, we can assume that since the $S_{NO_3^-}$ photocatalyst contained more spherical particles than the other nanoparticles, the polar facets exposed in this photocatalyst were abundant as opposed to the others and hence the high activity. The absence of any spherical particles in the

$S_{SO_4^{2-}}$ (i.e. trapezium shaped) meant only a smaller proportion of the polar surfaces were exposed and this contributed to the small activity of this photocatalyst.

The kinetic study of the photocatalytic degradation of Rhodamine B using as-synthesized ZnO was investigated with the Langmuir–Hinshelwood kinetic model, which also covers the adsorption properties of the substrate on the photocatalyst surface [36]. The equation is represented as follows:

$$Rate = \frac{dC}{dt} = k \frac{KC}{1+KC} \quad \text{eq. 6.6}$$

Where C is the concentration of Rhodamine B at the irradiation time, k the reaction rate constant, and K is the degradation coefficient of the reactant. Where k' is the apparent rate constant. A plot of $\ln(C_0/C)$ versus time results in a straight line; its slope is the pseudo first- order degradation rate constant (K_{app}) [36, 37]. The experimental data obtained in the kinetic study of Rhodamine B degradation when different ZnO photocatalyst morphologies were used was fitted with the Langmuir–Hinshelwood kinetic model. The results obtained are illustrated in APPENDIX C.

The plots of the data gave a straight line, showing that the photocatalytic degradation of Rhodamine B can be described by the pseudo-first-order kinetic model [38]. The correlation coefficient constant for the fitted line and the rate constants are graphically obtained (APPENDIX C) and their values are represented in table 6.1.

Table 6.2: Rate constants for photocatalytic degradation of Rhodamine B using ZnO nanoparticles synthesized from different zinc metal salts.

Reaction time	Initial concentration (ppm)	ZnO concentration (ppm)	K_{app}	R^2
$S_{NO_3^-}$	20	160	0.024	0.948
$S_{CH_3COO^-}$	20	160	0.023	0.975
S_{Cl^-}	20	160	0.020	0.952
$S_{SO_4^{2-}}$	20	160	0.000	0.983

The rate constant for the degradation of Rhodamine B using ZnO nanoparticles synthesized from different precursors confirm that the rate at which the dye molecules were degraded was faster when the nanoparticles synthesized using zinc nitrate hexahydrate was used.

6.5 Conclusion

The synthesis of ZnO using different zinc metal salts via microwave assisted digestion was successfully conducted. The nanoparticles took on rod-like and pseudo-spherical morphologies when the $\text{ZnO}_2 \cdot 6\text{H}_2\text{O}$, $(\text{Zn}(\text{CH}_3\text{COO})_2 \cdot 2\text{H}_2\text{O})$ and ZnCl_2 precursors were used, with the proportion of the NO_3^- spherical morphology in each photocatalyst varying in the order $\text{Zn}(\text{NO}_3)_2 \cdot 6\text{H}_2\text{O} > \text{Zn}(\text{CH}_3\text{COO})_2 \cdot 2\text{H}_2\text{O} > \text{ZnCl}_2$. The $\text{ZnSO}_4 \cdot \text{H}_2\text{O}$ precursor yielded trapezium shaped particles dominated by characteristic self-oriented assembly. In all the nanoparticles, significant amount of agglomeration was observed, indicating the inability of the urea to keep the individual grains apart. The crystallite sizes determined using the Scherrer's equation was found to be 20.5, 24.6, 26.5 and 54.9 nm for the $\text{S}_{\text{NO}_3^-}$, $\text{S}_{\text{CH}_3\text{COO}^-}$, S_{Cl^-} and $\text{S}_{\text{SO}_4^{2-}}$ nanoparticles, respectively. During photocatalytic degradation studies, the fastest degradation was achieved using the $\text{S}_{\text{NO}_3^-}$ photocatalyst, which degraded the dye in a period of 120 min, followed by $\text{S}_{\text{CH}_3\text{COO}^-}$ at 150 min, S_{Cl^-} at 180 min and $\text{S}_{\text{SO}_4^{2-}}$ managing to degrade only 15 % of the dye after 240 min. The difference in the activity was attributed to surface area differences, which followed the order $\text{S}_{\text{NO}_3^-} > \text{S}_{\text{CH}_3\text{COO}^-} > \text{S}_{\text{Cl}^-} > \text{S}_{\text{SO}_4^{2-}}$, with the photocatalyst that had the highest surface area showing high degradation rates. The large number of spherical particles in the $\text{S}_{\text{NO}_3^-}$ photocatalyst was also raised as a factor that was responsible for the high activity due to it having a high proportion of the high energy [0001] and [000-1] facets known to be highly active.

6.6 References

- [1] A. Moezzi, A.M. Mcdonagh, and M.B Cortie, *Chemical Engineering Journal*, **185-186**, (2012) 1-22
- [2] A. Kolodziejczak-Radzimska, and T. Jesionowski, *Materials*, **7(4)**, (2014) 2833–2881
- [3] K.M. Lee, C.W. Lai, K.S. Ngai, and J.C. Juan, *Water Research*,**88**, (2016) 428 - 448
- [4] N. Yusoff, L. Ho, S. Ong, Y. Wong, and W. Khalik, *Desalination and Water Chemistry Treatment*, **57**, (2016) 27
- [5] S. Baruah, M Jaisai, R. Imani, M.M. Nazhad and J. Dutta, *Science and Technology of Advanced Materials*, **10**, (2010) 5
- [6] P. Sutradhar, and M. Saha, *Journal of Experimental Nanoscience*, **11**, (2015) 314-327
- [7] M.A. Behnajady, N. Modirshahla, M. Shorki, A. Zeininezhad, and H.A. Zamani, *Journal of Environmental Science and Health, Part A*, **44**, (2009) 7
- [8] T. Sun, J. Qiu, and C. Liang, *Journal of Physical Chemistry*, **112**, (2008) 715-721
- [9] M. Farbon, and E. Jafarpour, *Material letters*, **85**, (2012) 47–49
- [10] C.M. Phan and H. M. Nguyen, *Journal of Physical Chemistry A*, **121**, (2017) 3213-3219
- [11] N. Yu, B. Dong, W.W. Yu, B. Hu, Y. Zhang And Y. Cong, *Applied Surface Science*, **258**, (2012) 5729 - 5732
- [12] M. Przybyszewska and M. Zaborski, *Polymer Letters*, **3**, (2009) 542-552
- [13] J. Mayekar, V. Dhar and S. Radha, *International Journal of Research in Engineering and Technology*, **3**, (2014) 03
- [14] L. Wang and M. Muhammed, *Journal of Material Chemistry*, **9**, (1999) 2871–2878
- [15] S.P. Garcia, and S. Semancik, *Chemistry of Materials*, **19**, (2007) 4016-4022
- [16] S.S Kumar, P. Venkateswarlu, V.R. Rao and G.N Rao, *International Nano Letters*,**3**, (2013) 30-37
- [17] D.I. Rusu, G.G. Rusu, and D. Luca, *Acta Physica Polonica A*, **119**, (2011) 850–856
- [18] R. He, and T. Tsuzuki, *Journal of American Ceramic Society*, **93**, (2010) 2281-2285

- [19] O. Sheikhnejad-Bishe, International Journal of Electrochemical Science, **9**, (2014) 3068-3077
- [20] N. Shukla, and A.G Roy, Materials Letters, **60**, (2006) 995-998
- [21] R. A. Laudise, and A. A. Ballman, Journal of Physical Chemistry, **64**, (1960) 688–691
- [22] K. M. Lee, C.W. Lai, K.S. Ngai, and J.C. Juan, Water Research, **88**, (2016) 428 - 448
- [23] M. Søndergaard, E. D. Bøjesen, M. Christensen, and B.B. Iversen, Crystal Growth and Design, **11**, (2011) 4027–4033
- [24] M. Pudukudy, and Z. Yaakob, Solid State Science, **30**, (2014) 78–88
- [25] O. Singh, N. Kohli, and R.C. Singh, Sensors and Actuators B: Chemical, **178**, (2013) 149-154
- [26] C.K. Srikanth, and P. Jeevanandam, Journal of Alloys and Compounds, **486**, (2009) 677–684
- [27] C.W. Tang, Modern Research in Catalysis, **2**, (2013) 19-24
- [28] A. M. Pourrahimi, D. Liu, L. K. H. Pallon, R. L. Andersson, A. M. Abad, J. M. Lagarón, M. S. Hedenqvist, V. Ström, U. W. Gedde, and R. T. Olsson, RSC Advances, **4**, (2014) ISSUE NO 35568
- [29] M.K. Lima, D.M. Fernandes, M.F. Silva, M.L. Baesso, A.M. Neto, G.R. de Morais, C.V. Nakamura, A.O. Caleara, A.A.W. Hechenleiter, and E.A.G. Pineda, Journal of Sol-Gel Technology, **72**, (2014) 301-309
- [30] M. Hoffman, S. Martin, W. Choi, and D. Bahnemann, Chemical Review, **95**, (1995) 69-96
- [31] J.M. Moore, R. Louder, and C.V. Thompson, Coatings, **4**, (2014) 651-669
- [32] U. Manzoor, M. Islam, L. Tabassam, and S.U. Rahman, Physica E, **41**, (2009) 1669-1672
- [33] I.K. Konstantinou, and T.A. Albanis, Applied Catalysis B: Environmental, **49** (1), (2004) 1-14

-
- [34] A. Ajmal, I. Majeed, R.N. Malik, H. Idriss, and M.A. Nadeem, RSC Advances, **4**, (2014) 37003
- [35] A. McLaren, T. Valdes-Solis, G. Li, S.C. Tsang, Journal of the American Chemical Society, **35**, (2009) 12540-12541
- [36] C.S. Turchi, and D.F. Ollis, Journal of Catalysis, **122**, (1990) ISSUE NO 178
- [37] N. Barka, and Y. Ait-Ichou, Arabian Journal of Chemistry, **3**, (2010) 279-283
- [38] M.V. Shankar, B. Nappolian, S. Sakthivel, B. Arabindo, M, Palanichamy, and V. Murugesan, Indian Journal of Engineering and Materials Sciences, **8**, (2001) 104-109

Chapter 7: Conclusions and Recommendations

7.1 Conclusions

In this dissertation, the synthesis of various morphologies and sizes of ZnO nanoparticles using a simple microwave assisted heating method is reported. Furthermore, the activity of the ZnO nanoparticles was studied in the photocatalytic degradation of Rhodamine B. Various reaction parameters such as pH of precursor solution, type of precursor, and reaction time were varied in order to produce various morphologies and sizes of ZnO. Varying the pH (i.e. 7, 10, and 14) of the precursor solution resulted in three different morphologies that took on pseudo-spherical, bullet-, and rod-like shapes. The BET measurements found that the surface areas for the pseudo-spherical, bullet-, and rod-like ZnO nanoparticles were 14.73, 10.05 and 8.43 $\text{m}^2.\text{g}^{-1}$, respectively. In the studies of the photocatalytic degradation of Rhodamine B, the morphology with the highest surface area and the highest proportion of exposed polar facets, which is dependent on the type of morphology, was obtained when synthesis was done at pH 7. In this study, the pseudo-spherical nanoparticles were found to be the most efficient in degrading Rhodamine B.

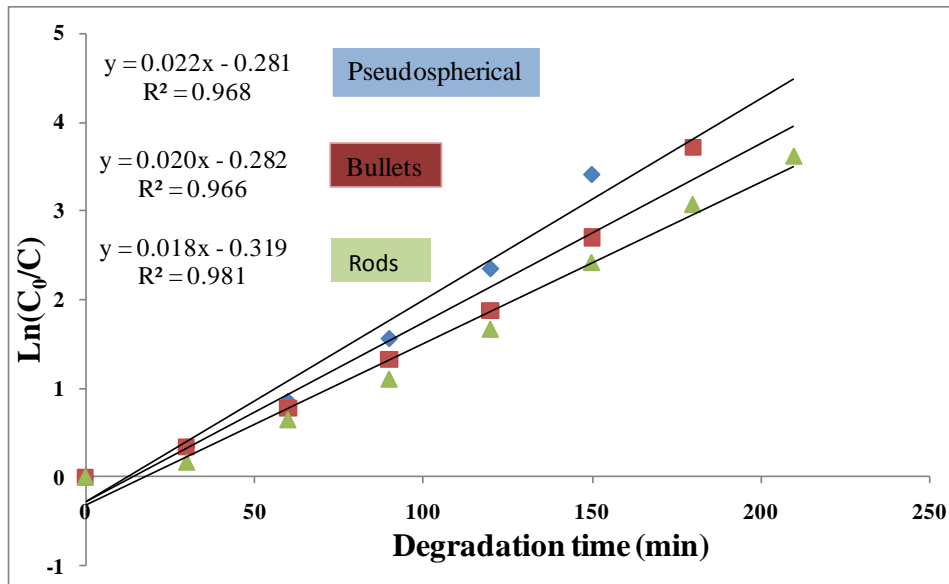
The synthesis of ZnO nanoparticles while varying the reaction time produced different sized nanoparticles, with the long reaction time producing larger nanoparticles than those synthesized at shorter reaction time. The nanoparticles synthesized at long reaction times (i.e. 30, 18 and 15 min) had a hexagonal morphology, as the reaction time was reduced to 11 and 8 min, the nanoparticles took on a more rod-like morphology. PL results indicated a slight blue shift of the nanoparticles synthesized at 8 min relative to those synthesized at much longer reaction times (i.e. 30, 18, 15, and 11 min). In the studies of the photocatalytic degradation of Rhodamine B, a trend was observed whereby the smaller sized nanoparticles showed the highest activity in the degradation of Rhodamine B than those that were larger. This difference in photocatalytic activity was attributed to the fact that smaller sized nanoparticles had a high surface area and hence more active sites were exposed on the surface for the Rhodamine B molecules to bind and be degraded.

The synthesis of ZnO nanoparticles using different zinc metal salts was performed in order to get a better understanding of the effect of counter anions on the structural, optical and photocatalytic activity of the ZnO nanoparticles. The PL results indicated a slight shift to higher energy (i.e. lower wavelength) as the precursors were changed with the order of $S_{NO_3^-} > S_{CH_3COO^-} > S_{Cl^-} > S_{SO_4^{2-}}$. The difference in the emission energy of the nanoparticles was attributed to size differences. The surface area measured by BET was found to be 13.25, 12.54, 12.02, and 1.24 m² .g⁻¹ for the $S_{NO_3^-} > S_{CH_3COO^-} > S_{Cl^-} > S_{SO_4^{2-}}$ nanoparticles, respectively. The photocatalytic activity of the different nanoparticles was significantly different with the $S_{NO_3^-}$, $S_{CH_3COO^-}$, S_{Cl^-} , and $S_{SO_4^{2-}}$ degrading Rhodamine B dye in 120, 150, 180, and 240 min. The difference in the degradation rate was explained using surface area. The nanoparticles with the highest surface area were more efficient in degrading the dye molecules due to the vast amount of active sites present on their surface.

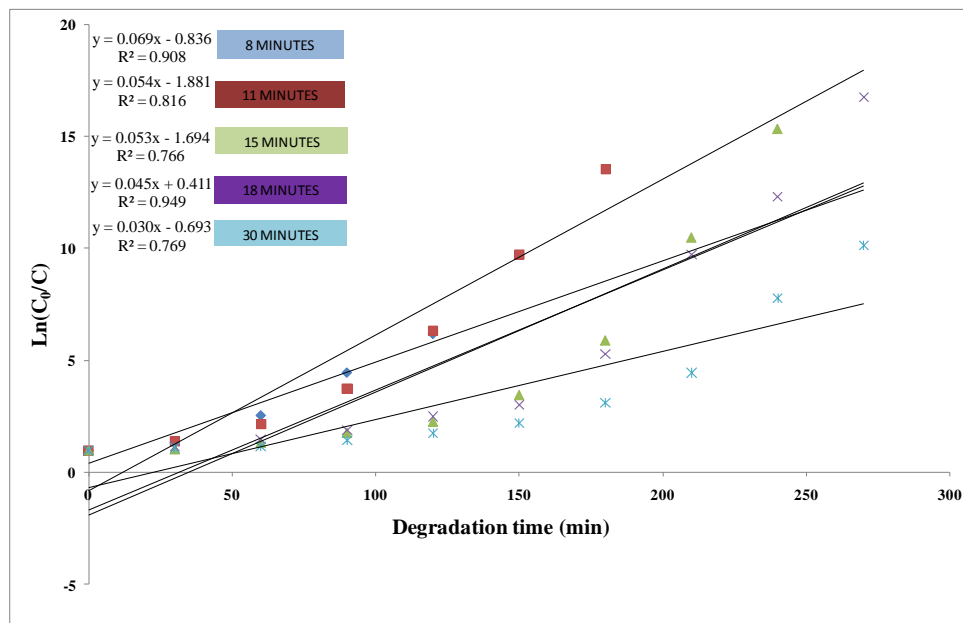
7.2 Recommendations

The photocatalytic activity of ZnO nanoparticles is highly dependent on the size and morphology of the nanocrystal being used. Therefore, suggestions for future work include using different capping agents in the synthesis of ZnO as a means of producing monodispersed nanoparticles. The ability to produce nanoparticles with a narrow size distribution and one type of morphology would allow for a better understanding of the effect of morphology on the photocatalytic activity of ZnO. To get a better understanding of the practical application of ZnO as a photocatalyst in real environmental conditions, photocatalysis can be done using direct sunlight. The possibility of using ZnO in the degradation of other dyes can be investigated. To fully confirm that Rhodamine B was entirely converted into carbon dioxide and water, mass spectroscopic analysis of the colourless solution obtained can be performed in order to support the complete degradation claim reported in literature.

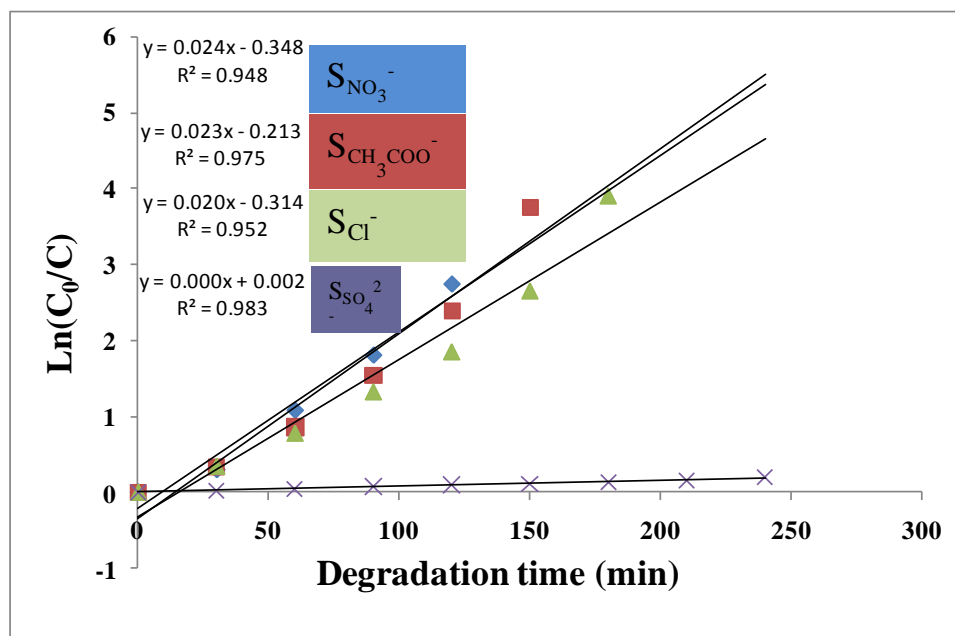
Annexure



ANNEXURE A: Graphical representation of the determination of the rate constants for degradation of Rhodamine B using different ZnO morphologies.



ANNEXURE B: Graphical representation of the determination of the rate constants for degradation of Rhodamine B using ZnO nanoparticles synthesized at different reaction times.



ANNEXURE C: Graphical representation of the determination of the rate constants for degradation of Rhodamine B using ZnO synthesized from different zinc metal salts.